

# INVESTIGATION OF ARCHITECTURES AVAILABLE FOR WIRELESS CHARGING

by

Jamel Andre` Long

A thesis submitted to the faculty of  
The University of North Carolina at Charlotte  
in partial fulfillment of the requirements  
for the degree of Master of Science in  
Electrical Engineering

Charlotte

2018

Approved by:

---

Dr. Madhav Manjrekar

---

Dr. Farid Tranjan

---

Dr. Robert Cox

©2018  
Jamel Andre` Long  
ALL RIGHTS RESERVED

## ABSTRACT

JAMEL ANDRE` LONG. Investigation of Architectures Available for Wireless Charging.  
(Under the direction of DR. MADHAV MANJREKAR)

There are many items in our day to day lives that where once plugged in to a wall outlet or even a USB port for power and/or communications that are now completely wireless. The computer mouse has already lost its tail, our telephones and headphones have become wireless – even electric toothbrushes and cellphones don’t need cables any longer. Data which was once only conveyed over physical lines is now conveyed wirelessly. Automobiles have traditionally been powered by some form of fossil fuel which pollutes the environment and may have large price fluctuations. With the recent high prices of fossil fuels and government mandates on air pollution alternate forms of clean energy have been pushed to the forefront of today’s research. Advances in battery research involving higher capacity and lower cost have sparked a renewed interest in Electric vehicles have become very popular in recent years. There are various types of electric vehicles in the market today including, various types of hybrids as well as and fully electric vehicles. To date for the most part they are still tethered to a wall charger which limits there locations due to weather and requiring human intervention to facilitate charging and disconnecting their onboard batteries. Some advantages of wireless charging over a tethered can be summarized as follows. Convenience – One complaint from PHEV owners is that they find connecting the charging plug that is substantially larger and heavier than the typical NEMA-5 plug troublesome. Inductive power transfer systems can be completely autonomous. Vehicles

can begin charging right away when they are parked over a charger. Weather – IPT systems can be embedded underground, eliminating issues related to exposure to inclement weather such as rain, snow, or freezing conditions. Wear- The mechanical handling of the tethered cable and plug will wear over a relative short period of time. The IPT system being embedded has no mechanical connection to be made, thereby removing a major component for wear. Anti-vandalism – Public plug-in systems are prone to vandalism such as theft of the copper cable. Because potential vandals and thieves cannot easily see IPT system infrastructure, it seems far less likely they will dig under the road to target it. Low risk of hazards – the wire used in a plug-in system may be a potential trip hazard for people; given that in a public setting the charging environment is usually close to the road, the level of danger imposed by another vehicle hitting someone is not negligible. Today we are researching viability of developing a wireless charger for electric vehicles by using some form of wireless power transfer.

## ACKNOWLEDGEMENTS

I would like to take this opportunity to thank my advisor Dr. Madhav Manjrekar for his invaluable guidance and advice throughout this thesis and defense process. I want to thank my committee members, Dr. Farid Tranjan and Dr. Robert Cox for their generous advice and interest.

I would also like to thank the academic and administrative staff at the Department of Electrical and Computer Engineering in The William States Lee College of Engineering at UNC Charlotte. In addition I would like to thank the researchers and professors at the Energy Production Infrastructure Center (EPIC).

Finally I would like to thank my wife and family who have been patient and supported me throughout my graduate experience and my thesis defense at UNCC.

## TABLE OF CONTENTS

LIST OF TABLES	viii
LIST OF FIGURES	ix
LIST OF ABBREVIATIONS	xiii
Chapter 1. WIRELESS POWER TRANSFER	1
1.1 INTRODUCTION	1
1.2 HISTORY	1
1.3 NIKOLA TESLA AND THE TESLA COIL	5
1.4 TYPES OF WIRELESS POWER TRANSFER	8
1.5 FAR FIELD WIRELESS POWER TRANSFER	8
1.6 NEAR FIELD POWER TRANSFER	13
1.7 SUMMARY	15
Chapter 2. NEAR FIELD POWER TRANSFER	19
2.1 INTRODUCTION	19
2.2 POWER DENSITY	19
2.3 IPT GAP ENERGY DENSITY	23
2.4 CAPACITIVE POWER TRANSFER GAP ENERGY DENSITY	26
2.5 WPT COUPLER VOLUME CALCULATIONS	29
2.6 ANALYTICAL COMPARISON OF INDUCTIVE AND CAPACITIVE POWER TRANSFER	36
Chapter 3. TRADITIONAL VS WIRELESS POWER TRANSFER	40
3.1 INTRODUCTION	40
3.2 RESONANT POWER CONVERTERS	42
3.2.1 TRADITIONAL SERIES RESONANT CONVERTER	47
3.2.2 TRADITIONAL PARALLEL RESONANT CONVERTER	51
3.2.3 TRADITIONAL SERIES PARALLEL RESONANT CONVERTER	54
3.2.4 LLC RESONANT CONVERTER	57
3.2.5 SUMMARY	73
Chapter 4. WIRELESS POWER TRANSFER SERIES-SERIES/PARALLEL RESONANT CONVERTER	76
4.1 INTRODUCTION	76

4.2	WIRELESS POWER TRANSFER	76
4.2.1	WPT PARALLEL-SERIES RESONANT CONVERTER	78
4.2.2	WPT PARALLEL TO PARALLEL RESONANT CONVERTER	81
4.2.3	DESIGN TRADE-OFFS	82
4.2.4	SERIES-SERIES AND SERIES-PARALLEL RESONANT POWER CONVERTER CONSIDERATION FOR HIGH POWER WPT DESIGN	87
Chapter 5.	DESIGN, MODELING AND SIMULATION FOR 7.5KW WIRELESS CHARGER	91
5.1	INTRODUCTION: PRACTICAL IMPLEMENTATION OF WIRELESS DESIGN	91
5.2	INITIAL DESIGN PARAMETERS	91
5.3	PHASE 1: MATCHING PRIMARY AND SECONDARY LC	99
5.4	PHASE 2: INCREASING THE RESONANT CAPACITOR VALUE TO 0.036 $\mu$ F	108
5.5	PHASE 3: INCREASING THE RESONANT CAPACITOR VALUE TO 0.037 $\mu$ F	111
5.6	PHASE 4: INCREASING THE RESONANT CAPACITOR VALUE TO 0.038 $\mu$ F	114
5.7	PHASE 5: ADDING SERIES INDUCTOR OUTPUT	116
5.8	PHASE 6: INCREASING PRIMARY LEAKAGE INDUCTANCE	118
5.9	SIMPLIFIED SCHEMATICS OF CIRCUIT USED FOR SIMULATION	121
5.10	SCHEMATIC DIAGRAMS	125
5.11	TRANSFORMER DESIGN	129
5.11.1	TRANSFORMER CORE SELECTION	129
5.11.2	DETERMINE WIRE GAUGE	134
Chapter 6.	RESULTS AND CONCLUSION	136
6.1	RESULTS	136
6.2	CONCLUSION	139
	REFERENCES	141

## LIST OF TABLES

Table 1-1 Summary WPT technologiesSummary WPT technologies.....	18
Table 2-1 Table of WPT Coupler Geometry relationships .....	31
Table 3-1 Summary of resonant topologies to be investigated.....	41
Table 3-2 Summary of three LLC resonant converter designs .....	75
Table 4-1 Summary of Series-Series Converter .....	77
Table 4-2 Summary of Series-Parallel Converter .....	78
Table 4-3 Summary of Parallel to Series Converter .....	81
Table 4-4 Summary of Parallel to Parallel Conversion .....	82
Table 4-5 Summary of topologies.....	85
Table 4-6     Secondary Impedance and Load Voltage/Current .....	86
Table 4-7     Properties at the secondary Resonant Frequency $\omega_0$ .....	86
Table 5-1 Summary of Calculated vs Simulated values .....	118



## LIST OF FIGURES

Figure 1 Illustration of the timeline for the development of Wireless Power Transfer .....	2
Figure 2 Illustration of the timeline for the development of Wireless Power Transfer Continued.....	3
Figure 3 Simplified Schematic of Unipolar Tesla coil circuit. [7] .....	6
Figure 4 Image of the Tesla Tower, Shoreham, Long Island, NY, 1904. [11] .....	9
Figure 5 Ferdinand Braun's phased array from 1905 [17] .....	10
Figure 6 Simplified Schematic Diagram of Rectenna Circuit [12].....	11
Figure 7 Picture Of First Ground-To-Ground MPT Experiment In 1975 At The Venus Site Of The JPL Goldstone Facility [12].....	12
Figure 8 Picture Of Tesla Demonstrating Wireless Power Transmission Using Capacitive Coupling At Columbia, New York, In 1891 [8] .....	14
Figure 9 Diagram Shows The Electromagnetic Frequency Spectrum [17] .....	16
Figure 10 Diagram Showing Classification Of Wireless Energy Transfer Technologies ..	17
Figure 11 Gap volume and coupler volume. (a1) Inductive Power Transfer coupler. (a2) Capacitive Power Transfer coupler. [1] .....	20
Figure 12 Inductive Power Transfer two pot cores [1] .....	21
Figure 13 Capacitive Power Transfer one set of parallel plates [1].....	21
Figure 14 3D Cut view of Inductive Power Transfer Two pot cores [1] .....	22
Figure 15 3D Model View of Parallel plates[1].....	22
Figure 16 Simplified Schematic of Typical Inductive Power Transfer topology .....	23
Figure 17 Simplified Schematic of Typical topology for Capacitive Power Transfer [19]	26
Figure 18 Graph illustrating the relationship between Voltage and Current .....	28
Figure 19 Graph of Gap Power Density [1].....	29
Figure 20 Coupler volume optimization. (a) Optimization of $r_w$ (with $r_A$ $r_g$ fixed) [1]....	33
Figure 21 Coupler volume with different gap ratio $r_g$ [1]. .....	33
Figure 22 Coupler/gap volume ratio versus gap/area ratio: [1] .....	35
Figure 23 Inductive Power Density and Transfer analysis chart [1]. .....	35
Figure 24 Capacitive Power Density and Transfer analysis chart [1]. .....	36
Figure 25 Coupler power density and gap power density [1].....	38
Figure 26 Air gap power versus gap distance [1]. .....	38
Figure 27 Coupler power density versus air gap distance [1].....	39
Figure 28 Simplified Schematic Diagram of Full bridge converter .....	43
Figure 29 Typical step response of un dampened primary waveform.....	43
Figure 30 Typical step response of critically dampened primary waveform.....	44
Figure 31 Graph of typical Waveforms for Full bridge converter.....	44
Figure 32 Half Bridge Bipolar converter .....	45
Figure 33 Graph of typical Half Bridge Bipolar Converter Waveforms .....	45
Figure 34 Functional schematic diagram of resonant transformer with coupling factor ....	46
Figure 35 Simplified Schematic of Half Bridge Series Resonant Converter.....	48

Figure 36 Reference diagram of DC operating region of Series Resonant Converter [26].	49
Figure 37 Reference diagram of typical waveforms of Series Resonant Converter [26].	49
Figure 38 Simplified Schematic of Half Bridge parallel resonant converter.	51
Figure 39 Reference diagram of operating region of Parallel Resonant Converter [26]	52
Figure 40 Reference diagram of graph indicating DC Simulation waveforms of Parallel Resonant Converter [26]	53
Figure 41 Simplified Schematic of Half bridge series parallel resonant converter	55
Figure 42 Reference diagram of operating region of Series Parallel Resonant Converter [26].	56
Figure 43 Reference of Simulated waveforms of Series Parallel Resonant Converter [26, 27]	56
Figure 44 Simplified Schematic of LCC and LLC resonant tank circuits	59
Figure 45 Reference diagram of DC characteristic of LLC resonant converter [26, 27]	59
Figure 46 Simplified Schematic of Half bridge LLC resonant converter	60
Figure 47 DC characteristic of LLC resonant converter [26]	62
Figure 48 Reference diagram of three operating regions of resonant converter [26]	63
Figure 49 Simulated Operational Waveforms in region 1	64
Figure 50 Reference diagram of Simulation waveforms in region 2 [26]	65
Figure 51 Simplified Schematic LLC resonant converter Circuit diagram during mode 1 in region 2	65
Figure 52 Circuit diagram during mode 2 in region 2	66
Figure 53 Circuit diagram during mode 3 in region 2	67
Figure 54 Simulation waveforms of Phase 1 with 400V	69
Figure 55 Simulation waveforms of Phase 1 with 300V	70
Figure 56 Simulation waveforms of Phase 2 with 400V	71
Figure 57 Simulation waveforms of Phase 2 with 300V	71
Figure 58 Simulation waveforms of Phase 3 with 400V	72
Figure 59 Simulation waveforms of Phase 3 with 300V	73
Figure 60 Primary loss for three designs with $V_{in} = 400V$	73
Figure 61 Primary loss for three designs with $V_{in} = 360V$	74
Figure 62 Primary loss for three designs with $V_{in} = 300V$	74
Figure 63 Simplified Schematic diagram of resonant mode converter components	76
Figure 64 Simplified Schematic diagram of resonant mode Series-Series WPT	77
Figure 65 Simplified Schematic diagram of resonant mode Series-Parallel WPT	78
Figure 66 Simplified schematic of Parallel-Series Resonant Converter	78
Figure 67 Simplified schematic of Parallel-Parallel Resonant Converter	82
Figure 68 Simplified diagram of Wireless Power Transfer system [25]	83
Figure 69 Simplified schematic of Series-Series Resonant Converter	87
Figure 70 Simplified Full Bridge LLC - (SP) Design Schematic	91
Figure 71 Simplified Block Diagram of a Full bridge	92
Figure 72 Switch Bank	93
Figure 73 Rectifier/Filter section	94

Figure 74 Output characteristics [23] .....	95
Figure 75 Resonant Tank Network .....	96
Figure 76 Transmit and Receive coils separated by a distance h .....	99
Figure 77 Simplified Schematic of Dual Resonant Network.....	100
Figure 78 Simplified Schematic of Combined Dual Resonant Network .....	101
Figure 79 Graph of $V_c$ and $I_l$ with 370 $\mu$ H choke and .034 $\mu$ F cap .....	104
Figure 80 Output and current waveforms with 380 $\mu$ F choke and 0.034 $\mu$ F capacitor .....	105
Figure 81 Primary waveforms with 370 $\mu$ H choke and 0.034 $\mu$ F capacitor.....	106
Figure 82 Primary Inductor Voltage, FET Voltage and Current Waveforms with 370 $\mu$ F choke and 0.034 $\mu$ F capacitor .....	106
Figure 83 Coupling coefficient “k”- factor as a function of reactive component values and 0.034 $\mu$ F .....	108
Figure 84 Output and current waveforms with 380 $\mu$ F choke and 0.036 $\mu$ F capacitor .....	109
Figure 85 Primary waveforms with 370 $\mu$ H choke and 0.036 $\mu$ F capacitor.....	109
Figure 86 Primary inductor voltage, FET Drain voltage and FET current 370 $\mu$ H choke and 0.036 $\mu$ F capacitor .....	110
Figure 87 Coupling coefficient “k”- factor as a function of $C_r = 0.036\mu$ F.....	111
Figure 88 Output and current waveforms with 380 $\mu$ F choke and 0.037 $\mu$ F capacitor .....	112
Figure 89 Primary waveforms with 370 $\mu$ H choke and 0.037 $\mu$ F capacitor.....	112
Figure 90 Primary inductor voltage, FET Drain voltage and FET current 370 $\mu$ H choke and 0.037 $\mu$ F capacitor .....	113
Figure 91 Coupling coefficient “k”- factor as a function of $C_r = 0.037\mu$ F.....	113
Figure 92 Graph of $V_c$ and $I_l$ Waveforms with 380 $\mu$ Hchoke and 0.038 $\mu$ F Capacitor .....	114
Figure 93 Primary waveforms with 370 $\mu$ H choke and 0.038 $\mu$ F capacitor.....	114
Figure 94 Output and current waveforms with 380 $\mu$ H choke and 0.038 $\mu$ F capacitor .....	115
Figure 95 Primary inductor voltage, FET Drain voltage and FET current 370 $\mu$ H choke and 0.038 $\mu$ F capacitor .....	115
Figure 96 Primary waveforms with 370 $\mu$ H choke and 0.038 $\mu$ F capacitor and 16 $\mu$ H choke on output .....	116
Figure 97 Output and current waveforms with 380 $\mu$ F choke and 0.035 $\mu$ F capacitor and 16 $\mu$ H Choke in series with output .....	117
Figure 98 Primary inductor voltage, FET Drain voltage and FET current 370 $\mu$ H choke and 0.036 $\mu$ F capacitor and 16 $\mu$ H choke.....	117
Figure 99 Phase 6 Primary waveforms .....	119
Figure 100 Primary waveforms .....	120
Figure 101 Schematic used to for simulation to produce waveforms.....	121
Figure 102 Design 2 Schematic with Non-ideal components.....	122
Figure 103 Primary waveforms with real world component values .....	123
Figure 104 Primary FET waveforms with real world component values .....	124
Figure 105 Schematic of full bridge Control Section .....	125
Figure 106 Schematic Of Primary Full Bridge Inverter Section .....	126
Figure 107 Schematic Of Bias And House Keeping Supply .....	127
Figure 108 Schematic Of Synchronous Rectification.....	128

Figure 109 Cool Mu “E-Core” Selector Chart.....	131
Figure 110 Mechanical Parameters of Bar Core .....	131
Figure 111 Field Intensity .....	133
Figure 112 Components of Wireless Transformer.....	135
Figure 113 Vin 200V, Vo 44.7V Switching 83Khz.....	136
Figure 114 Vin 200V, Vo 19V Switching 47Khz.....	137
Figure 115 VIN 150V, VO 16V SWITCHING 47KHZ.....	137
Figure 116 Vin 150v, Vo 50v switching 47khz.....	138
Figure 117 Vin 100V, with 1.5 inch Separation from Primary to Secondary .....	139

## LIST OF ABBREVIATIONS

WPT	Wireless Power Transfer
IPT	Inductive Power Transfer
CPT	Capacitive Power Transfer
SRC	Series Resonant Converter
PRC	Parallel Resonant Converter
SPRC	Series Parallel Resonant Converter
CET	Contactless Energy Transfer
SS	Series-Series
SP	Series-Parallel
PS	Parallel-Series
L	Inductance [H]
C	Capacitance [F]
I	Current [A]
$P_{out}$	Output power [W].
$U_C$	Coupling capacitor voltage [V]
$I_C$	Coupling capacitor current [A].
$I_L$	Coupling inductor current [A]
$U_L$	Coupling inductor voltage [V].
$\epsilon_0$	Vacuum permittivity and [F/m].
$\epsilon_r$	Relative permittivity [F/m]
$\mu_0$	Vacuum Permeability [H/m]
$\mu_r$	Relative Permeability [H/m]

$A_c$	Cross sectional area [ $m^2$ ]
$d$	Distance [m]
$H$	Magnetic Field Strength amperes/meter or A/m
$B$	Magnetic flux density in the core [T] Tesla
$H$	$B_0/\mu_0$
$Q_{gap}$	Gap reactive power [ $V \cdot A$ ]
$\rho$	power density
$V_{gap}$	Gap volume [ $m^3$ ].
$V_{coupler}$	Coupler volume [ $m^3$ ].
$r_g$	Gap ratio ( $d/\sqrt{A_c}$ ).
$r_A$	Core area Dimension
$r_w$	Core window dimension
$r_c$	Capacitor coupler dimension ratio
$k_c$	Coupler volume coefficient.
$k_w$	Winding area fill factor.
$k$	Coupling Coefficient between the primary and secondary coils
$E_c$	Coupling capacitor electric field
$D_c$	Coupling capacitor electric field in gap density
$H_L$	Coupling inductor magnetic Intensity
$B_L$	Coupling inductor magnetic field
$\rho_c$	Coupling capacitor gap power density [ $W/m^3$ ].
$\rho_L$	Coupling inductor gap power density [ $W/m^3$ ].
$E_{max}$	Maximum electric field strength in the air gap [V/m]

$J_{\max}$	Maximum current density in conductor [A/m <sup>2</sup> ]
$f_{\text{sw}}$	Switching frequency [kHz]
$f_0$	Resonant frequency [kHz]
$\omega_0$	Resonant angular velocity [rad/s]
RLC	Resistor Inductor Capacitor
LC	Inductor Capacitor

## Chapter 1. WIRELESS POWER TRANSFER

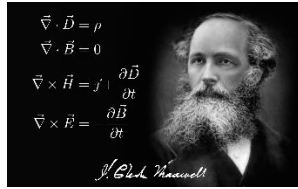
### 1.1 INTRODUCTION

In this section we will examine where the concept of Wireless Power Transfer came from. We will look at the history of and some key figures and how their contributions have lead us to the wireless power transfer. We will look at the contributions of Nikola Tesla and the tesla coil. We will examine the different types of wireless power transfer. We will examine far field power transfer as its various transmission types. We will examine near filed power transfer and how it differs from far field power transfer. Finally we will summarize the different types of wireless power transfer and their applications and the frequency ranges where they would be used.

### 1.2 HISTORY

What is WPT, or Wireless Power Transfer? As the name implies wireless power transfer or wireless energy transfer is the transmission of electrical energy from a power source to an electrical load, without the use of physical/mechanical connection between the sending source and the receiving load [2]. There is little difference between the history of WPT and that of wireless communications. In fact, the history of WPT is largely based on the history of wireless communications [2].

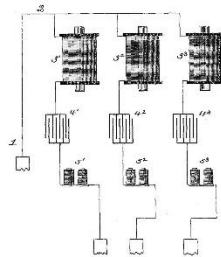




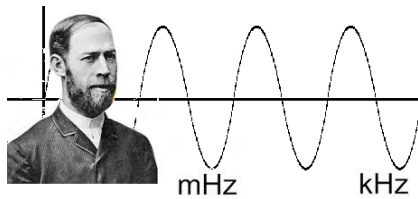
In 1873, James Clerk Maxwell, Derived Maxwell's Equations [3]



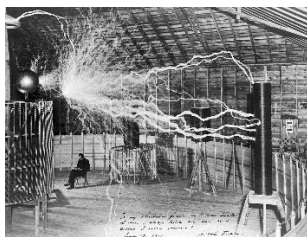
Guglielmo Marconi and His 1<sup>st</sup> Transmitter in the 1890's [4]



Maurice Hutin and Maurice Le-Blanc and the Multiple Telegraph Circuit 1891 [5]

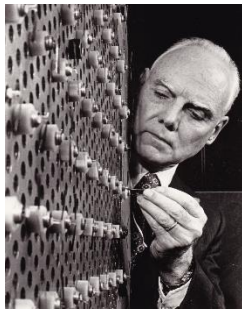


1898, Heinrich Hertz Confirms the existence of Electromagnetic Radiation [6]

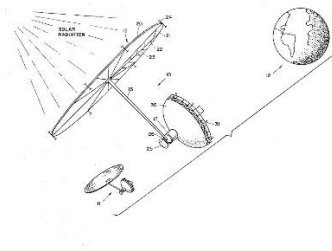


Nikola Tesla and Wardencllyffe Tower 1904 [7]

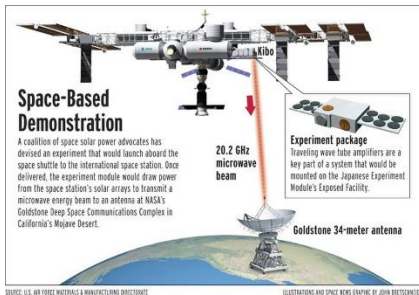
FIGURE 1 ILLUSTRATION OF THE TIMELINE FOR THE DEVELOPMENT OF WIRELESS POWER TRANSFER



William Cyrus Brown Pioneered Microwave Power Transmission in 1960's [8]



Peter Glaser Father of Solar-Power Satellite Idea 1971 [9]



Goldstone Deep Space Communications Performs experiments in the tens of kilowatts 1975 [10]



Fulton Innovation Charges Tesla Car wirelessly with 89% efficiency 2011 [11]

FIGURE 2 ILLUSTRATION OF THE TIMELINE FOR THE DEVELOPMENT OF WIRELESS POWER TRANSFER CONTINUED

In Wireless Power Transfer, WPT, a wireless transmitter connected to a power source conveys the field energy across an intervening space to one or more receivers, where it is converted back to an electrical current and then used. How did this all start? The lineage for WPT can be traced back to 1826 with André-Marie Ampère's who gave a formalized understanding of the relationships between electricity and magnetism using algebra showing that electric current produces a magnetic field [2]. His main contribution was in the field of Electricity and magnetism [12]. The unit for current 'Ampere' is named after him [12]. His research was then followed in 1831 by Michael Faraday. Faraday postulated that an electrical current moving through a wire creates "fields of force" surrounding the wire [13]. Faraday developed Faraday's law of induction in 1831 describing the electromagnetic force induced in a conductor by a time-varying magnetic flux [13]. Faraday made the first transformer [13]. The unit of capacitance is named after him. One of the most significant contributors was James Clerk Maxwell who wrote a mathematical treatise formalizing the theory of fields in 1856: *On Faraday's Lines of Force* [14]. In 1862 he synthesized these and other observations, experiments and equations of electricity, magnetism and optics into a consistent theory, deriving Maxwell's equations. This set of partial differential equations forms the basis for modern electromagnetics, including the wireless transmission of electrical energy [14]. In 1864 Maxwell predicted the existence of electromagnetic waves by means of a mathematical model [3]. In 1873 he published his results in "A Treatise on Electricity and Magnetism" and are known as "Maxwell's Equations" [14]. In 1884 John Henry Poynting developed equations for the Poynting vector, which describes the direction and magnitude of electromagnetic energy flow and is used in the Poynting theorem, a statement about energy conservation for electric

and magnetic fields. Poynting's theorem and the Poynting vector, are used in the analysis of wireless energy transfer systems [14]. In 1888 Heinrich Hertz first succeeded in showing experimental evidence of radio waves using his spark-gap radio transmitter [2]. The prediction and evidence of radio waves toward the end of the 19th Century was the beginning of wireless power transfer (WPT) [2]. During the same period, when Marchese G. Marconi and Reginald Fessenden pioneered communication via radio waves, Nikola Tesla investigated wireless transmission of electrical energy using his radio frequency resonant transformer circuit called the Tesla Coil [2].

### 1.3 NIKOLA TESLA AND THE TESLA COIL

Tesla performed the first WPT experiments in 1899 [2]. Using his Tesla coil as a radio frequency oscillator that drives an air-core double-tuned resonant transformer to produce high voltages at low currents [7]. The specialized transformer used in the Tesla coil circuit is what would be called a resonant transformer. While a traditional, non-wireless, high power transformer is designed to transfer energy efficiently from primary to secondary winding through a core by means of magnetic coupling without storing energy within the transformer itself [7]. The resonant transformer of the Tesla coil transformer is designed to temporarily store electrical energy. Each winding has a capacitance across it and functions as an LC circuit (resonant circuit, tuned circuit), storing oscillating electrical energy, analogously to a tuning fork [7].

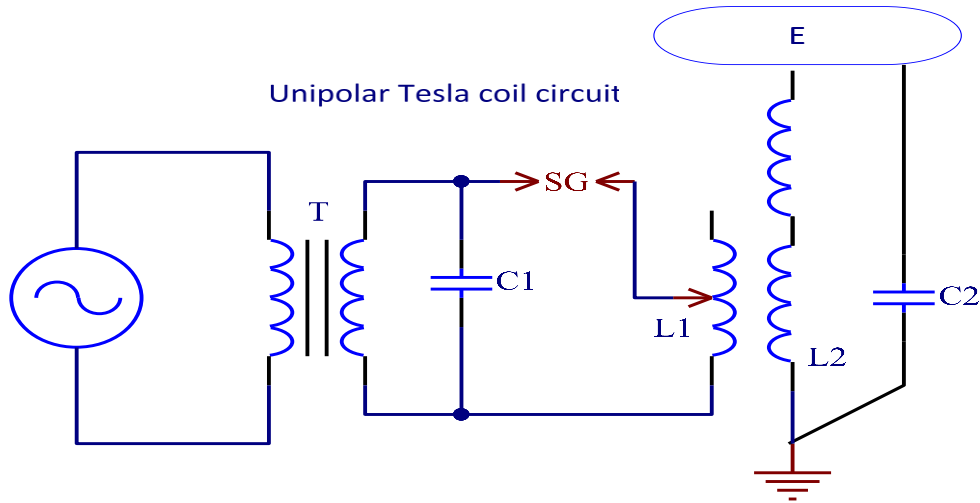


FIGURE 3 SIMPLIFIED SCHEMATIC OF UNIPOLAR TESLA COIL CIRCUIT. [7]

The unipolar tesla coil of figure 1.3, C2 is not an actual capacitor but represents the capacitance of the secondary windings L2, plus the capacitance to ground of the toroid electrode E [7]. The primary winding ( $L1$ ) consisting of a relatively few turns of heavy copper wire or tubing, is connected to a capacitor ( $C1$ ) through the spark gap ( $SG$ ). The secondary winding ( $L2$ ) consists of many turns (hundreds to thousands) of fine wire on a hollow cylindrical form inside the primary. The secondary is not connected to an actual capacitor, but it also functions as an LC circuit, the inductance ( $L2$ ) resonates with ( $C2$ ), the sum of the stray parasitic capacitance between the windings of the coil, and the capacitance of the toroidal metal electrode attached to the high voltage terminal. To produce the largest output voltage the primary and secondary circuits are tuned so they resonate at the same frequency. This allows them to exchange energy, so the oscillating current alternates back and forth between the primary and secondary coils.”

Resonant Frequency of Primary[7]

$$f_1 := \frac{1}{2\pi} \cdot \sqrt{\frac{1}{L_1 \cdot C_1}} \quad (1-1)$$

Resonant Frequency of Secondary[7]

$$f_2 := \frac{1}{2\pi} \cdot \sqrt{\frac{1}{L_2 \cdot C_2}} \quad (1-2)$$

A transformer is tuned to resonance when the primary Frequency  $f_1$  equal to the secondary frequency  $f_2$

PRIMARY: SECONDARY RESONANCE RATIO[7]

$$f_1 := f_2 \quad (1-3)$$

Therefore the primary and secondary LC circuits must be equal

PRIMARY AND SECONDARY LC RATIO[7]

$$\mathbf{L_1 C_1 := L_2 C_2} \quad (1-4)$$

## 1.4 TYPES OF WIRELESS POWER TRANSFER

WPT falls into two categories near field and far field power transfer. Where one defines the “near-field” is somewhat subjective, but is generally accepted to be below one wavelength from the transmitting antenna.[15] Since the wavelength of the transmitting antenna is relatively short even at lower frequencies this mode of power transfer is referred to as near field power transfer. This is because the reactive near-field occurs at and below a fraction ( $1/2\pi$ ) of a wavelength and is a non- radiative storage field – this is the region of most interest for inductive wireless power transfer.[15] When transmitting over large distances the wavelength could easily be much less than the distance between transmit and receive antenna, thus this type of power transfer is considered Far Field Power Transfer.

## 1.5 FAR FIELD WIRELESS POWER TRANSFER

The vision of transmitting power without using conducting wires can be dated back to the early 20<sup>th</sup> century, when Nikola Tesla first started to construct his famous Wardenclyffe Tower (Fig. 1.4) near Long Island Sound for broadcasting, wireless communication, and the transmission of wireless power in 1901 [1]. Tesla's work was impressive but due to lack of radio wave technologies at that time and the advancements made by Marconi with wireless signal transmissions, his experiment was seen as no longer worthy lost funding and thusly not successful even though he attempted to demonstrate its feasibility [7].



FIGURE 4 IMAGE OF THE TESLA TOWER, SHOREHAM, LONG ISLAND, NY, 1904. [11]

In the 1930s, a great deal of progress in generating high-power microwaves in the 1–10 GHz range was achieved by the invention of the magnetron and the klystron tubes. [16] After World War II, high-power and high-efficiency microwave tubes were advanced by the development of radar technology. [16] The power delivered to a receiver could be concentrated with microwaves. [16] WPT using microwaves is called microwave power transfer (MPT). [16] In the state-of-the-art, in order to improve the end-to-end power transfer efficiency, researchers' efforts were focused on enhancing the transmit efficiency, the receive efficiency, or both. To obtain higher transmit efficiency, the transmit antenna array must be designed such that the side lobes of its beam pattern are reduced to the lowest



acceptable level and that its main lobe keeps spillover losses to a minimum. [16] To this end, electronically steered phased arrays with retro directive beamforming have taken the place of traditional horn antennas and emerged as the most reliable technique to guarantee an accurate beam steering in WPT applications. [16]

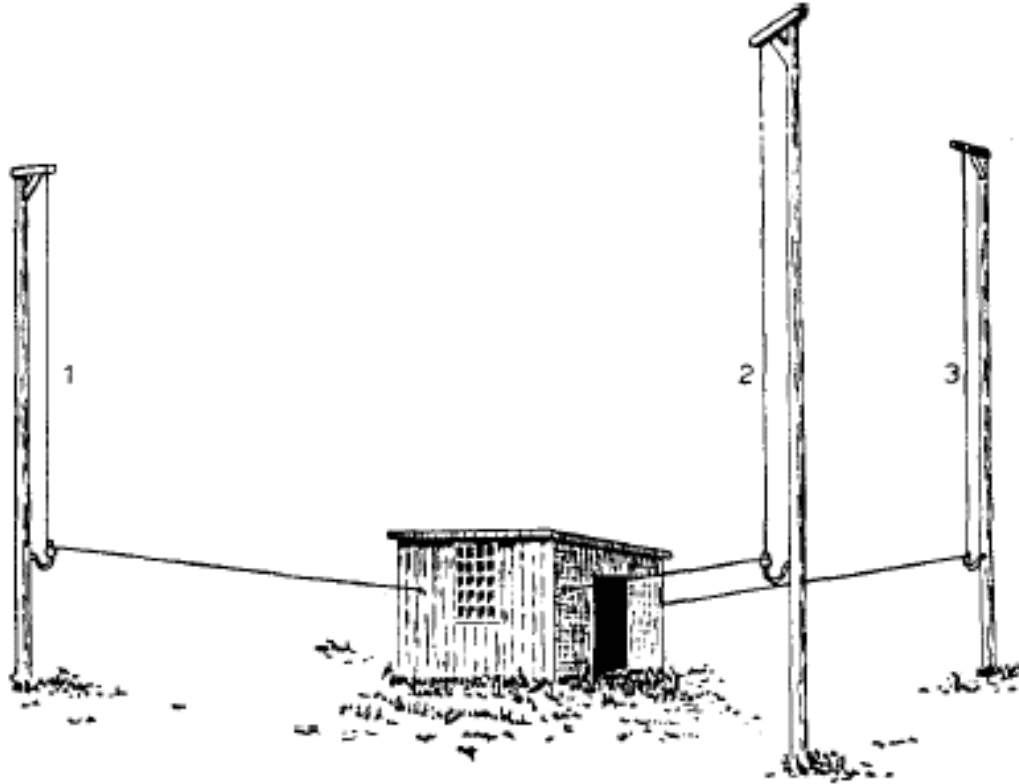
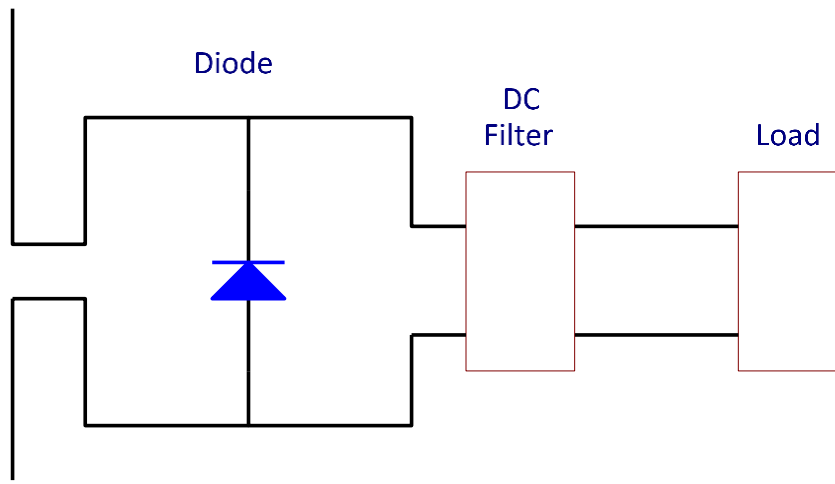


FIGURE 5 FERDINAND BRAUN'S PHASED ARRAY FROM 1905 [17]

On the other hand, attaining higher receive efficiency was attempted through the design of high-performance rectifying antennas (i.e., Rectenna).[16] In 1963 W.C. Brown developed a rectifying antenna, which he named a “Rectenna” for receiving and rectifying microwaves. [12] A Rectenna consists of an antenna, diode, and load, all in parallel, as shown in Fig 3-2. The electromagnetic wave induced into the antenna is rectified by the

diode and flows through a low-pass DC filter to the load. [12] This circuit acts as a diode clamp, raising the output DC voltage to as high as the peak input AC voltage. The efficiency of the first Rectenna was 50% at an output of 4 WDC and 40% at an output of 7 WDC, respectively. [12]

Antenna



Rectenna Circuit

FIGURE 6 SIMPLIFIED SCHEMATIC DIAGRAM OF RECTENNA CIRCUIT [12]

In the 1970s, Brown attempted to increase the total DC–RF–transfer–RF–DC efficiency using 2.45 GHz Microwaves [12]. The overall DC–DC efficiency was only 26.5% at an output of 39 WDC in the Marshall Space Flight Center tests of 1970 [BRO 73a]. In 1975, the overall DC–DC efficiency finally attained 54% at an output of 495 WDC using the Raytheon Laboratory magnetron [12]. In parallel, Brown, Richard Dickinson and his team succeeded in the largest MPT demonstration up to that time in 1975 at the Venus Site of the JPL Goldstone Facility Fig 3-3. The distance between the transmitting parabolic antennas, whose diameter was 26 m, and a Rectenna array, whose size was 3.4 m × 7.2 m,

was 1 mile. The transmitted 2.388 GHz microwave signal was 450 kW from the klystron and the rectified DC power achieved was 30kWDC with an 82.5% rectifying efficiency.



FIGURE 7 PICTURE OF FIRST GROUND-TO-GROUND MPT EXPERIMENT IN 1975 AT THE VENUS SITE OF THE JPL GOLDSTONE FACILITY [12]

Researchers often used 2.45 or 5.8 GHz frequencies of the industry, science and medical (ISM) band for MPT systems [2]. The push behind far-field power transfer comes from two major communities that have made significant contributions toward fulfilling Tesla's dream of wireless power: space-based solar power (SSP) or solar powered satellite (SPS) and RF identification (RFID). Though still in the experimental stage, researchers working in SPS have made advancements in energy conversion at great distances and high powers (greater than 1 W) to enable electricity to be shared via radio waves, namely collecting solar energy in orbital stations around earth and beaming it to ground stations via microwave power transfer. A simple example of multidirectional Far-Field transmission

would be in telecommunications, where a signal is transmitted over great distance, by means of a powerful transmitter emitting a signal in all directions, but the energy at the receiver needs only be large enough to distinguish the signal from the noise – much of the energy produced by the transmitter is dispersed and lost through radiation. Antennas from 300 MHz to 30 GHz are considered to be in the microwave frequency bands, see fig 2-2. Antennas that use the microwave or higher frequency range can be physically small size. Microwave signals travel by line of sight and are not bent by the ionosphere as are lower frequency signals. Satellite and terrestrial communication links with very high capacities are therefore possible, with frequency reuse at minimally distant locations. [17] Frequency reuse is the process of using the same radio frequencies on radio transmitters site within a geographic area that are separated by a sufficient distance to cause minimal interference with each other. [17]

## 1.6 NEAR FIELD POWER TRANSFER

Nearly all wireless power transfer (WPT) techniques use near-field electromagnetic induction, which can be divided into two methods: magnetic induction (or inductive power transfer—IPT) and electrostatic induction (or capacitive power transfer—CPT) [2]. IPT is the most common and is applicable to many power levels and gap distances. Conversely, CPT is only applicable for power transfer applications with inherently small gap distances due to constraints on the developed voltage [1]. Despite limitations on gap distance, CPT has been shown to be viable in kilowatt power level applications [1]. The first public WPT

demonstration to power a “commonplace” load was capacitive coupling to tube lighting by Tesla in 1891 [1].

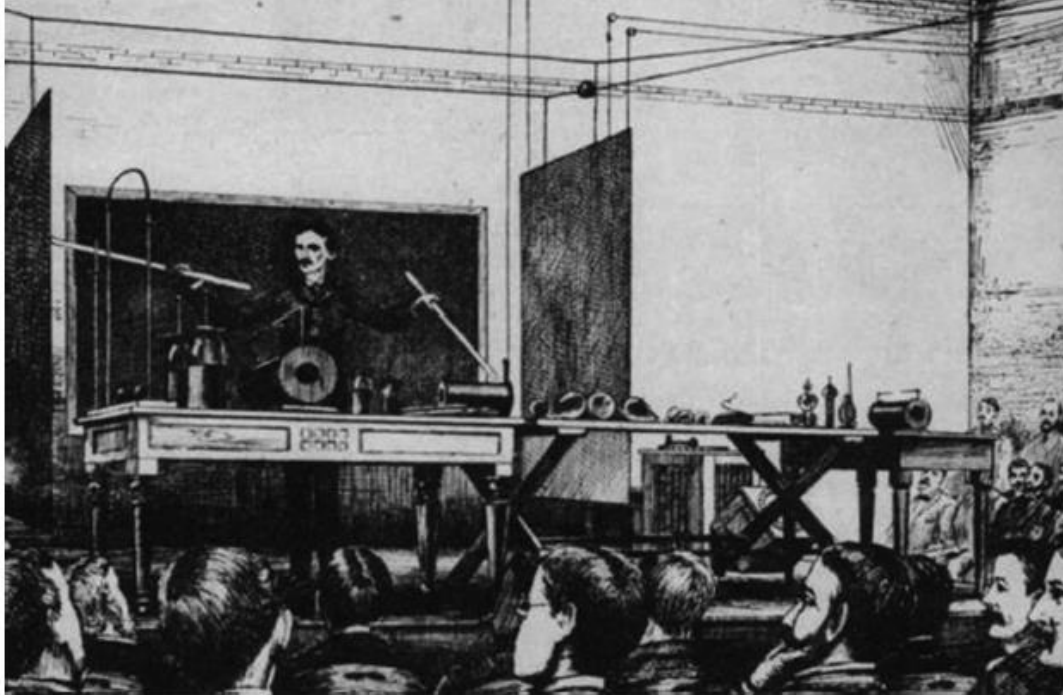


FIGURE 8 PICTURE OF TESLA DEMONSTRATING WIRELESS POWER TRANSMISSION USING CAPACITIVE COUPLING AT COLUMBIA, NEW YORK, IN 1891 [8]

Although CPT is developing quickly, it is perceived as only suitable for low power levels over short transfer distances, while IPT is for low to high power levels spanning a larger distance range [1]. Compared with the IPT system, the CPT system has many advantages [1]. Magnetic fields are sensitive to nearby metal objects, and the system efficiency drops quickly with this interference [18]. They also generate eddy current losses and, hence, heat in a conductive object, which creates a potential fire hazard [18]. However, the electric field in the CPT system does not generate significant losses in the metal objects [18].

These categories can be further broken down to include the near-field types; magnetic resonance, inductive coupling and electrostatic induction [2]. Electromagnetic induction

over a distance was demonstrated shortly thereafter (again by Tesla) and proved to be more versatile for wireless power applications.

## 1.7 SUMMARY

Both Near and Far-Field power transmission can operate at any frequency, within the wavelength parameter limitations defined above, based on topology and power levels used. Eventually, these techniques evolved into wireless communications [1]. Far field transmissions would include laser-based optical power transmission and RF/microwave energy transmission, only RF/microwave and laser-based systems are truly long range methods [15]. Since near Field and Far Field power transfer are not only a function of the distance between the antennae but also a function of the frequency used.

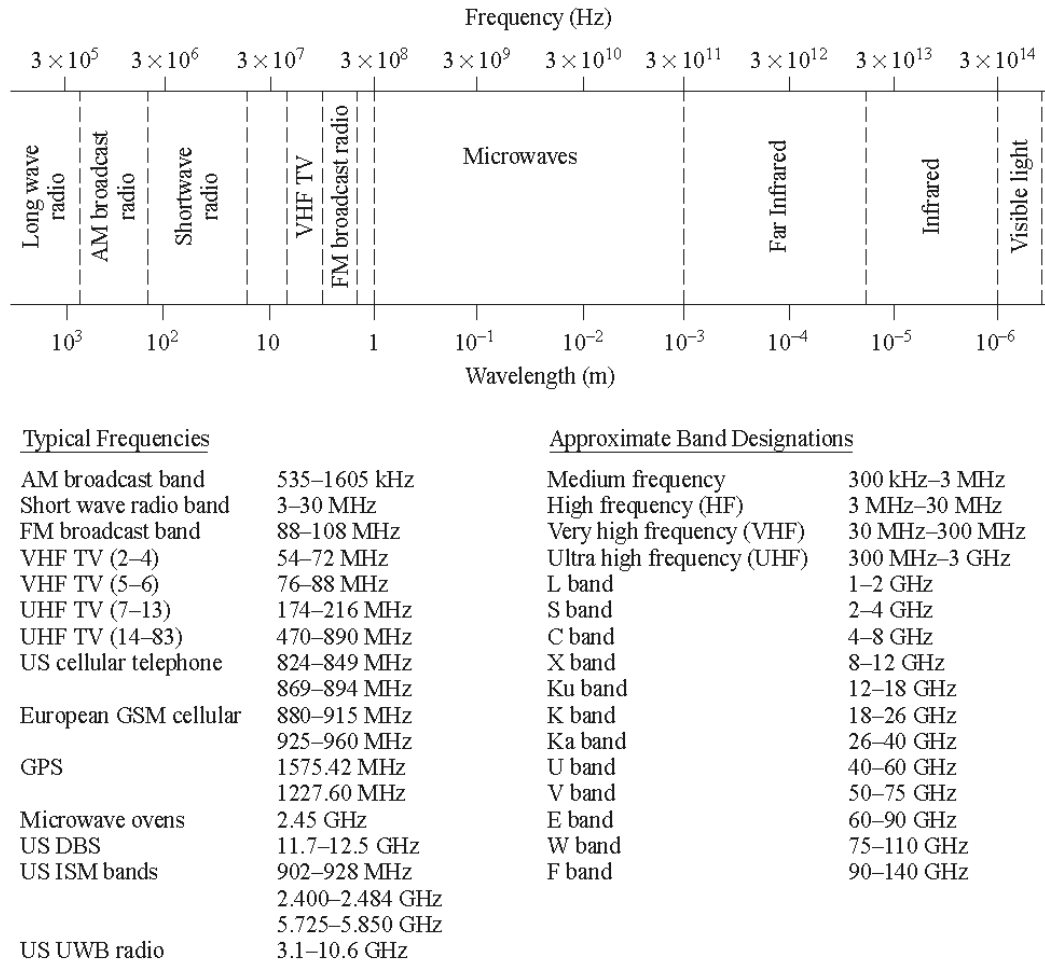


FIGURE 9 DIAGRAM SHOWS THE ELECTROMAGNETIC FREQUENCY SPECTRUM [17]

The electromagnetic spectrum represents all of the possible frequencies of electromagnetic energy [17]. It ranges from extremely long wavelengths (extremely low frequency exposures such as those from power lines) to extremely short wavelengths (x-rays and gamma rays) and includes both non-ionizing and ionizing radiation [17].

Figure 1.8 below is a diagram of the classification of the various Wireless Power Transfer Technologies.

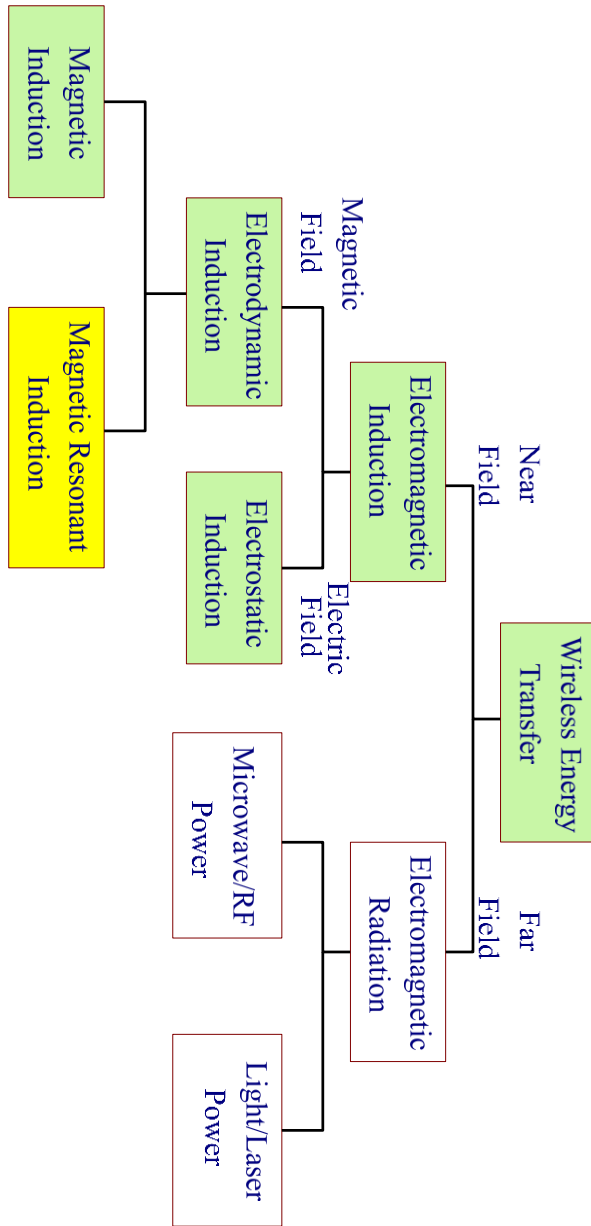


FIGURE 10 DIAGRAM SHOWING CLASSIFICATION OF WIRELESS ENERGY TRANSFER TECHNOLOGIES

There are several advantages and disadvantages to the various WPT technologies. Table 1-1 below is a detailed summary of the differences discussed in this chapter and the applications where they might be used.



TABLE 1-1 SUMMARY WPT TECHNOLOGIES

WPT Technology		Advantages	Disadvantages	Applications
<b>EM radiation</b>	Omni-directional	Able to maintain RF/DC conversion efficiency over a wide range of operating conditions including input and output power load resistance variations	Dramatic falling of power transfer efficiency over distance and appropriate only for ultralow power sensors.	Charging a wireless sensor network (WSN) for environmental monitoring (temperature, moisture, light etc.).
	Uni-directional (microwave / laser)	High power transmission efficiency over long distance (kilo meter range)	Require LOS and sophisticated tracking & alignment mechanism, inherently large scale of devices.	SHARP unmanned plane.
<b>EM induction coupling</b>		Non-radiative, simple and high power transfer efficiency in centimeter range.	Short transmission distance and require accurate alignment in the charging direction.	Charging pad for cell phones and laptops, electric toothbrush, etc.
<b>Inductive Power Transfer by Magnetic resonant coupling</b>		Effective transfer efficiency over several meters under Omni-direction. No need of LOS and insensitive to weather condition.	Drop of efficiency due to orientation, axial mismatch between transmitter & receiver and interference. Core design critical to prevent saturation	Charging mobile devices, electric vehicles, implantable devices and wireless sensor networks.
<b>Capacitive Power Transfer</b>		Insensitive friendly metals, capable of very high power and high frequency	Short transmission distance gap distances, mm range, voltage has an electric field strength of about $3 \times 10^6$ V/m or 3 kV/mm), air can begin to break down	Charging mobile devices, electric vehicles, implantable devices and wireless sensor networks.

## Chapter 2. NEAR FIELD POWER TRANSFER

### 2.1 INTRODUCTION

In this chapter two types of near field wireless power are examined both with the same 1mm gap between the two to determine any practical limitations or advantages one may have over the other. Since WPT over small distances can be performed by either Capacitive Power Transfer, CPT, or Inductive Power Transfer, IPT, we can examine their relationships and similarities[1]. First both types are introduced, the IPT in the shape of cup core transformer arrangement and the CPT in the form 2 plates. Next cup core IPT design energy density is examined in detail and expressed with appropriate calculations. The plate design CPT energy density is examined in detail and expressed with appropriate calculations. The volume of the IPT cup core design is examined in detail and expressed with appropriate calculations to determine the relative size of the core for a given power density. Finally an analytical comparison of the IPT vs CPT is discussed.

### 2.2 POWER DENSITY

Power density is defined as the throughput power divided by the coupler volume (including the gap) [1]. To simplify the comparison between IPT and CPT, coupler power density is investigated rather than the overall system volume [1]. To compare the power density, the gap energy density of the magnetic field and electric field is compared first (i.e., the electric/magnetic energy that can be stored in the gap volume) [1]. Then, the gap power density is used as an intermediate variable to establish a relationship between the air gap power and coupler volume [1]. The IPT and CPT coupler geometries for analysis are

illustrated in Fig. 7 with dimensional definitions assigned to calculate the volumes  $V_{\text{gap}}$  and  $V_{\text{coupler}}$  [1].

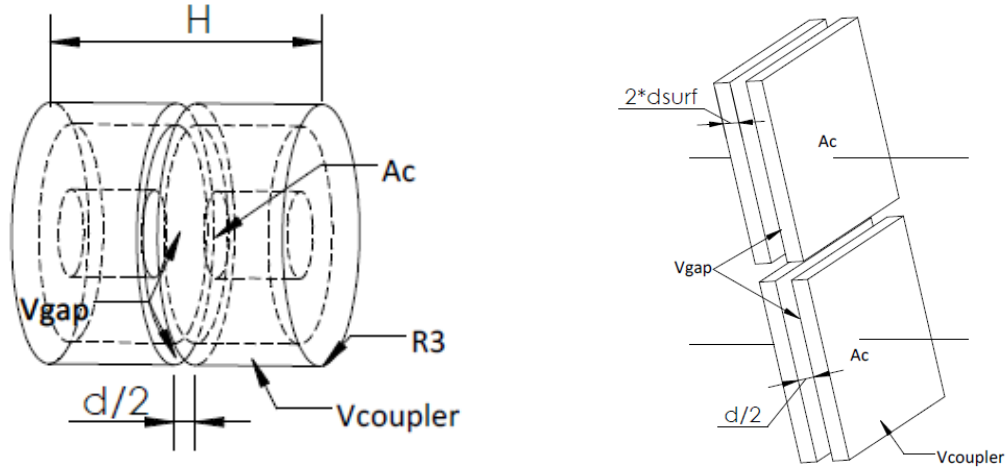


FIGURE 11 GAP VOLUME AND COUPLER VOLUME. (A1) INDUCTIVE POWER TRANSFER COUPLER. (A2) CAPACITIVE POWER TRANSFER COUPLER. [1]

Both IPT and CPT facing areas are defined as cross sectional area  $A_c$ , separated by a Gap of  $d$ , with both structures perfectly aligned. [1] Looking at both from a small gap scenario the IPT is functionally a gapped transformer and modeled as two pot cores with identical center posts and back iron areas. [1] The CPT couplers consist of two sets of parallel plates of identical surface area separated by a gap. See Fig. 2.1.

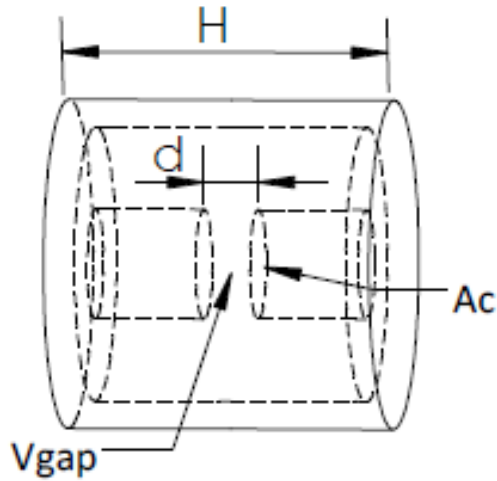


FIGURE 12 INDUCTIVE POWER TRANSFER TWO POT CORES [1]

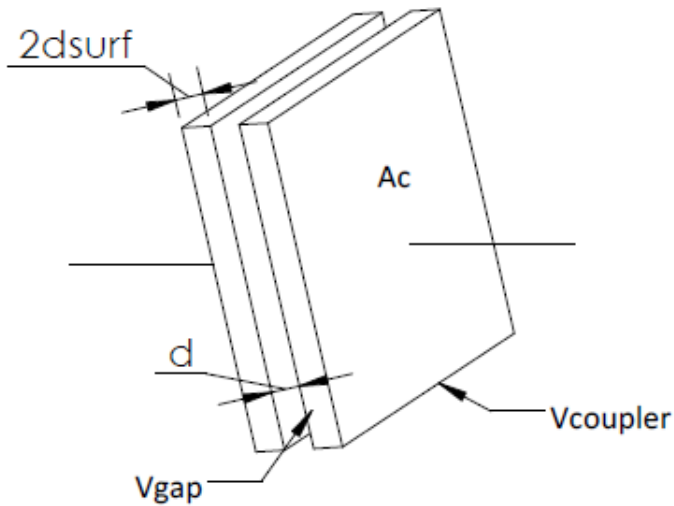


FIGURE 13 CAPACITIVE POWER TRANSFER ONE SET OF PARALLEL PLATES [1]

It should be noted that for the CPT coupler, each of the square surfaces can be replaced by a stacked surface of  $N$ -layers ( $N=3$ ) in Fig. 2.5. As illustrated, the gap is divided into five pairs, and the surface thickness can be decreased to  $1/3$  as well. Although this is a different form factor, the total volume is unchanged.

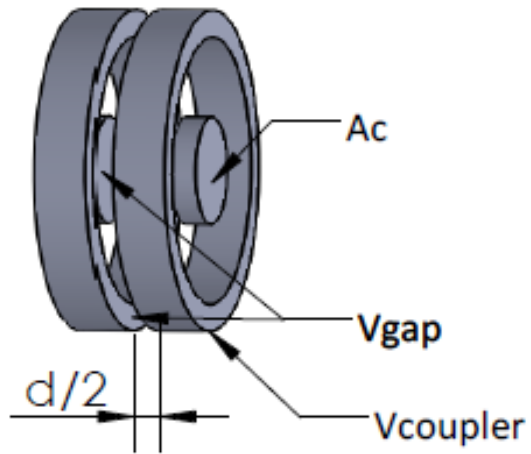


FIGURE 14 3D CUT VIEW OF INDUCTIVE POWER TRANSFER TWO POT CORES [1]

COUPLER VOLUME

$$V_{\text{coupler}} := \pi \cdot R_3^2 H \quad (2-1)$$

GAP VOLUME

$$V_{\text{gap}} := A_c \cdot d \quad (2-2)$$

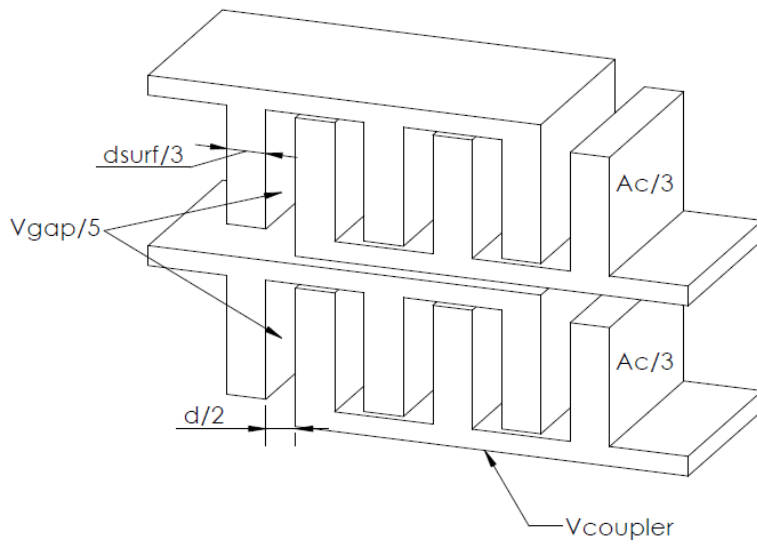


FIGURE 15 3D MODEL VIEW OF PARALLEL PLATES[1]

## COUPLER VOLUME

$$V_{\text{coupler}} := A_c \cdot (d + 4d_{\text{surf}}) \quad (2-3)$$

GAP VOLUME IS DETERMINED IN THE SAME MANNER AS GAP VOLUME FROM EQUATION  
2-3 ABOVE

$$V_{\text{gap}} := A_c \cdot d \quad (2-4)$$

The comparison may be more transparent if the couplers are redrawn from their actual implementation by lumping gaps and surface thicknesses together as in Fig. 2.3 and 2.5. Determining the volume of a CPT coupler is relatively straightforward. It is the sum of the gap volume and the volume of the coupling plates. IPT is less transparent; the core must be sized to accommodate space for windings, while simultaneously directing magnetic flux at a reasonable density in a closed path. For an IPT coupler, a spiral winding and pot core in Fig. 2.2 is modeled in the same fashion as in Fig. 2.4, just by increasing  $R_w$  and decreasing  $h_1$ . Ultimately, different dimensional permutations may be fed into these volume models suitable for analyzing coupler power density [1].

## 2.3 IPT GAP ENERGY DENSITY

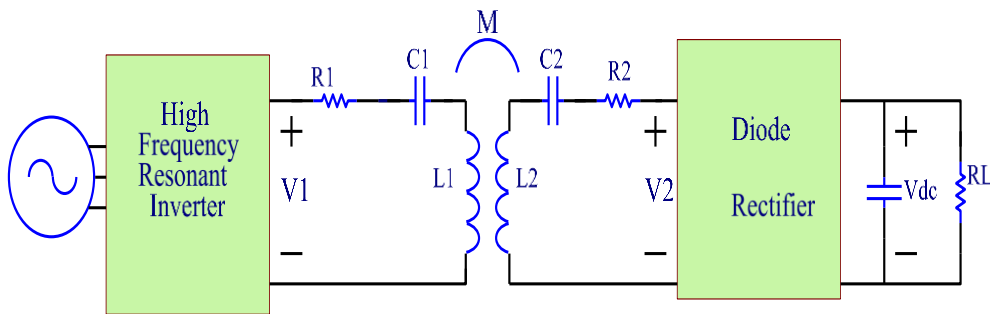


FIGURE 16 SIMPLIFIED SCHEMATIC OF TYPICAL INDUCTIVE POWER TRANSFER  
TOPOLOGY

Field energy is stored in the gap [1]. For the IPT system specified here, it is assumed that the current is purely sinusoidal with the peak value of  $I_L$ . The inductive reactive power and the power density are [1];

FIELD ENERGY IN THE GAP [1]

$$Q_{\text{gap}} := \omega \cdot C \cdot U_{C_{\text{rms}}}^2 \quad (2-5)$$

FIELD ENERGY IN THE GAP [1].

$$Q_{\text{gap}} := \pi \cdot f_{\text{sw}} \cdot \varepsilon_0 \cdot \varepsilon_r \cdot A_c \cdot d \cdot E_{C_{\text{max}}}^2 \quad (2-6)$$

GENERAL EQUATION FOR POWER DENSITY [1].

$$\rho_c := \frac{Q_{\text{gap}}}{V_{\text{gap}}} \quad (2-7)$$

SUBSTITUTION OF  $Q_{\text{GAP}}$  AND  $V_{\text{GAP}}$  IN POWER DENSITY EQUATION [1].

$$\rho_c := \pi \cdot f_{\text{sw}} \cdot \varepsilon_0 \cdot \varepsilon_r \cdot E_{C_{\text{max}}}^2 \quad (2-8)$$

The displacement  $D_C$  max or electric field  $E_C$  max limits the current integration over time (A/Hz) as specified in (6) [28]. This reflects the physical duality between IPT and CPT: IPT—magnetic flux, CPT—electric charge.

ELECTRIC FIELD  $E_C$  MAX BASED ON IPT [1].

$$D_{C_{\text{max}}} := \varepsilon_0 \cdot \varepsilon_r \cdot E_{L_{\text{max}}} \quad (2-9)$$

ELECTRIC FIELD EC MAX BASED ON CPT [1].

$$D_{C\_max} := \frac{1}{A_c} \frac{I_{C\_max}}{2\pi \cdot f_{sw}} \quad (2-10)$$

SIMPLIFICATION OF POWER DENSITY [1].

$$\rho_c := \pi f_{sw} \cdot \frac{D_{C\_max}^2}{\epsilon_0 \cdot \epsilon_r} \quad (2-11)$$

The maximum magnetic field  $H_{L\_max}$  or induction  $B_{L\_max}$  is limited by the voltage integration over time (V/Hz), a familiar condition in inductive systems as described by

MAXIMUM MAGNETIC FIELD AS A FUNCTION OF MAGNETIC FIELD STRENGTH "H" [1].

$$B_{L\_max} := \mu_0 \cdot \mu_r \cdot H_{L\_max} \quad (2-12)$$

SIMPLIFICATION OF MAXIMUM MAGNETIC FIELD [1].

$$B_{L\_max} := \frac{1}{A_c} \cdot \frac{U_{L\_max}}{2\pi f_{sw}} \quad (2-13)$$

These formulae reveal the limiting factors concerning IPT throughput power. Namely, the power density is limited by the operational frequency and maximum flux density (energy stored in the gap) [1]. Operational frequency is determined by the loss characteristics of the power electronic drive circuitry and the coupler core (back iron) material [1]. Additionally, the saturation properties of the core limit the peak value of flux density [1]. Commonly used core materials such as ferrite or powdered iron regularly achieve flux densities of 0.2 T with core losses of 3MW/m<sup>3</sup> and 10 MW/m<sup>3</sup>, respectively, at a frequency



of 500 kHz [1]. Depending on specific operating conditions, either saturation or core losses will determine the maximum flux density [1].

## 2.4 CAPACITIVE POWER TRANSFER GAP ENERGY DENSITY

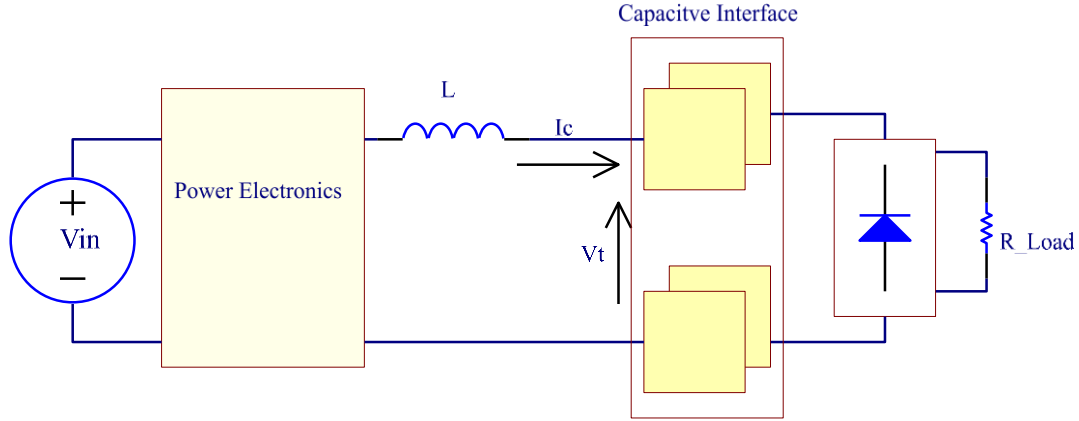


FIGURE 17 SIMPLIFIED SCHEMATIC OF TYPICAL TOPOLOGY FOR CAPACITIVE POWER TRANSFER [19]

Similarly to IPT, the field energy is stored in the coupler gap. Unlike IPT, however, there is no core or back iron needed in a CPT system. Electric field lines terminate on charge and due to the cancellation of the field outside the coupling plates, a “back iron” pathway is not required. Thus, for a CPT system, the coupler volume will be only slightly larger (an integer multiple) than the gap itself. For the CPT system specified here, it is assumed that the voltage on the coupling capacitor is purely sinusoidal with a peak value of  $U_C$ . The capacitive reactive power and the power density are

INDUCTIVE ENERGY STORED IN THE GAP [1].

$$Q_{\text{gap}} := \omega \cdot L \cdot I_{L_{\text{rms}}}^2 \quad (2-14)$$

INDUCTIVE ENERGY STORED IN THE GAP [1].

$$Q_{\text{gap}} := \pi f_{\text{sw}} \cdot \mu_0 \cdot \mu_r \cdot A_c \cdot d \cdot H_{L\_max}^2 \quad (2-15)$$

INDUCTIVE POWER DENSITY [1].

$$\rho_L := \frac{Q_{\text{gap}}}{V_{\text{gap}}} \quad (2-16)$$

INDUCTIVE POWER DENSITY EXPANDED [1].

$$\rho_L := \pi f_{\text{sw}} \cdot \mu_0 \cdot \mu_r \cdot H_{L\_max}^2 \quad (2-17)$$

INDUCTIVE POWER DENSITY SIMPLIFIED [1].

$$\rho_L := \pi f_{\text{sw}} \cdot \frac{B_{L\_max}^2}{\mu_0 \cdot \mu_r} \quad (2-18)$$

Much like IPT, CPT power density is limited by the operational frequency and gap displacement field strength. Without any core material or back iron as in IPT, the operational frequency is limited essentially by the power electronic drive circuitry because air gap losses are negligible. A limit on maximum field strength does exist, in the form of electric breakdown, rather than saturation [20], [21]. Although air is normally an excellent insulator, when stressed by a sufficiently high voltage (an electric field strength of about  $3 \times 10^6$  V/m or 3 kV/mm), air can begin to break down, becoming partially conductive. Across relatively small gaps, breakdown voltage in air is a function of gap length time's pressure.

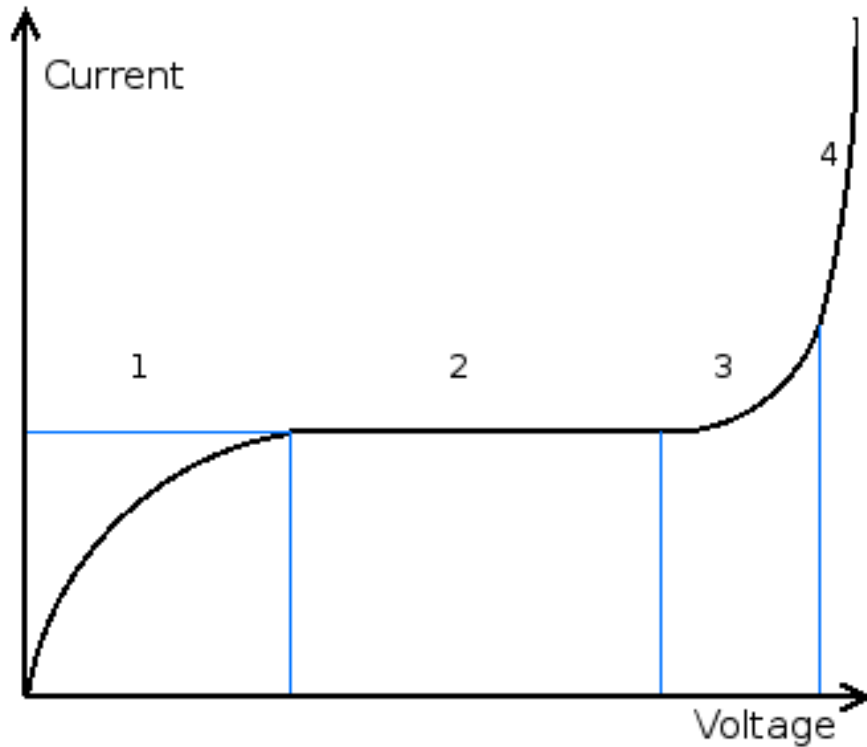


FIGURE 18 GRAPH ILLUSTRATING THE RELATIONSHIP BETWEEN VOLTAGE AND CURRENT

Before gas breakdown, there is a non-linear relation between voltage and current as shown in the figure 11. In region 1, there are free ions that can be accelerated by the field and induce a current. These will be saturated after a certain voltage and give a constant current, region 2. Region 3 and 4 are caused by ion avalanche as explained by the Townsend discharge mechanism. This electric field strength is also indicative of why CPT is generally not utilized for applications with gap distances  $>1$  mm, the resultant voltage between the transmitter and receiver plates is large. The field strength for CPT may be pushed higher in applications residing in vacuum or possibly when coatings are utilized to prevent a direct galvanic path between plates during gap (air) breakdown.

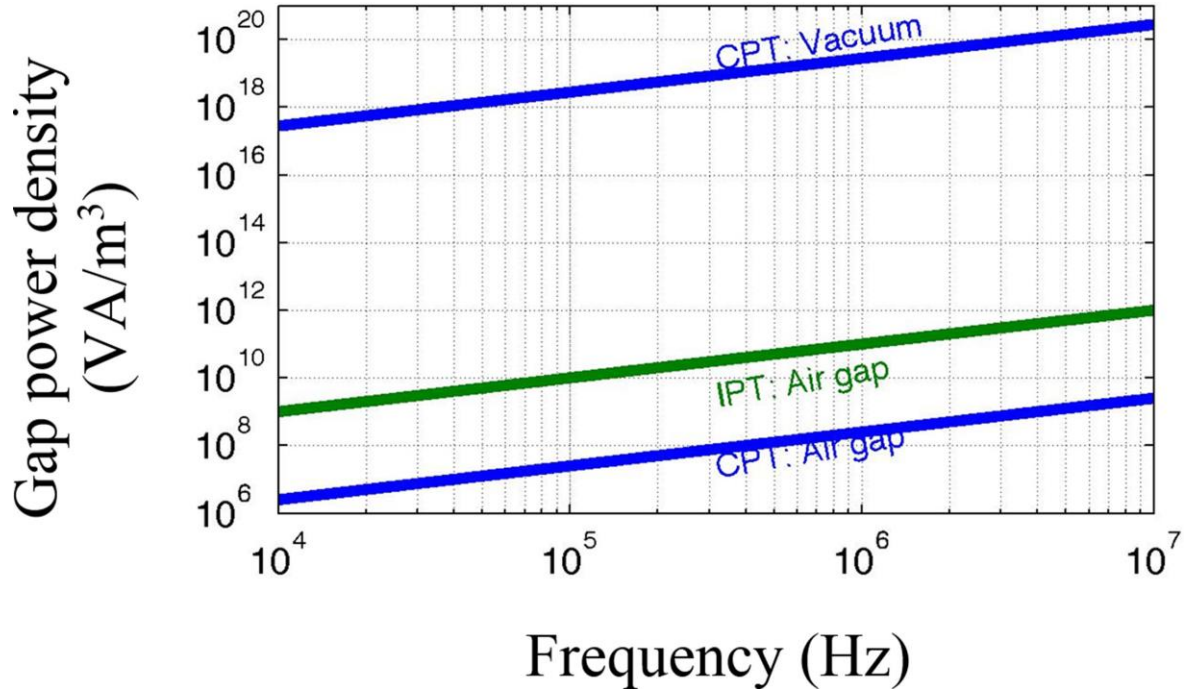


FIGURE 19 GRAPH OF GAP POWER DENSITY [1].

Figure 2-9 plots the gap power density to compare IPT and CPT. The gap power density of the IPT system is substantially higher ( $\sim 400\times$  larger) than CPT while operating in air. For further comparison, in vacuum the electric field strength may be much higher, allowing CPT to increase power density, while IPT is still limited by its core material. For a more complete picture of IPT and CPT power density, a thorough analysis of the coupler itself is needed. The gap volume is not the total volume; thus, the following section calculates and compares the volume of the couplers by including the core, windings, plate thickness, etc.

## 2.5 WPT COUPLER VOLUME CALCULATIONS

**IPT Coupler Size:** According to Fig. 2.9, the magnetic flux passes through three areas in the core, the center post  $\pi R_1^2$ , back iron  $2\pi R_1 h_2$ , and the core edge  $\pi (R_3^2 - R_2^2)$ . To prevent the flux density in the core from saturation, these three areas should be the same as defined in

#### AREA OF CENTER POST

$$A_c := \pi R_1^2 \quad (2-19)$$

#### AREA OF BACK IRON

$$A_c := 2\pi R_1 \cdot h_2 \quad (2-20)$$

#### AREA OF CORNER EDGES

$$A_c := \frac{\pi}{R_3^2 - R_2^2} \quad (2-21)$$

Using the geometric definitions in Table 2-1, the total IPT coupler volume  $V_{\text{coupler}}$  can be written as

#### VOLUME OF COUPLER

$$V_{\text{Coupler}} := \left( 2h_1 + 2h_2 + \frac{d}{2} \right) \left[ 2A_c + \pi (R_2^2 - R_1^2) k_c \right] \quad (2-22)$$

TABLE 2-1 TABLE OF WPT COUPLER GEOMETRY RELATIONSHIPS

	Name	Symbol	Expression (IPT)	Expression (CPT)
Common Parameters	Gap distance	d	d	A <sub>c</sub>
	Cross-sectional area	A <sub>c</sub>	$\pi R^2$	
	Gap geometry ratio	r <sub>g</sub>	$\frac{d}{\sqrt{A_c}}$	
Inductive Power Transfer Parameters	Winding area	A <sub>w</sub>	2h <sub>l</sub> *R <sub>w</sub>	-
	Winding-core ratio	r <sub>A</sub>	$\frac{A_w}{A_c}$	-
	Winding area Geometry ratio	r <sub>w</sub>	$\frac{R_w}{h_l}$	-
Capacitive Power Transfer Parameters	Surface Thickness	d <sub>surf</sub>	-	d <sub>surf</sub>
	Thickness Ratio	R <sub>c</sub>	-	d <sub>surf</sub> /d

Note that the factor k<sub>c</sub> (~1:1.1) is introduced to fulfill the extra volume that may be caused by the non-ideal core shape (e.g., oversizing the core for winding area, saturation prevention area, etc.) Next, V<sub>coupler</sub> expressed in (8) may be normalized to the gap volume V<sub>gap</sub> and after algebraic simplification, [13]

$$\frac{V_{\text{Coupler}}}{V_{\text{gap}}} = \left[ \frac{2}{r_g} \left( \sqrt{\frac{r_A}{2r_w}} + \sqrt{\frac{1}{4\pi}} \right) + \frac{1}{2} \right] \left[ 2 + \pi \left( \sqrt{\frac{2r_A \cdot r_w}{\pi}} + \frac{r_A \cdot r_w}{2} \right) \right] k_c \quad (2-23)$$

Ultimately, the above suggests that IPT possesses greater power density with lower r<sub>A</sub>, which is intuitive because relative coupling area increases as r<sub>A</sub> decreases. The empirical

value for  $r_A$  should be around 0.5–2 [22], [23]. However, the coupling area has an important impact on the parameter  $r_g$ , which is a significant factor affecting IPT coupler volume. With a small gap and large cross-sectional area (i.e., smaller  $r_g$ ), the core may be easily saturated. Increasing the gap and decreasing the cross-sectional area will reduce this issue but the larger gap will cause the coupling factor to drop. Empirical values for  $r_g$  are typically 0.01–0.1 (e.g., For a 1-mm gap, the cross-sectional area is usually around 1–100 cm<sup>2</sup>, and the gap volume is 0.1–10 cm<sup>3</sup>) [24]. For every  $r_A$  and  $r_g$ , there is an optimal  $r_w$  to minimize  $V_{\text{coupler}}$  according to equation above. Fig. 11 plots  $V_{\text{coupler}}$  normalized to  $V_{\text{gap}}$  (i.e., the coupler to gap volume ratio). As plotted in Fig. 11(a), the optimized  $r_w$  is generally between 0.1 and 1. For a spiral winding, the shape of the winding has larger area ( $R_w$  is high) and reduced depth ( $h_1$  is small); therefore,  $r_w = (R_w/h_1)$  is very high (e.g., >10), increasing coupler volume to be larger than optimal, as shown in Fig. 11(b). For a general small gap, IPT coupler of the pot core design herein, the ratio  $V_{\text{coupler}}/V_{\text{gap}}$  can be optimized to  $\sim 100$ , and a typical value is  $\sim 500$ . For example, a 1-mm gap (d), 10 cm  $\times$  10 cm cross-sectional area (AC) coupler, at frequency 1 MHz,  $V_{\text{coupler}}/V_{\text{gap}} = 498$ .

2) CPT Coupler Size: Calculating  $V_{\text{coupler}}$  is easier for CPT since it has the advantage of being coreless. The only difference between gap volume and the coupler volume is the thickness of the conductive plate surfaces. The surface should be thick enough to carry current efficiently ( $J_{\text{max}} < 5 \text{ A/mm}^2$ ). Also, its thickness should be manufactured practically (e.g., aluminum foil thickness  $d_{\text{Al}} = 0.025 \text{ mm}$ ). The CPT coupler models are shown in Fig. 9(c2). Similar to the IPT coupler, a factor  $k_C > 1$  is used to fulfill an operational safety or manufacturability margin for extra coupling plate thickness should it be desired.

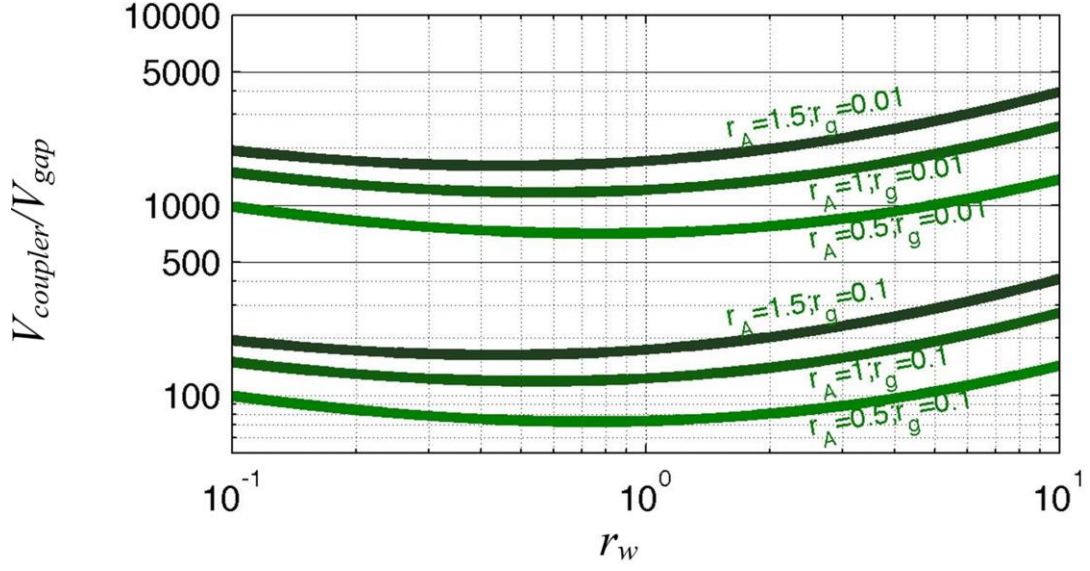


FIGURE 20 COUPLER VOLUME OPTIMIZATION. (A) OPTIMIZATION OF  $r_w$  (WITH  $r_A$   $r_g$  FIXED) [1]

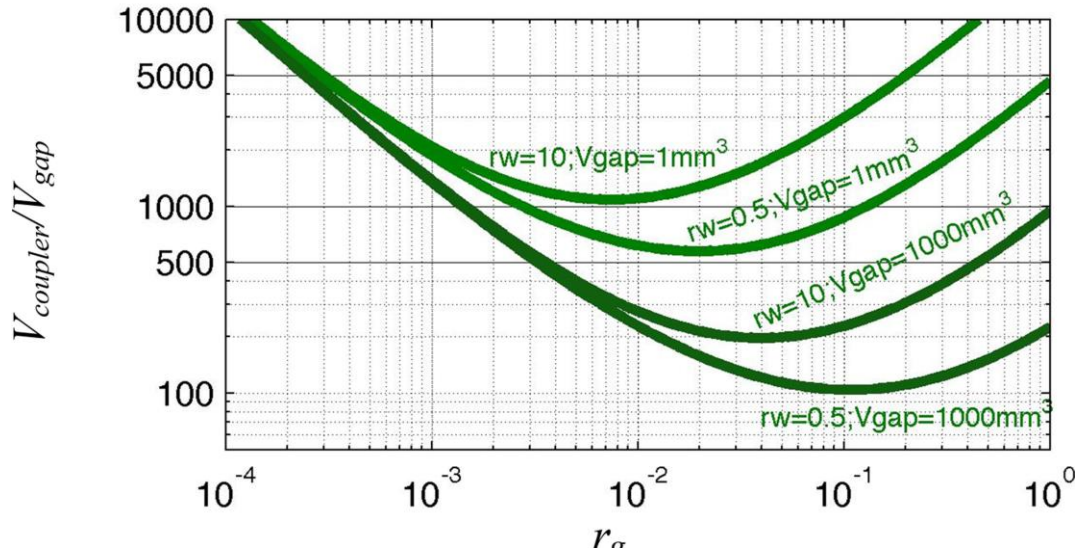


FIGURE 21 COUPLER VOLUME WITH DIFFERENT GAP RATIO  $r_g$  [1].

$B_{\text{sat}} = 0.2 \text{ T}$ ,  $k_w = 0.2$ ,  $J_{\text{max}} = 5 \text{ A/mm}^2$ ,  $k_c = 1$

The surface thickness  $d_{\text{surf}_e}$  for a square surface planar coupler may be sized using

$$I_c = J_{\text{max}} \cdot d_{\text{surf}_e} \cdot \sqrt{A_c} \quad (2-24)$$

$$I_c = \frac{1}{\sqrt{2}} \cdot E_{\text{max}} \cdot \omega \varepsilon \cdot A_c \quad (2-25)$$



After solving for  $d_{\text{surf\_e}}$ , and substitution into the ratios in Table 2-1, the minimum surface thickness to satisfy electrical constraints is written as

$$d_{\text{surf\_e}} = \frac{E_{\text{max}} \cdot \omega \varepsilon \cdot \sqrt{A_c}}{\sqrt{2} J_{\text{max}}} \quad (2-26)$$

$$d_{\text{surf\_e}} = \frac{E_{\text{max}} \cdot \omega \varepsilon}{\sqrt{2} J_{\text{max}}} \cdot \left( \frac{V_{\text{gap}}}{r_g} \right)^{\frac{1}{3}} \quad (2-27)$$

Usually there are mechanical constraints as well, imposing a minimum thickness ( $d_{\text{min}}$ ) that can be manufactured. For off-the-shelf foils, the mechanical thickness is suitably large to satisfy electrical requirements. Assume  $d_{\text{surf\_m}} = d_{\text{min}} = 0.025$  mm, which is the thickness of standard metal foils ( $\sim 0.001$  in). The thickness ratio in Table III is written as

$$r_C = \max \left( \frac{d_{\text{surf\_e}}}{d}, \frac{d_{\text{surf\_m}}}{d} \right) \quad (2-28)$$

$$r_C = \max \left( \frac{E_{\text{max}} \cdot \omega \varepsilon}{\sqrt{2} J_{\text{max}}} \cdot \frac{1}{r_g}, \frac{d_{\text{min}}}{d} \right) \quad (2-29)$$

The coupler to gap volume ratio is (15) after substitution of (14) into the coupler volume equation in Fig. 2.11

$$\frac{V_{\text{coupler}}}{V_{\text{gap}}} = (1 + 4r_C) k_C \quad (2-30)$$

$$\frac{V_{\text{coupler}}}{V_{\text{gap}}} = \left( 1 + \max \left( \frac{2\sqrt{2} E_{\text{max}} \cdot \omega \varepsilon}{J_{\text{max}} \cdot r_g}, \frac{4d_{\text{min}}}{d} \right) \right) \cdot k_C \quad (2-31)$$

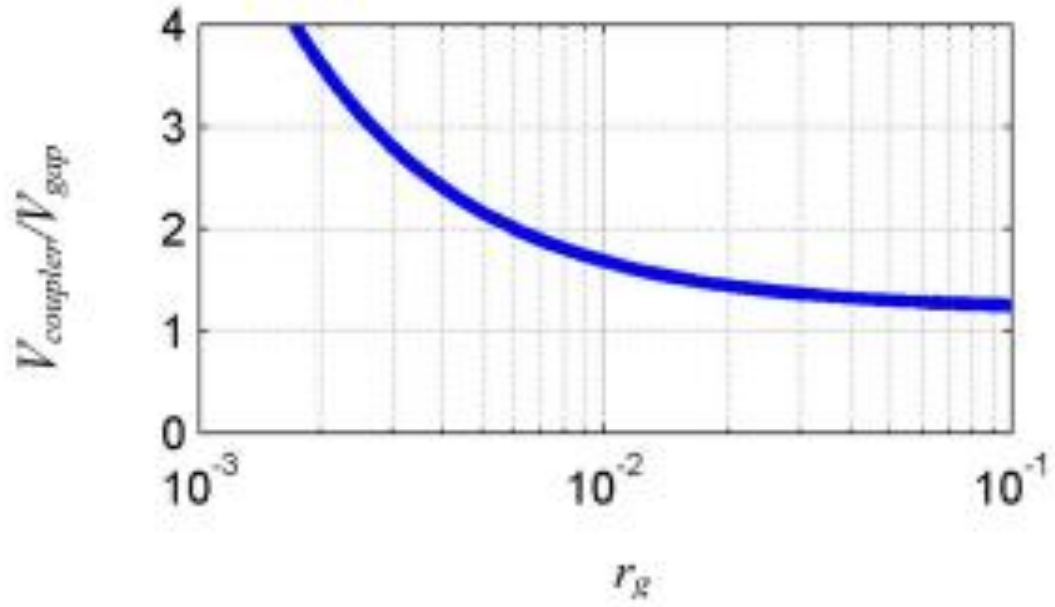


FIGURE 22 COUPLER/GAP VOLUME RATIO VERSUS GAP/AREA RATIO: [1]

$E_{max} = 3\text{MV/m}$ ,  $J_{max} = 5\text{ A/mm}^2$ ,  $f_{sw} = 1\text{ MHz}$ ,  $k_C = 1.2$ ,  $A_C = 0.1\text{ m}^2$ .

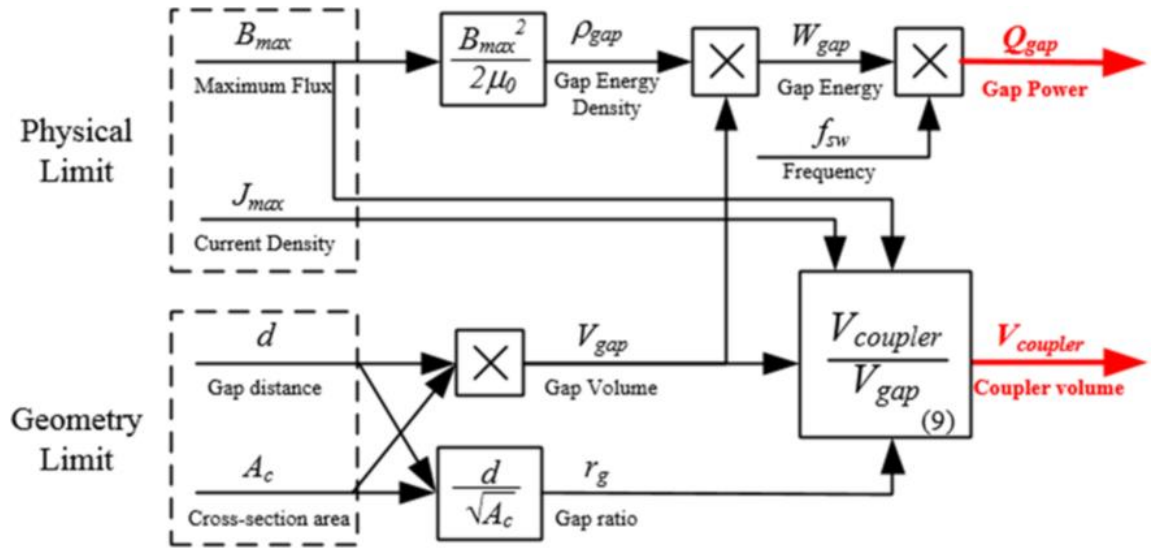


FIGURE 23 INDUCTIVE POWER DENSITY AND TRANSFER ANALYSIS CHART [1].

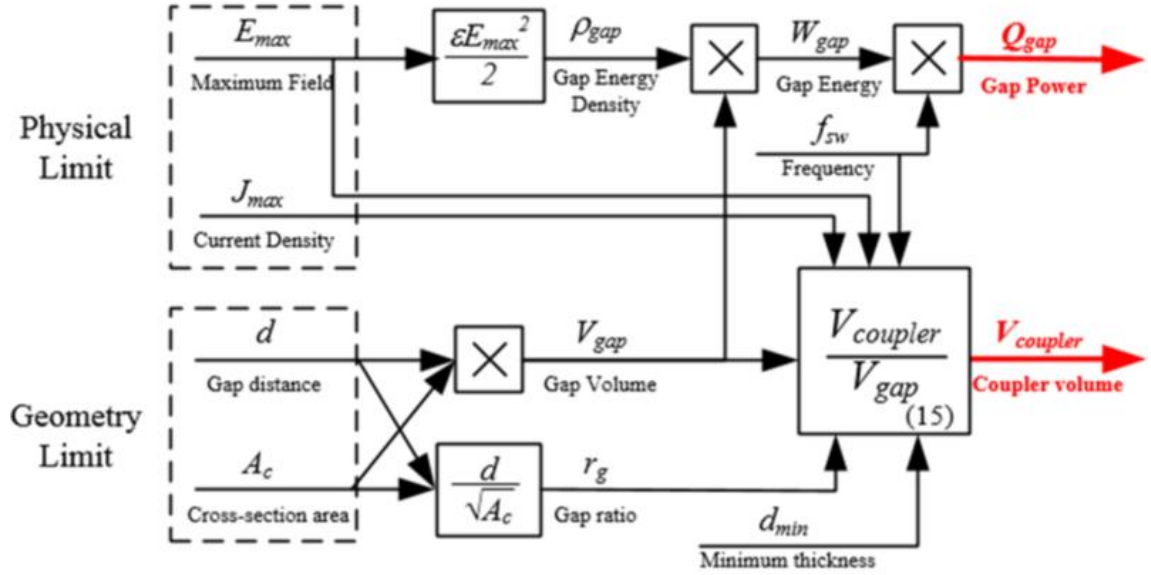


FIGURE 24 CAPACITIVE POWER DENSITY AND TRANSFER ANALYSIS CHART [1].

As shown in Fig. 2.14, the volume ratio can be optimized to  $k_c$  (e.g.,  $\sim 1.2$ ), and the general value can be set to be  $(1-4) k_c$ . As an example, a 1-mm gap ( $d$ ), 10 cm  $\times$  10 cm cross sectional area ( $A_c$ ) coupler, at frequency 1 MHz, if  $k_c = 1.2$ ,  $V_{\text{coupler}}/V_{\text{gap}} = 1.68$ .

## 2.6 ANALYTICAL COMPARISON OF INDUCTIVE AND CAPACITIVE POWER TRANSFER

Given the physical limitations of permeable material and air, along with volumetric constraints, an analysis of air gap power density and coupler volume for IPT and CPT was performed. Each coupling techniques' respective calculation process is documented in block diagrams form in Figs. 2.13 and 2.14. Calculation blocks within the diagram refer back to the equations in the previous sections (equation numbers in lower right-hand corner of blocks). The coupler power density can be calculated by  $Q_{\text{gap}}/V_{\text{coupler}}$ . The air gap power  $Q_{\text{gap}}$  and the coupler volume  $V_{\text{coupler}}$  are limited by the material's physical characteristics

(physical limits, i.e., saturation flux density, electric field strength, etc.) and the gap geometry requirements (geometry limits, i.e., gap distance  $d$  and transmitter/receiver area  $A_c$ ). In Sections III-A and III-B, it was calculated that IPT has  $\sim 400\times$  greater air gap energy storage capability than CPT under normal atmospheric conditions (air). Conversely, Section III-C demonstrated that the coupler to gap volume ratio favors CPT with a value of  $V_{\text{coupler}}/V_{\text{gap}} = 1.68$  compared to the IPT best case scenario of  $\sim 100$  and typical value of  $\sim 500$ . This constitutes up to a  $\sim 300\times$  coupler to gap volume ratio advantage for CPT over IPT in small gap applications. The overall power density of these systems is reflected by the product of air gap power density and volume ratio as plotted in Fig. 2.12. Ultimately, Fig. 2.12 indicates that, despite disparate gap energy and coupler volumetric characteristics, IPT and CPT are roughly equivalent in power density for small gap applications. Another observation is that the coupler power density is much closer to the gap power density for the CPT technique. According to the analysis flow chart in Fig. 2.14, the following plots in Figs. 2.15 and 2.16 can be drawn to compare the suitable applications for IPT and CPT. In addition, theoretical limits are plotted against the surveyed data presented earlier in Section II. The analytical and surveyed data plotted together provide a level of verification of the analytical modeling. Limitation inputs for the model are

$$E_{\text{max}} := 3 \frac{\text{MV}}{\text{m}};$$

$$J_{\text{max}} := 5 \frac{\text{A}}{\text{mm}^2};$$

$$B_{\text{max}} := 0.2\text{T};$$

$$d_{\min} := 0.025\text{mm};$$

$$k_w := 0.2;$$

$$f_{\text{sw}} := 1\text{MHz}$$

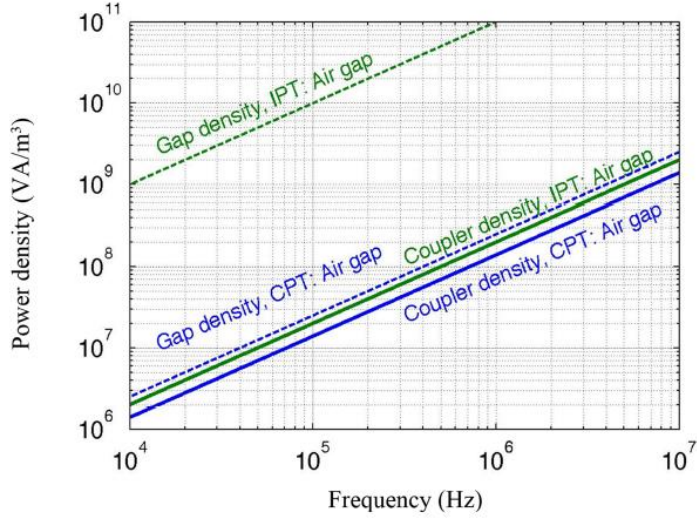


FIGURE 25 COUPLER POWER DENSITY AND GAP POWER DENSITY [1].

When  $d = 1\text{mm}$ ,  $A_c = 10\text{ cm} \times 10\text{ cm}$ , capacitive coupler  $V_{\text{coupler}}/V_{\text{gap}} \approx 1.68$ , inductive coupler  $V_{\text{coupler}}/V_{\text{gap}} \approx 500$ .

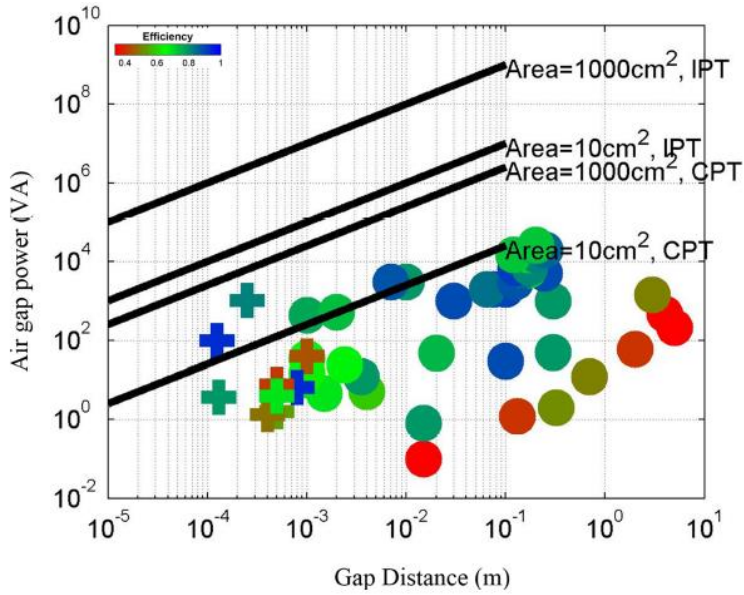


FIGURE 26 AIR GAP POWER VERSUS GAP DISTANCE [1].

Frequency: 1 MHz Lines: Analytical data. Scatter points: Survey data.

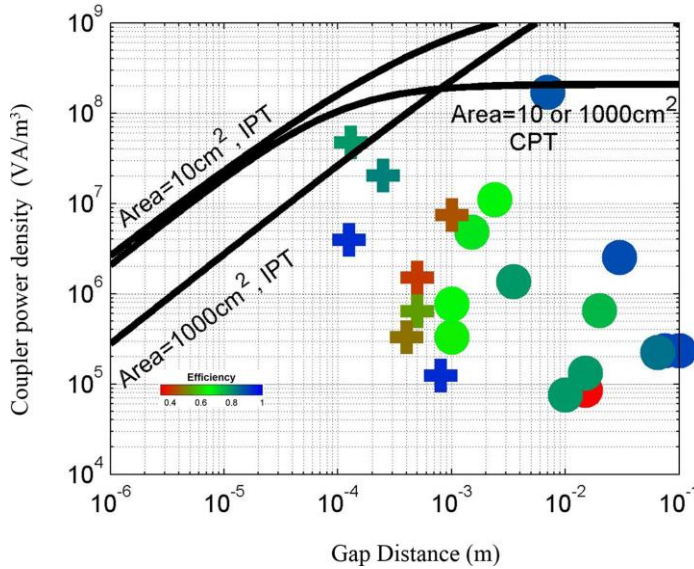


FIGURE 27 COUPLER POWER DENSITY VERSUS AIR GAP DISTANCE [1].

Figure 2.17 plots air gap power versus distance with efficiency indicated by color. Frequency: 1 MHz Lines: Analytical data. Scatter points: Survey data. In applications where the gap distance is fixed, and the coupler size is not a concern, IPT has the advantage of overall higher power capability. In applications where space is a commodity, CPT may have the advantage because of the lower coupler to gap volume ratio. Clearly, for a fixed gap, both IPT and CPT exhibit the property that larger area allows higher coupler power as shown in Fig. 2.13. Fig. 2.14 plots coupler power density versus gap distance with efficiency indicated by color. In applications where the coupler volume is fixed (rather than the gap), coupler power density  $Q_{\text{gap}}/V_{\text{coupler}}$  is of greater concern. For small gaps ( $<1$  mm), CPT has a higher power density. When the gap is  $\sim 1$  mm, CPT and IPT have similar power densities. For gaps  $>1$  mm, IPT has a better power density. This provides additional support to the notion that the boundary between IPT and CPT's efficacy with respect to gap size occurs at  $\sim 1$ -mm gap, for a given coupling area.

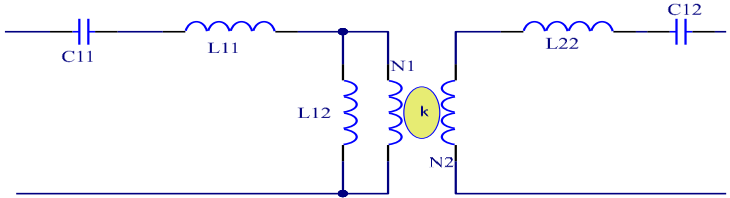
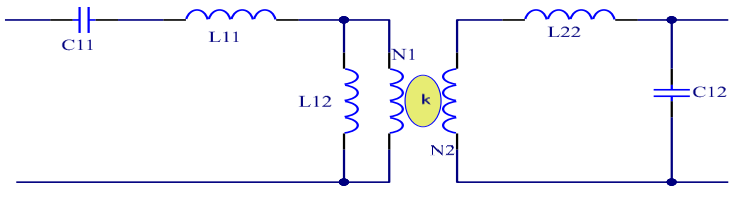
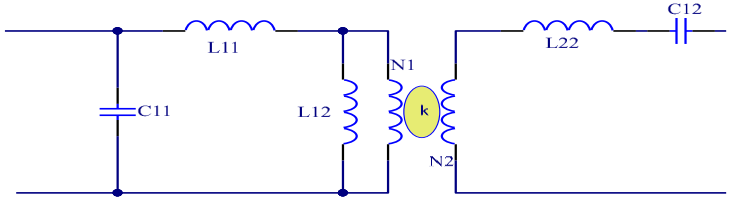
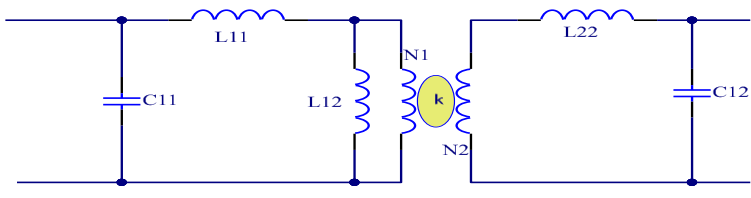
## Chapter 3. TRADITIONAL VS WIRELESS POWER TRANSFER

### 3.1 INTRODUCTION

In the previous section we examined two types of Wireless Power Transfer, WPT. We compared CPT to IPT with both having a maximum distance between them of 1mm. While this is still be considered wireless its application and many of the calculations are based on the conventional transformer design. In this project we are looking to wirelessly transfer power over 21cm, in previous sections we determined that for direct high efficiency energy transfer under a wavelength in distance leads us to look at IPT as the means of power transfer. We will examine the switching configuration of each as well as the resonant sections. There are several topologies available for use in WPT. Table 3.1 shows a summary of the basic topologies and typical acronym used for each.

The analysis and design of these topologies have been studied thoroughly for traditional power transfer. When looking at WPT another layer of complexity is added in the form of coupling between the primary and secondary as well as both being required to have matching resonant circuits. Starting with the traditional transformer design approach the simple three topologies becoming four topologies: (SS), (SP), (PS), and (PP) (first letter denotes primary and second a secondary compensation). The major goal is to evaluate the performance of the converter with wide input range and decide which approach best meets the needs of our application. We will examine the merits of each, first with the traditional transformer model and then comparing to the WPT model. In this section we will first examine resonant mode conversion and then compare the various topologies to determine which will best suits our needs for WPT.

TABLE 3-1 SUMMARY OF RESONANT TOPOLOGIES TO BE INVESTIGATED

Simplified Circuits of various resonant mode converters	Abbreviation
<p style="text-align: center;">Series-Series</p> 	Series-Series SS
<p style="text-align: center;">Series-Parallel</p> 	Series-Parallel SP
<p style="text-align: center;">Parallel-Series</p> 	Parallel-Series PS
<p style="text-align: center;">Parallel-Parallel</p> 	Parallel-Parallel PP

The analysis and design of these topologies have been studied thoroughly. In next section, three topologies will be evaluated for front end DC/DC application. When looking at WPT another layer of complexity is added in the form of the secondary, which must also have a Resonant Circuit. This leads to the simple three topologies becoming four topologies: (SS), (SP), (PS), and (PP) (first letter denotes primary and second a secondary compensation). The major goal is to evaluate the performance of the converter with wide input range and



decide which approach best meets the needs of our application. We will examine the merits of each, first with the simple transformer model and then comparing to the WPT model. In this section we will first examine resonant mode conversion and then compare the various topologies to determine which will best suits our needs for WPT.

### 3.2 RESONANT POWER CONVERTERS

Resonant power converters contain resonant L–C networks, also called resonant circuit (RC) or resonant tank network, whose voltage and current waveforms vary sinusoidally during one or more subintervals of each switching period. These converters contain low total harmonic distortion because switching frequency is equal to first harmonic frequency. In non-resonant power converters the resonant frequency of the primary inductance as well as parasitic inductance and capacitance may be 10 times the switching frequency and therefore each time the switching is closed the circuit resonates at a frequency much higher than that of the total switching period. This higher frequency oscillation stores energy in the oscillation and must be mitigated by means of snubbers and filtering to reduce the effects of the Electro Magnetic Interference, or EMI, produced back out onto the source or the load. Basic power converter topologies being considered for WPT systems are presented in Table 3.1. The full-bridge (Figure 3.1) inverter, composed of four switches and an RC, is commonly used in high power applications. The half-bridge inverter (Figure 3.3) has only two switches and two others can be replaced by capacitors. The output voltage  $v_1$  of the full bridge converter is doubled when compared with that of half-bridge topology.

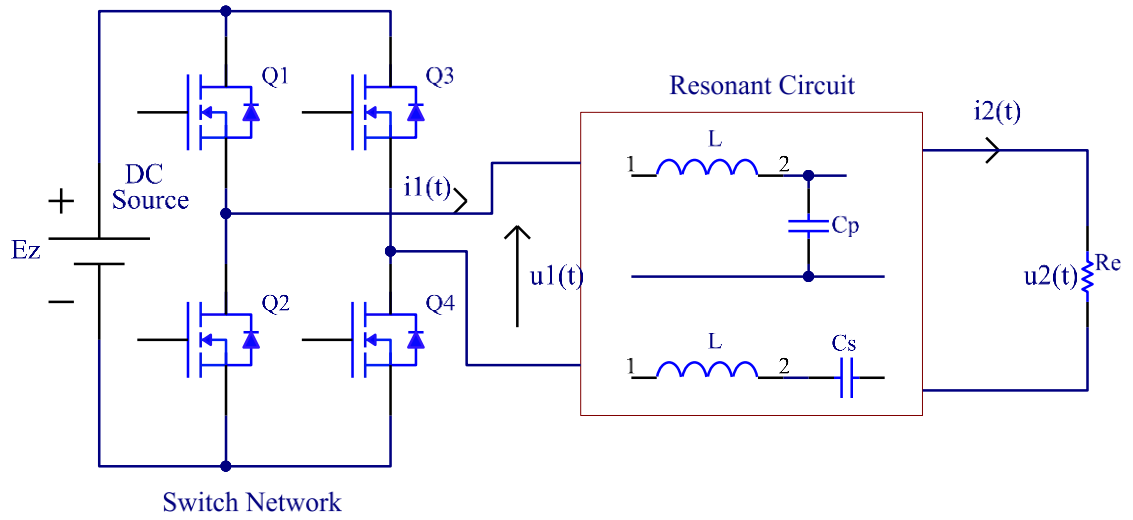


FIGURE 28 SIMPLIFIED SCHEMATIC DIAGRAM OF FULL BRIDGE CONVERTER

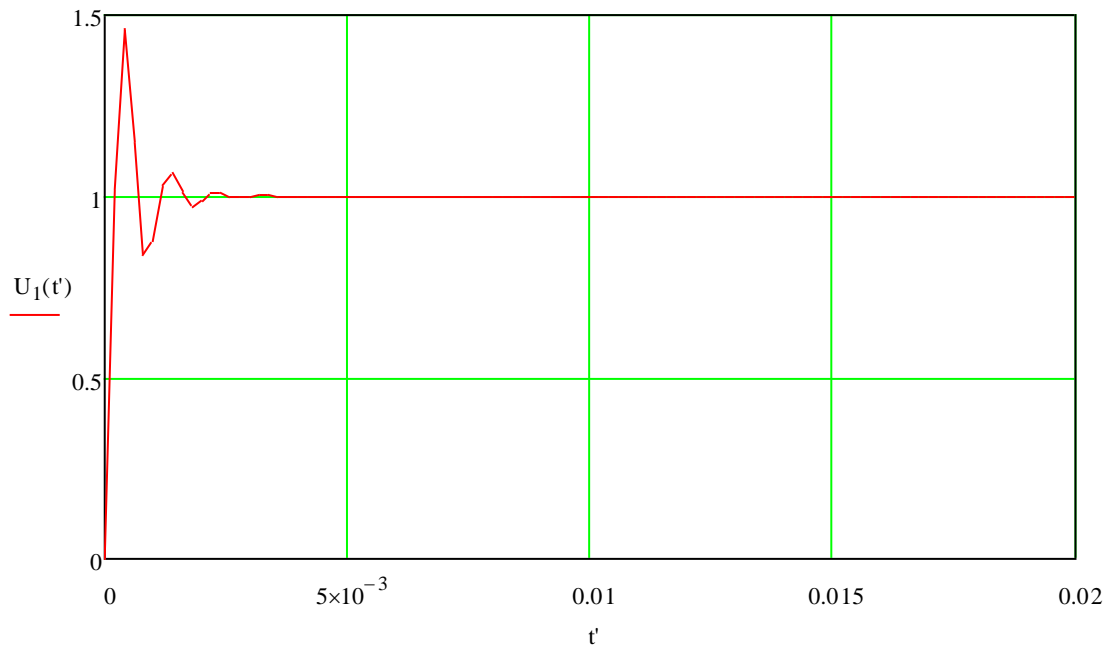


FIGURE 29 TYPICAL STEP RESPONSE OF UN DAMPENED PRIMARY WAVEFORM

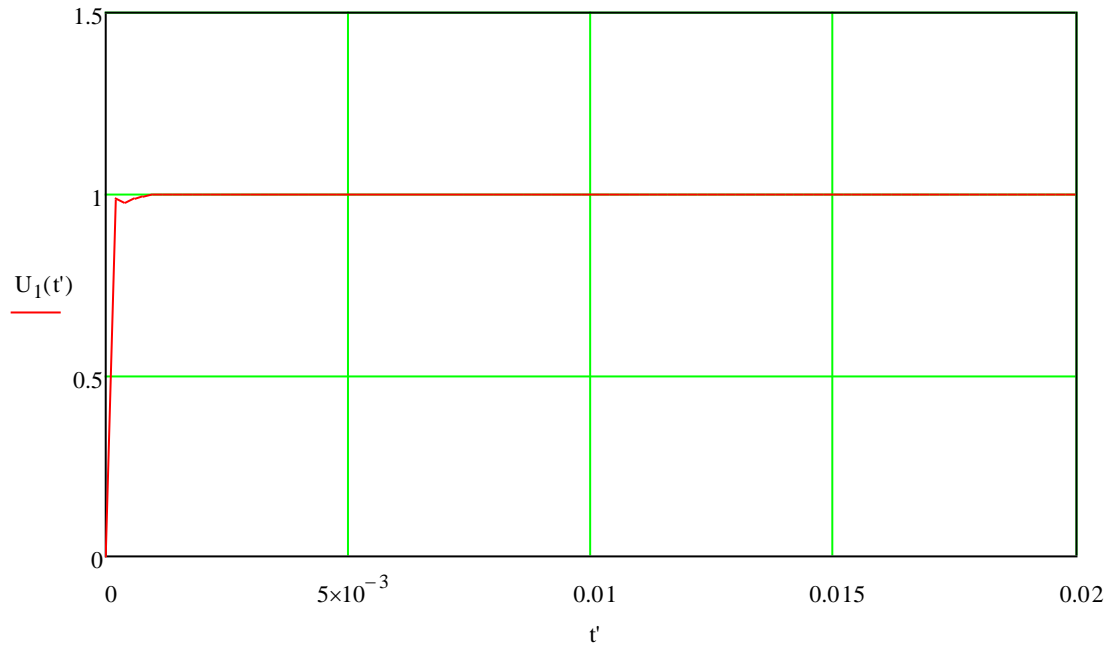


FIGURE 30 TYPICAL STEP RESPONSE OF CRITICALLY DAMPENED PRIMARY WAVEFORM

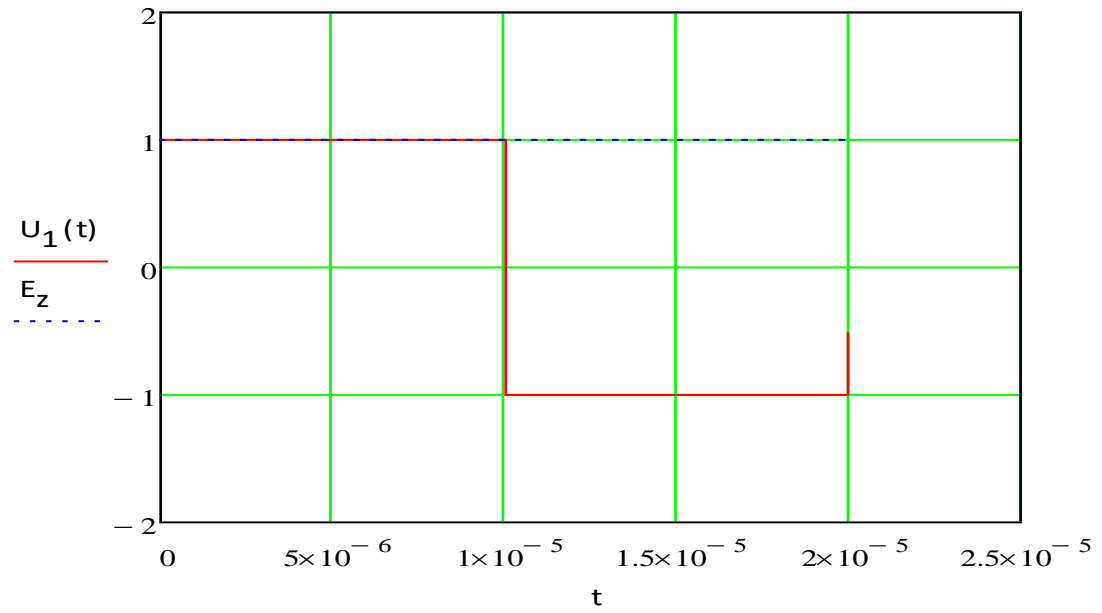


FIGURE 31 GRAPH OF TYPICAL WAVEFORMS FOR FULL BRIDGE CONVERTER

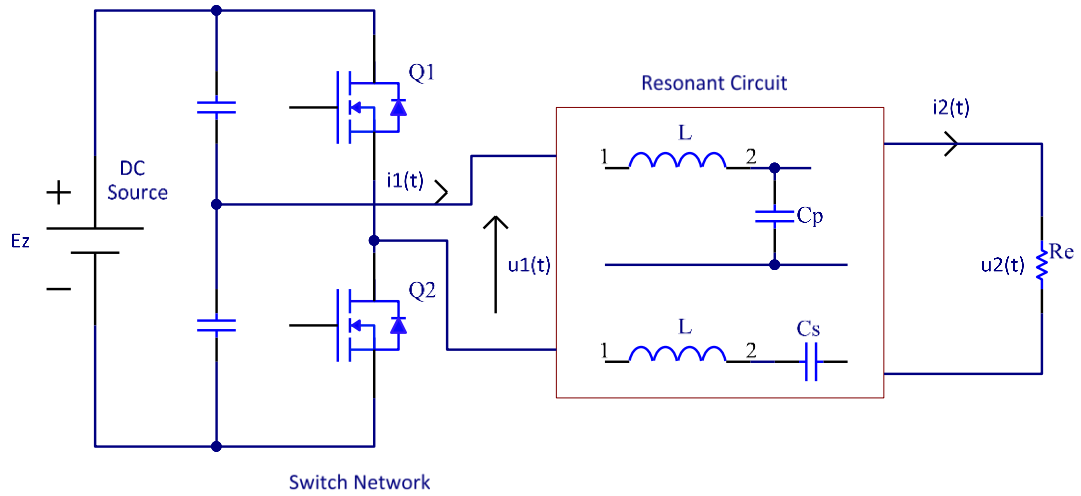


FIGURE 32 HALF BRIDGE BIPOLAR CONVERTER

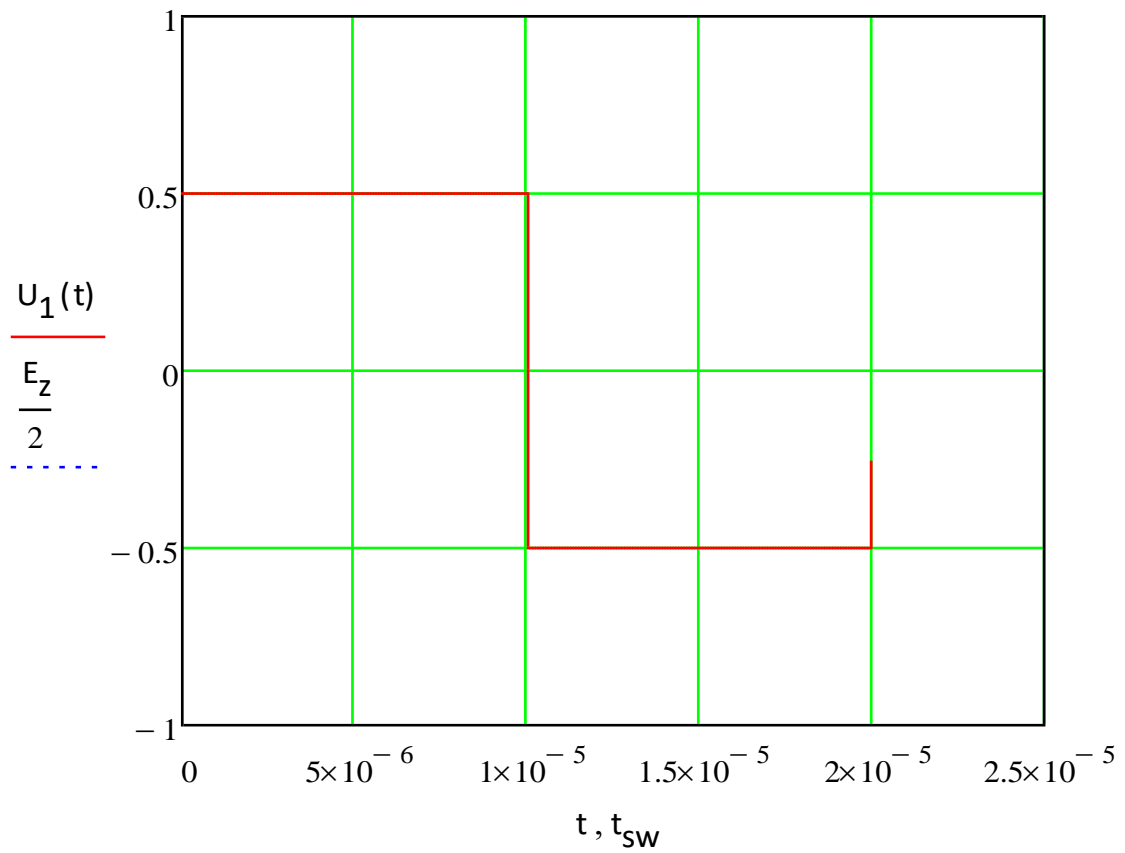


FIGURE 33 GRAPH OF TYPICAL HALF BRIDGE BIPOLAR CONVERTER WAVEFORMS

In conventional applications, a transformer is used for galvanic insulation between source and load, and its operation is based on high magnetic coupling factor  $k$  between primary and secondary windings. The coupling factor or coupling coefficient “ $k$ ” is the percentage of magnetic of the lines of flux from the first coil that are cutting the second coil. Generally, the amount of inductive coupling that exists between the two coils is expressed as a fractional number between 0 and 1 instead of a percentage (%) value, where 0 indicates zero or no inductive coupling, and 1 indicating full or maximum inductive coupling. In other words, if  $k = 1$  the two coils are perfectly coupled, if  $k > 0.5$  the two coils are said to be tightly coupled and if  $k < 0.5$  the two coils are said to be loosely coupled.

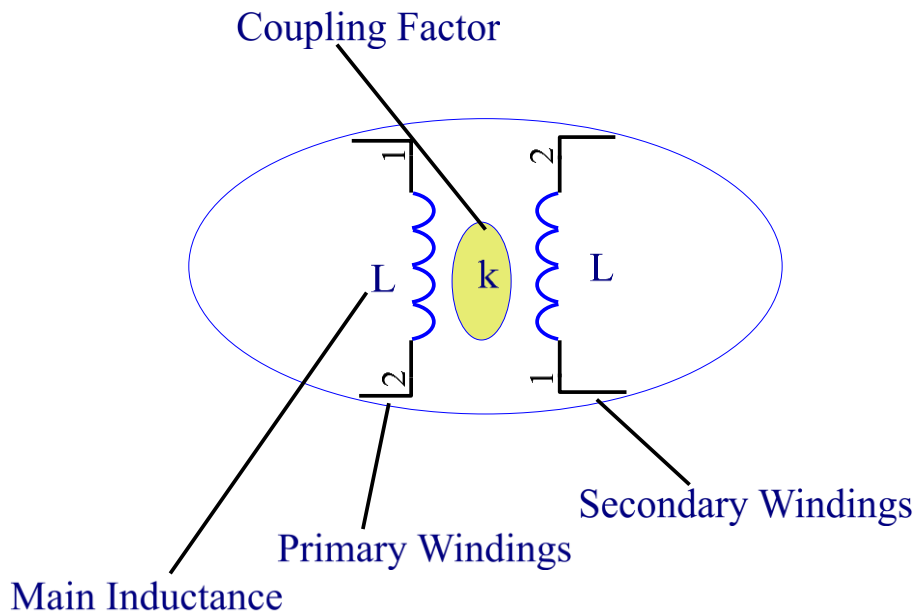


FIGURE 34 FUNCTIONAL SCHEMATIC DIAGRAM OF RESONANT TRANSFORMER WITH COUPLING FACTOR

Consequently, increase in magnetizing current causes higher conducting losses. Also, winding losses increase because of large leakage inductances. Another disadvantage of transformers with relatively large gap is electromagnetic compatibility (EMC) problem

(strong radiation). To minimize the above disadvantages of WPT transformers, several power conversion topologies have been proposed, which can be classified into the following categories: the flyback, resonant, quasi-resonant, and self-resonant. The common thing for all these topologies is that they all utilize the energy stored in the transformer. In most applications, a resonant soft switching technique is used because it allows both compensation of the transformer leakage inductance and reduction of power converter switching losses [25]. To form resonant circuits and compensate for the large WPT transformer leakage inductances, two methods can be applied *S*-series or *P*-parallel. In conventional resonant topologies, Series Resonant Converter (SRC), Parallel Resonant Converter (PRC) and Series Parallel Resonant Converter (SPRC, also called LCC resonant converter) are the three most popular topologies.

### 3.2.1 TRADITIONAL SERIES RESONANT CONVERTER

The circuit diagram of a half bridge Series Resonant Converter is shown in Figure 3.6. The DC characteristic of SRC is shown in Figure 3.7. The resonant inductor  $L_{11}$  and resonant capacitor  $C_{11}$  are in series. They form a series resonant tank. The resonant tank will then in series with the load. From this configuration, the resonant tank and the load act as a voltage divider. By changing the frequency of input voltage  $V_{in}$ , the impedance of resonant tank will change. This impedance will divide the input voltage with load. Since it is a voltage divider, the DC gain of SRC is always lower than 1. At resonant frequency, the impedance of series resonant tank will be very small; all the input voltage will drop on the load. So for series resonant converter, the maximum gain happens at resonant frequency[23].

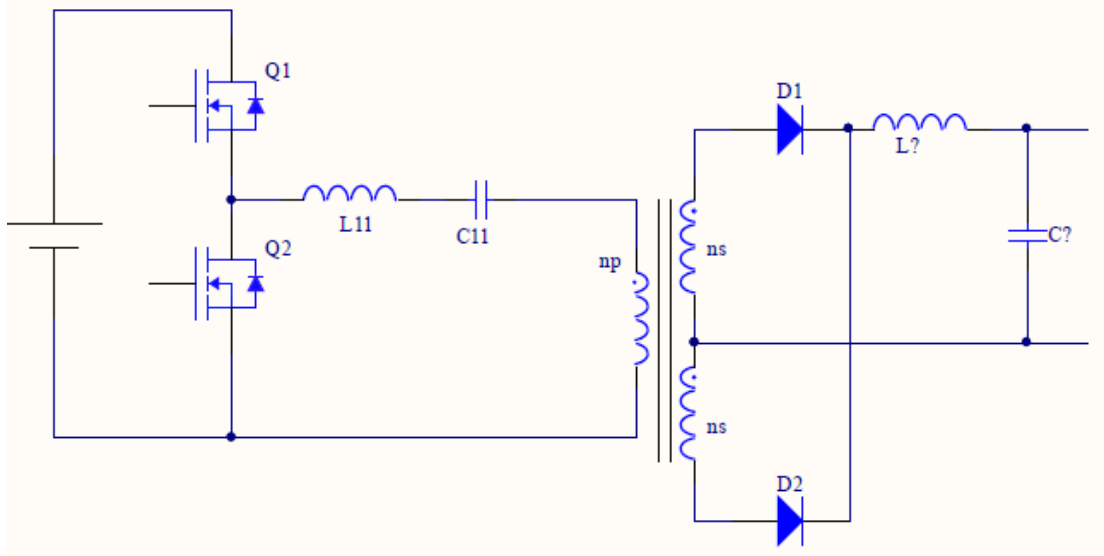


FIGURE 35 SIMPLIFIED SCHEMATIC OF HALF BRIDGE SERIES RESONANT CONVERTER

For front end DC/DC application, a SRC is designed to meet the specifications with following parameters:

Transformer turns ratio: 5:2,

Resonant inductance:  $37\mu\text{H}$ ,

Resonant capacitance:  $17\text{nF}$ .

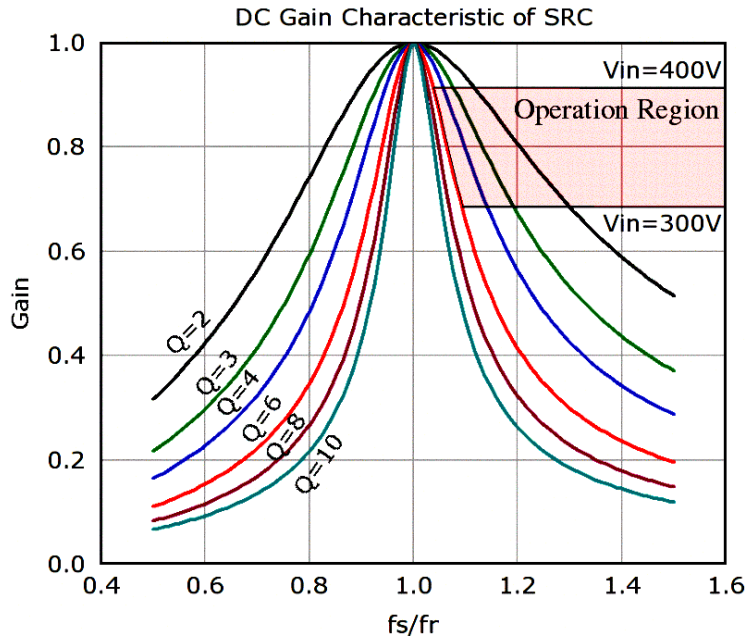


FIGURE 36 REFERENCE DIAGRAM OF DC OPERATING REGION OF SERIES RESONANT CONVERTER [26].

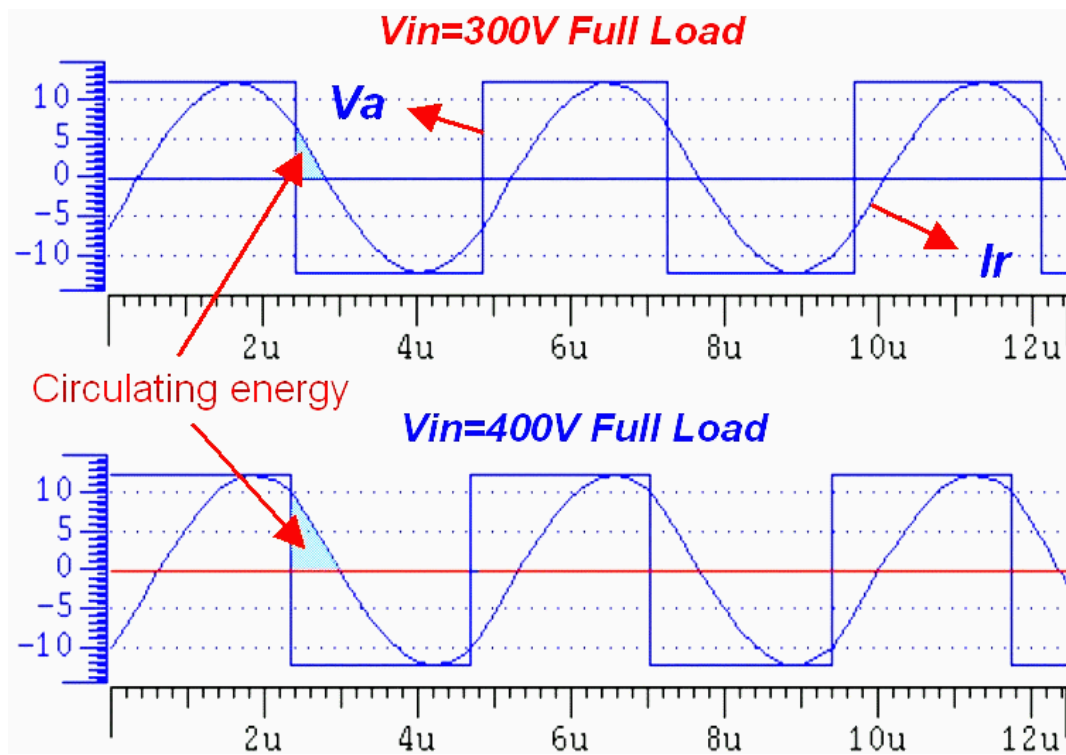


FIGURE 37 REFERENCE DIAGRAM OF TYPICAL WAVEFORMS OF SERIES RESONANT CONVERTER [26].



With above parameters, the range of  $Q$  is from 6 (Full load) to 0 (No load). With above design, the operating region of the converter is shown in Figure 27 as shaded area.

Simulation waveforms of SRC; Note the Circulating Energy at 300V is significantly less than at 400V Simulation waveform is shown in Figure 28. From the operating region graph and simulation waveforms, several things could be observed: Operating region is on the right side of resonant frequency  $f_r$ . This is because of zero voltage switching (ZVS) is preferred for this converter. When switching frequency is lower than resonant frequency, the converter will work under zero current switching (ZCS) condition. In fact, the rule is when the DC gain slope is negative; the converter is working under zero voltage switching condition. When the DC gain slope is positive, the converter will work under zero current switching condition. For power MOSFET, zero voltage switching is preferred. It can be seen from the operating region that at light load, the switching frequency needs to increase to very high to keep output voltage regulated. This is a big problem for SRC. To regulate the output voltage at light load, some other control method has to be added. At 300V input, the converter is working close to resonant frequency. As the input voltage increases, the converter is working at a higher frequency away from resonant frequency. As frequency increases, the impedance of the resonant tank is increased. This means more and more energy is circulating in the resonant tank instead of transferred to output.

From the simulation waveforms, at 300V input, the circulating energy is much smaller than 400V input situation. Here the circulating energy is defined as the energy sent back to the input source in each switching cycle. The more energy is sent back to the source during each switching cycle, the higher the energy needs to be processed through the semiconductors, the higher the conduction loss. Also from the MOSFET current we can

see that the turn off current is much smaller in 300V input. When input voltage increases to 400V, the turn off current is more than 10A, which is around the same level as PWM converter.

With above analysis, we can see that SRC is not a good candidate for front end DC/DC converter. The major problems are: light load regulation, high circulating energy and turn off current at high input voltage condition.

### 3.2.2 TRADITIONAL PARALLEL RESONANT CONVERTER

The Simplified Schematic of parallel resonant converter is shown in Figure 3.9. Its DC characteristic is shown in Figure 33. For parallel resonant converter, the resonant tank is still in series. It is called parallel resonant converter because in this case the load is in parallel with the resonant capacitor. More accurately, this converter should be called series resonant converter with parallel load. Since the transformer primary side is a capacitor, an inductor is added on the secondary side to match the impedance.

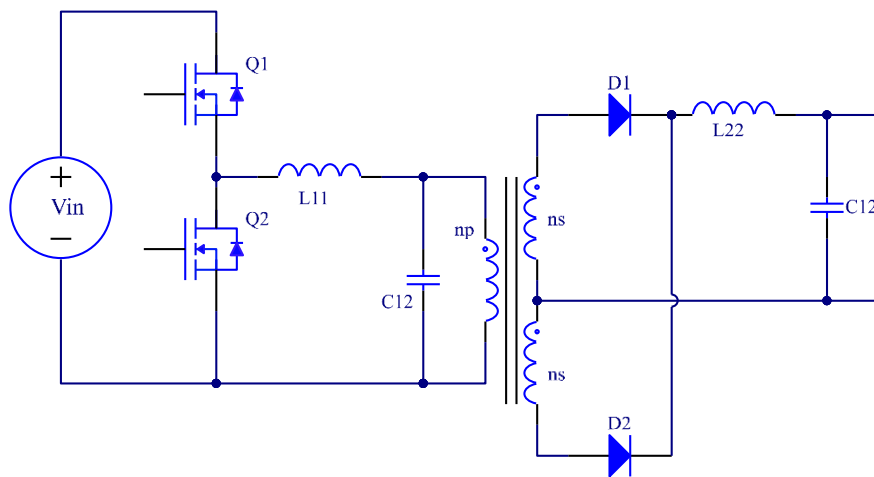


FIGURE 38 SIMPLIFIED SCHEMATIC OF HALF BRIDGE PARALLEL RESONANT CONVERTER

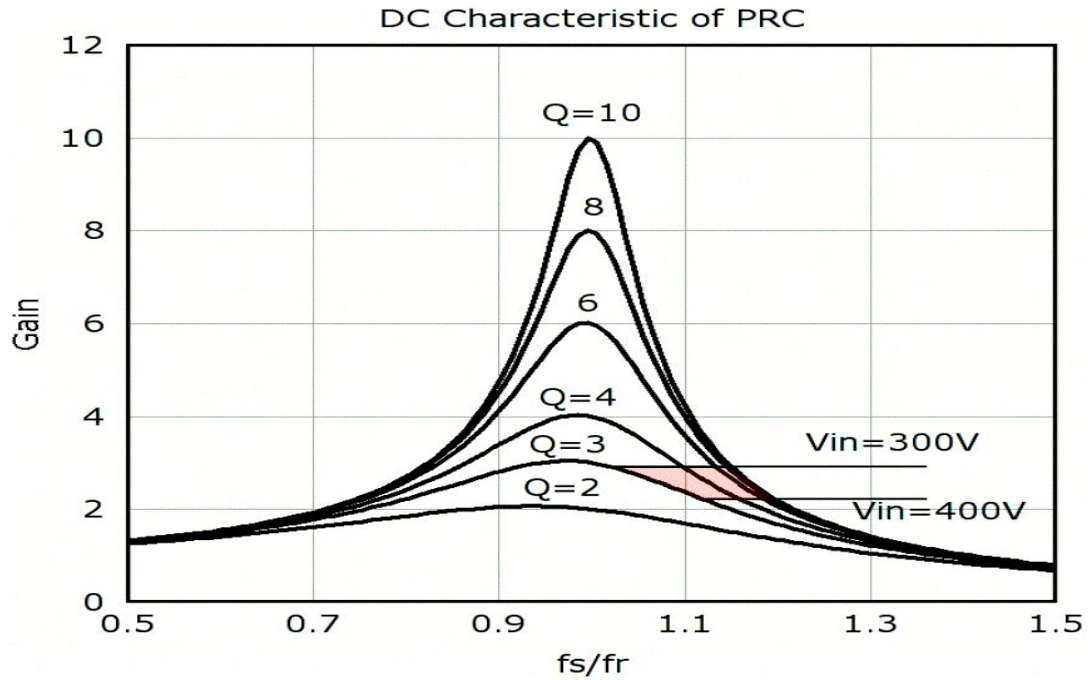


FIGURE 39 REFERENCE DIAGRAM OF OPERATING REGION OF PARALLEL RESONANT CONVERTER [26]

The parameters of parallel resonant converter designed for front end DC/DC application are:

Transformer turns ratio: 9:1,

Resonant inductance:  $58\mu H$ ,

Resonant capacitance:  $11.7nF$ .

With above parameters, the range of  $Q$  for this converter is 3 (Full load) to  $\infty$  (No load).

The operating region of PRC is shown in Figure 33 as shaded area. Simulation waveform is shown in Figure 4.6. From the operating region graph and simulation waveforms, several things could be observed:

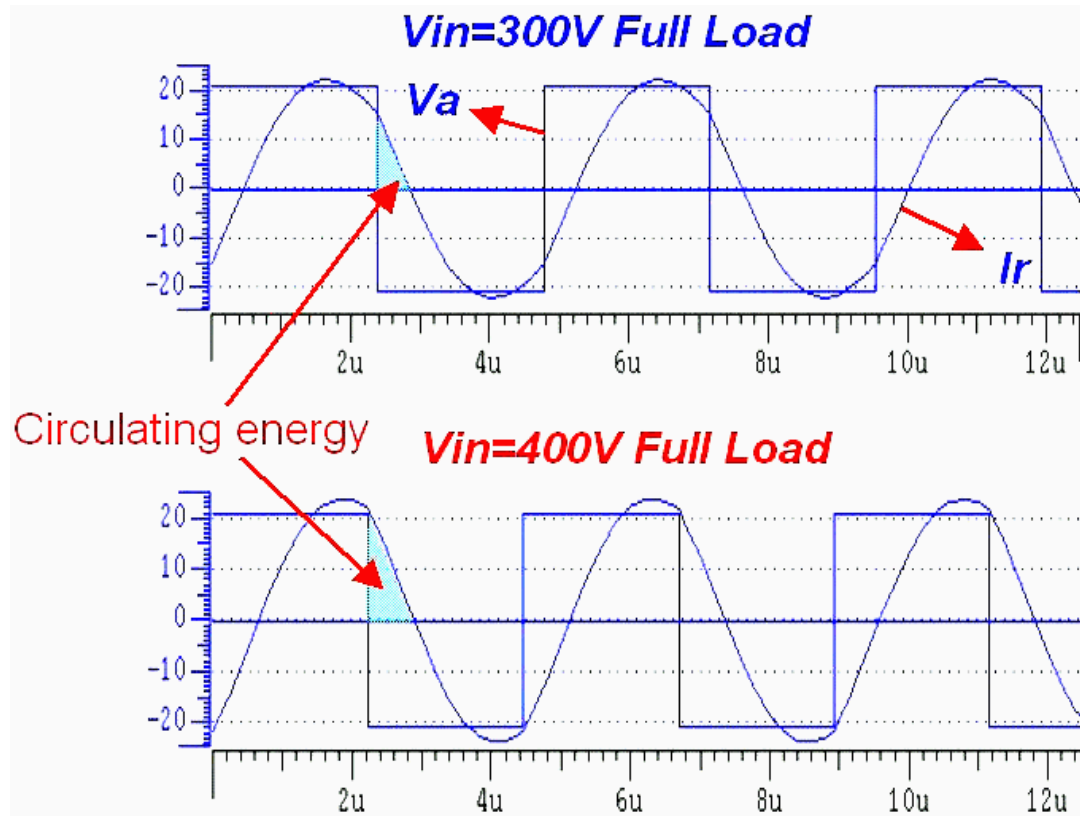


FIGURE 40 REFERENCE DIAGRAM OF GRAPH INDICATING DC SIMULATION WAVEFORMS OF PARALLEL RESONANT CONVERTER [26]

Similar to Series Resonant Converter, the operating region is also designed on the right hand side of resonant frequency to achieve Zero Voltage Switching. Compare with SRC, the operating region is much smaller. At light load, the frequency doesn't need to change too much to keep output voltage regulated. So light load regulation problem doesn't exist in PRC. Same as SRC for PRC, the converter is working close to resonant frequency at 300V. At high input voltage, the converter is working at a higher frequency far away from the resonant frequency. From simulation waveforms, at 300V input, the circulating energy is smaller than 400V input situation. Compare with SRC, it can be seen that for PRC, the circulating energy is much larger. Also from the MOSFET current we can see that the turn

off current is much smaller in 300V input. When the input voltage increases to 400V, the turn off current is more than 15A, which is even higher than the PWM converter. For PRC, a big problem is the circulating energy is very high even at light load. For PRC, since the load is in parallel with the resonant capacitor, even at no load condition, the input will still see a pretty small impedance due to the series resonant tank. This will induce pretty high circulating energy even when the load is zero. With above analysis, we can see that PRC is not a good candidate for front end DC/DC converter too. The major problems are: high circulating energy, high turn off current at high input voltage condition.

### 3.2.3 TRADITIONAL SERIES PARALLEL RESONANT CONVERTER

The Simplified Schematic of series parallel resonant converter is shown in Figure 3.14. The DC characteristic of SPRC is shown in Figure 3.15. Its resonant tank consists of three resonant components:  $L_{11}$ ,  $C_{11}$  and  $C_{12}$ . The resonant tank of SPRC can be looked as the combination of SRC and PRC. Similar as PRC, an output filter inductor is added on secondary side to match the impedance. For SPRC, it combines the good characteristic of PRC and SRC. With load in series with series tank  $L_{11}$  and  $C_{11}$ , the circulating energy is smaller compared with PRC. With the parallel capacitor  $C_{12}$ , SPRC can regulate the output voltage at no load condition. The parameters of SPRC designed for front end DC/DC application are:

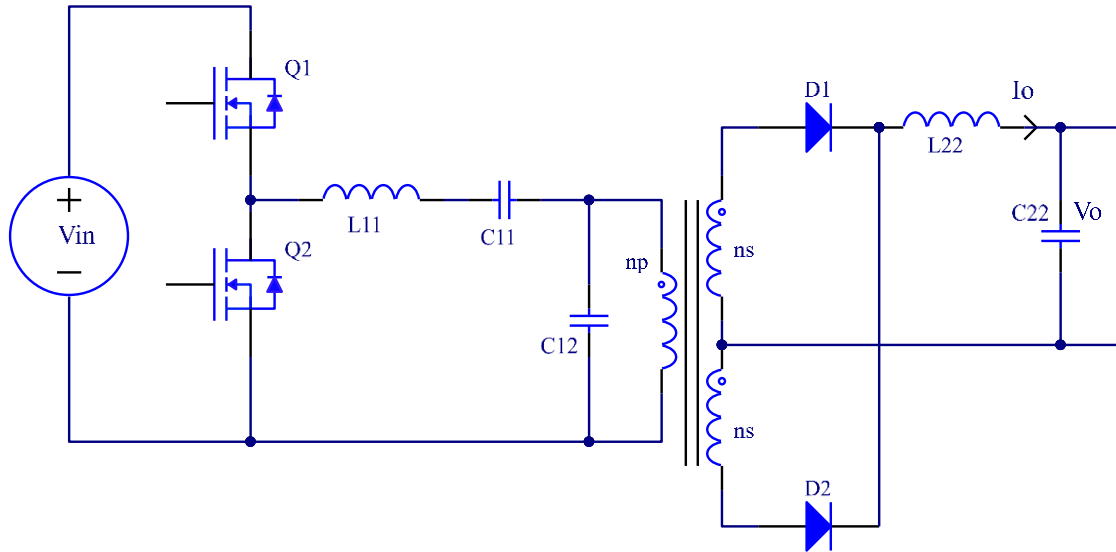


FIGURE 41 SIMPLIFIED SCHEMATIC OF HALF BRIDGE SERIES PARALLEL RESONANT CONVERTER

Transformer turns ratio: 6:1,

Resonant inductance:  $72\mu\text{H}$ ,

Series resonant capacitor  $C_{11}$ :  $17.7\text{nF}$ ,

Parallel resonant capacitor  $C_{12}$ :  $17.7\text{nF}$ ,

Range of  $Q$ : 1 (Full load) to  $\infty$  (No load)

The DC characteristic and operating region of SPRC are shown in Figure 3.13. Simulation waveform is shown in Figure 3.14. From the operating region graph, several things could be observed:

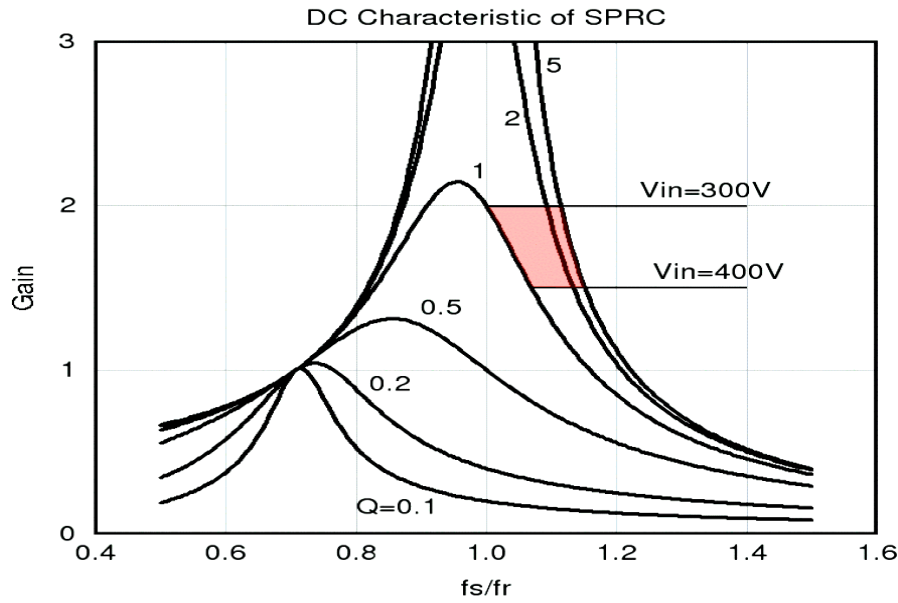


FIGURE 42 REFERENCE DIAGRAM OF OPERATING REGION OF SERIES PARALLEL RESONANT CONVERTER [26]

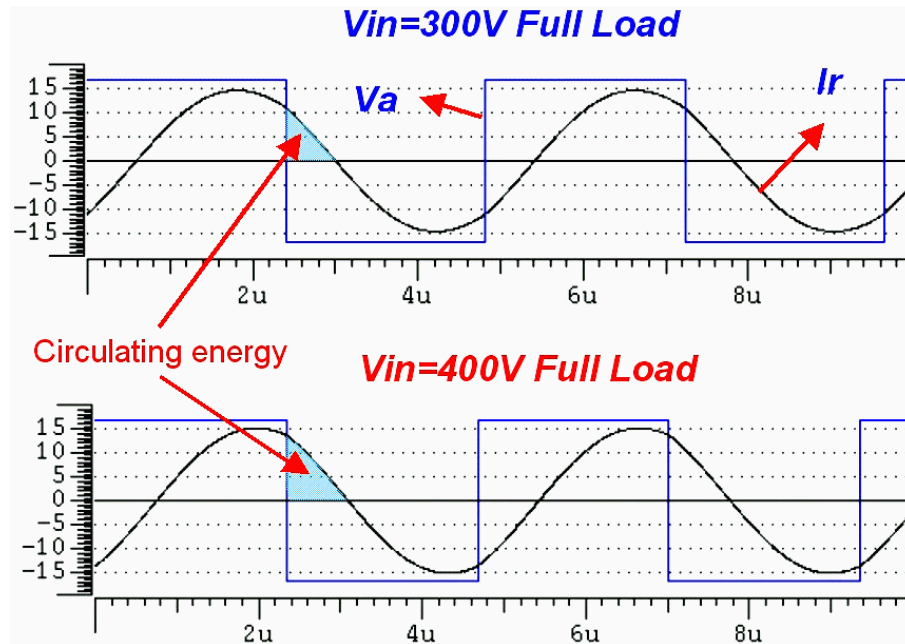


FIGURE 43 REFERENCE OF SIMULATED WAVEFORMS OF SERIES PARALLEL RESONANT CONVERTER [26, 27]

Similar to SRC and PRC, the operating region is also designed on the right hand side of resonant frequency to achieve Zero Voltage Switching. From the operating region graph,

it can be seen that SPRC narrow switching frequency range with load change compare with SRC. Compare the switching waveforms, the input current in much smaller than PRC and a little larger than SRC. This means for SPRC, the circulating energy is reduced compare with PRC. Same as SRC and PRC, the converter is working close to resonant frequency at 300V. At high input voltage, the converter is working at higher frequency far away from resonant frequency. Same as PRC and SRC, the circulating energy and turn off current of MOSFET also increase at high input voltage. The turn off current is more than 10A. With above analysis, we can see that SPRC combines the good characteristics of SRC and PRC. Smaller circulating energy and not so sensitive to load change. Unfortunately, SPRC still will see big penalty with wide input range design. With wide input range, the conduction loss and switching loss will increase at high input voltage. The switching loss is similar to that of PWM converter at high input voltage. By analysis, design and simulation of SRC, PRC and SPRC, the conclusion is that these three converters all cannot be optimized at high input voltage. High conduction loss and switching loss will be resulted from wide input range. To achieve high switching frequency and higher efficiency, we have to look for some other topologies.

#### 3.2.4 LLC RESONANT CONVERTER

Three traditional resonant topologies were analyzed in previous sections. From the results, we can see that all of them will see big penalty for wide input range design. High circulating energy and high switching loss will occur at high input voltage. They are not suitable for front end DC/DC application. Although above analysis gave us negative results, still we could learn something from it:



For a resonant tank, working at its resonant frequency is the most efficient way of transferring energy as all energy from the inductor is transferred to the capacitor with the only losses being that  $I^2R$  losses. This rule applies to SRC and PRC very well. As for the SPRC, it has two resonant frequencies. Normally, working at its highest resonant frequency will be more efficient. To achieve zero voltage switching, the converter has to work on the negative slope of DC characteristic. From above analysis, LCC resonant converter also could not be optimized for high input voltage. The reason is the same for SRC and PRC; the converter will work at switching frequency far away from resonant frequency at high input voltage. Look at the DC characteristic of LCC resonant converter, it can be seen that there are two resonant frequencies. One low resonant frequency determined by series resonant tank  $L_{11}$  and  $C_{11}$ . One high resonant frequency determined by  $L_{11}$  and equivalent capacitance of  $C_{11}$  and  $C_{12}$  in series. For a resonant converter, it is normally true that the converter could reach high efficiency at resonant frequency. For LCC resonant converter, although it has two resonant frequencies, unfortunately, the lower resonant frequency is in ZCS region. For this application, we are not able to design the converter working at this resonant frequency. Although the lower frequency resonant frequency is not usable, the idea is how to get a resonant frequency at ZVS region. By changing the LCC resonant tank to its dual resonant network, this is achievable. As shown in Figure 3.15, by change L to C and C to L, a LLC resonant converter could be built. The DC characteristics of these two converters are shown in Figure 3.16 and Figure 3.17. The DC characteristic of LLC converter is like a flip of DC characteristic of LCC resonant converter. There are still two resonant frequencies. In this case,  $L_{11}$  and  $C_{11}$  determine the higher resonant frequency.

The lower resonant frequency is determined by the series inductance of  $L_{12}$  and  $L_{11}$ . Now the higher resonant frequency is in the ZVS region, which means that the converter could be designed to operate around this frequency.

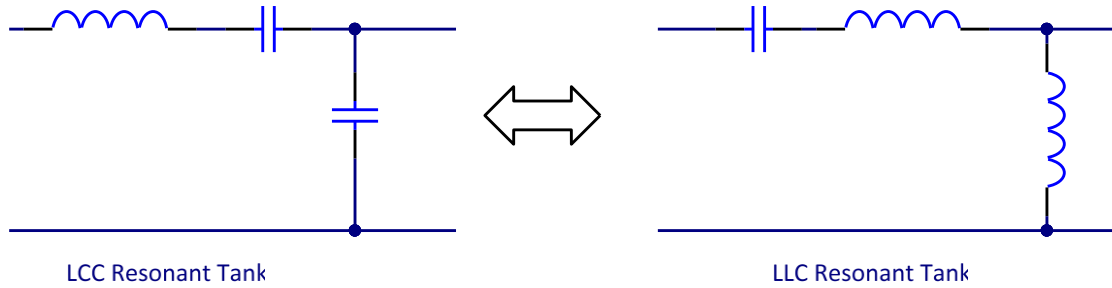


FIGURE 44 SIMPLIFIED SCHEMATIC OF LCC AND LLC RESONANT TANK CIRCUITS

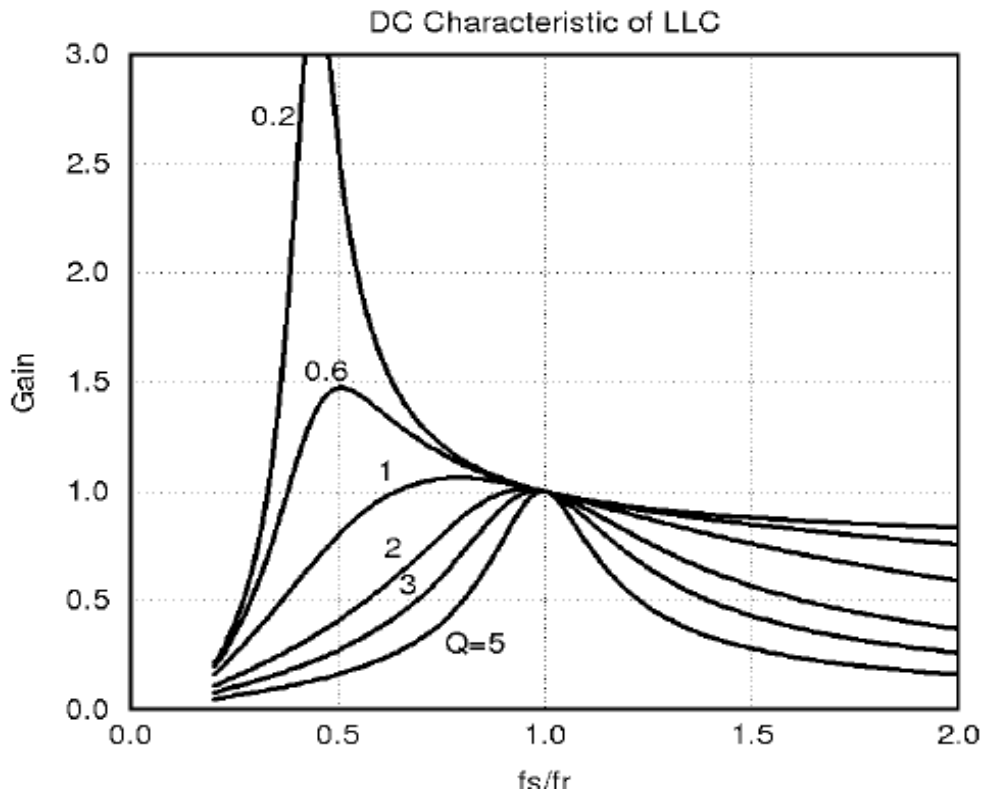


FIGURE 45 REFERENCE DIAGRAM OF DC CHARACTERISTIC OF LLC RESONANT CONVERTER [26, 27]

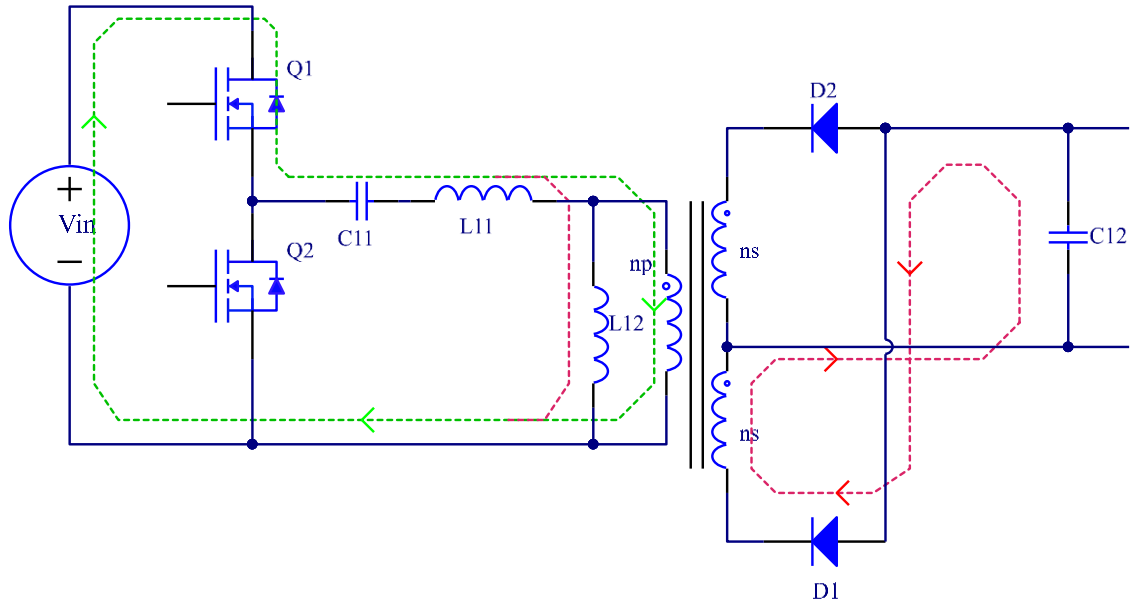


FIGURE 46 SIMPLIFIED SCHEMATIC OF HALF BRIDGE LLC RESONANT CONVERTER

As a matter of fact, LLC resonant converter existed for very long time. But because of lack of understanding of characteristic of this converter, it was used as a series resonant converter with passive load. Which means it was designed to operate in switching frequency higher than resonant frequency of the series resonant tank of  $L_{11}$  and  $C_{11}$ . When operating in this region, LLC resonant converter acts very similar to SRC. The benefit of LLC resonant converter is narrow switching frequency range with light load and ZVS capability with even no load. In this dissertation, some unexplored operating region of LLC resonant converter will be investigated. Within these operating regions, LLC resonant converter will have some very special characteristic, which makes it an excellent candidate for front end DC/DC application.

To design LLC resonant converter, DC analysis is essential. Two methods were discussed: fundamental simplification method and simulation method.

The DC characteristic of LLC resonant converter could be divided into ZVS region and ZCS region as shown in Figure 3.19. For this converter, there are two resonant frequencies.

One is determined by the resonant components  $L_{11}$  and  $C_{11}$ . The other one is determined by  $L_{12}$ ,  $C_{11}$  and load condition. As load getting heavier, the resonant frequency will shift to higher frequency. The two resonant frequencies are [23]:

#### NO LOAD RESONANT FREQUENCY

$$f_{r1} = \frac{1}{2\pi \cdot \sqrt{L_{11} \cdot C_{11}}} \quad (3-1)$$

#### LOADED RESONANT FREQUENCY

$$f_{r2} = \frac{1}{2\pi \cdot \sqrt{(L_{12} + L_{11}) \cdot C_{11}}} \quad (3-2)$$

With this characteristic, for 400V operation, it could be placed at the resonant frequency of  $f_{r1}$ , which is a resonant frequency of series resonant tank of  $C_{11}$  and  $L_{11}$ . While input voltage drops, more gain can be achieved with lower switching frequency. With proper choose of resonant tank, the converter could operate within ZVS region for load and line variation. There are some interesting aspects of this DC characteristic. On the right side of  $f_{r1}$ , this converter has same characteristic of SRC. On the left side of  $f_{r1}$ , the image of PRC and SRC are fighting to be the dominant. At heavy load, SRC will dominant. When load get lighter, characteristic of PRC will floating to the top. With these interesting characteristics, we could design the converter working at the resonant frequency of SRC to achieve high efficiency. Then we are able to operate the converter at lower than resonant frequency of SRC still get ZVS because of the characteristic of PRC will dominant in that frequency range. From above discussion, the DC characteristic of LLC resonant converter could be also divided into three regions according to different mode of operation as shown

in Figure 3.20. Our designed operating regions are region 1 and region 2. Region 3 is ZCS region. The converter should be prevented from entering region 3. The simulation waveform for region 1 and region 2 are shown in Figure 3.21 and Figure 3.22. In fact, there are many other operating modes for LLC resonant converter as load changes.

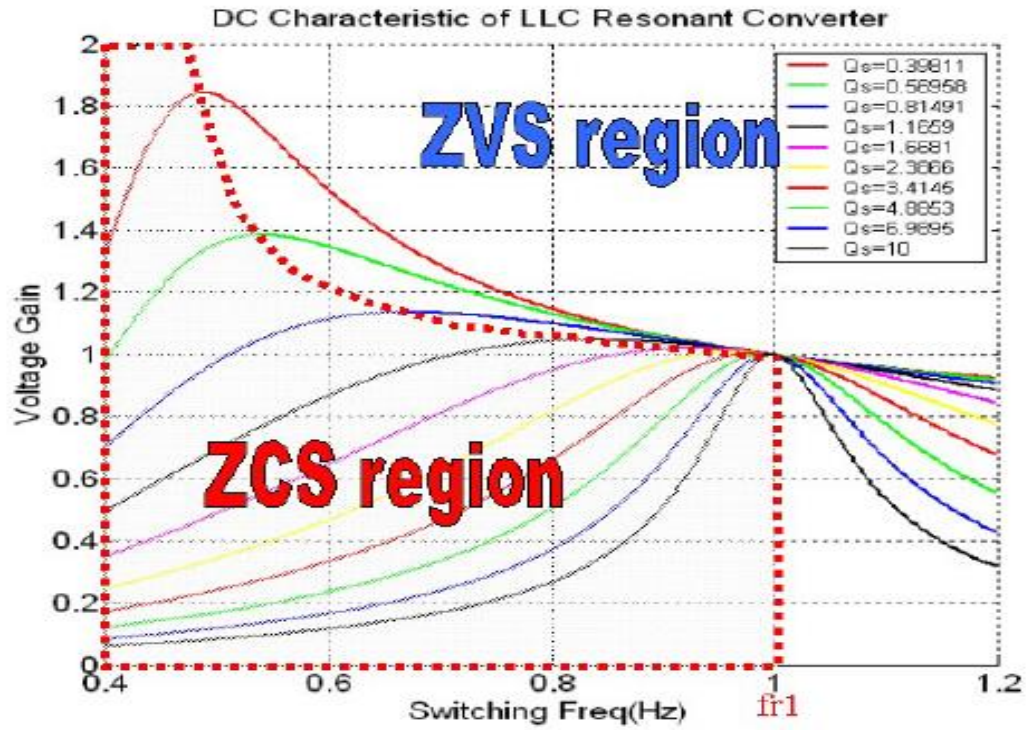


FIGURE 47 DC CHARACTERISTIC OF LLC RESONANT CONVERTER [26]

In region 1, the converter works very similar to SRC. In this region,  $L_{12}$  never resonates with resonant capacitor  $C_r$ ; it is clamped by output voltage and acts as the load of the series resonant tank. With this passive load, LLC resonant converter is able to operate at no load condition without the penalty of very high switching frequency. Also, with passive load  $L_{12}$ , ZVS could be ensured for any load condition.

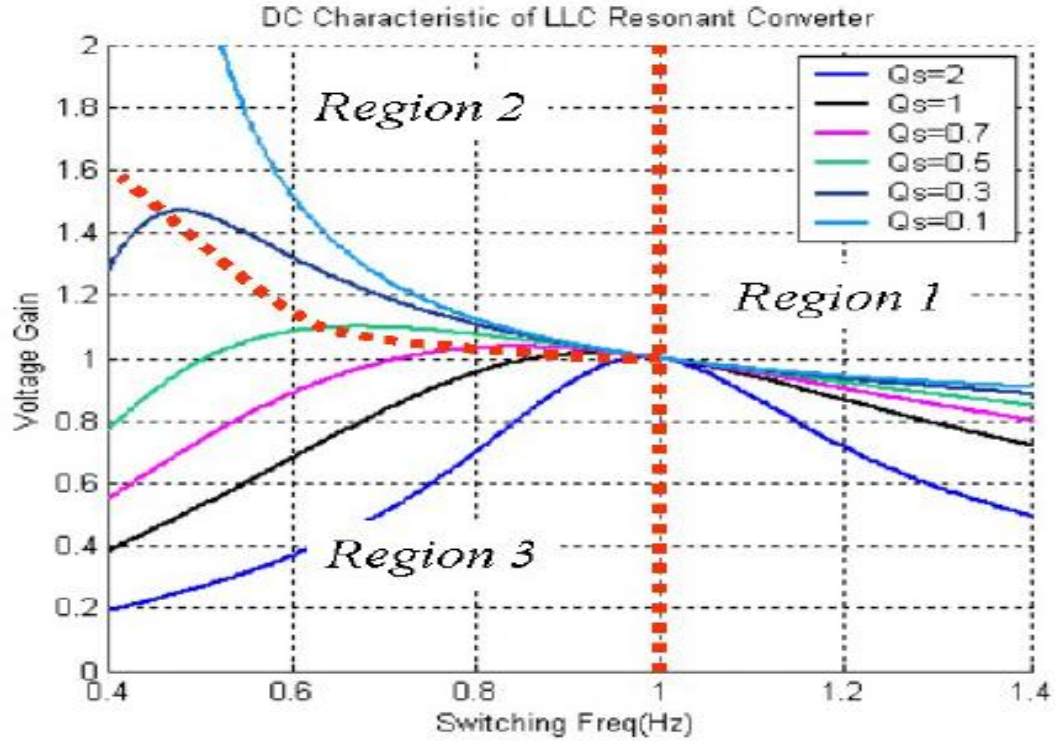


FIGURE 48 REFERENCE DIAGRAM OF THREE OPERATING REGIONS OF RESONANT CONVERTER [26]

In region 2, the operation of LLC resonant converter is more complex and interesting. The waveforms could be divided into clearly two time intervals. In the first time interval,  $L_{11}$  resonant with  $C_{11}$ .  $L_{12}$  is clamped by output voltage. When  $L_{11}$  current resonant back to same level as  $L_{12}$  current, the resonant of  $L_{11}$  and  $C_{11}$  is stopped, instead, now  $L_{12}$  will participate into the resonant and the second time interval begins. During this time interval, the resonant components will change to  $C_{11}$  and  $L_{12}$  in series with  $L_{11}$ , which is shown in the waveforms as a flat region. In fact, that is a part of the resonant process between  $L_{12}$  and  $L_{11}$  with  $C_{11}$ . From this aspect, LLC resonant converter is a multi-resonant converter since the resonant frequency at different time interval is different. Because of the resonant between  $L_{12}$  and  $C_{11}$ , a peak on the gain appears at resonant frequency of  $L_{12}+L_{11}$  and  $C_{11}$ .

Next the operating of LLC resonant converter in region 2 will be discussed in detail. It is divided into three modes.

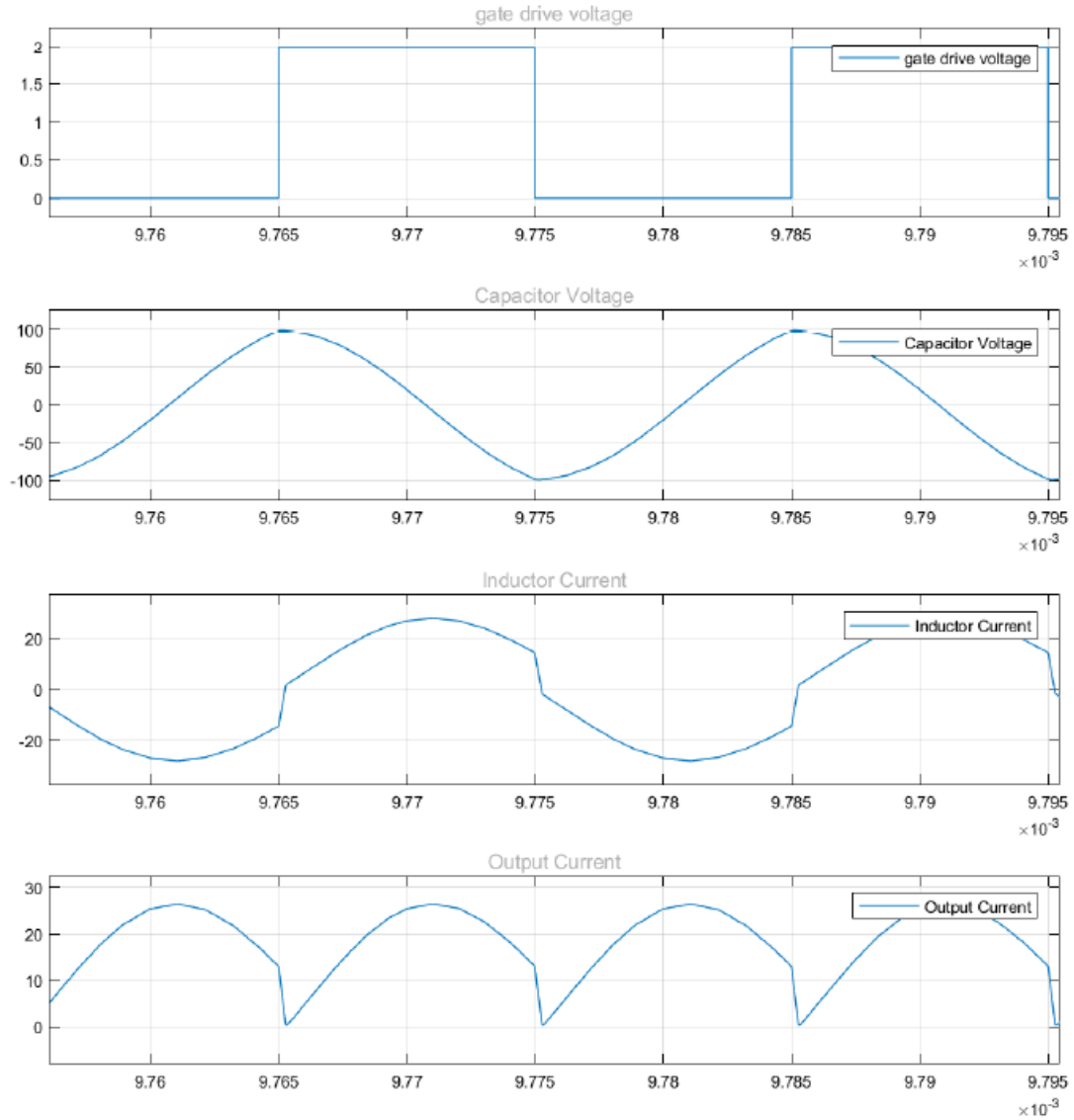


FIGURE 49 SIMULATED OPERATIONAL WAVEFORMS IN REGION 1

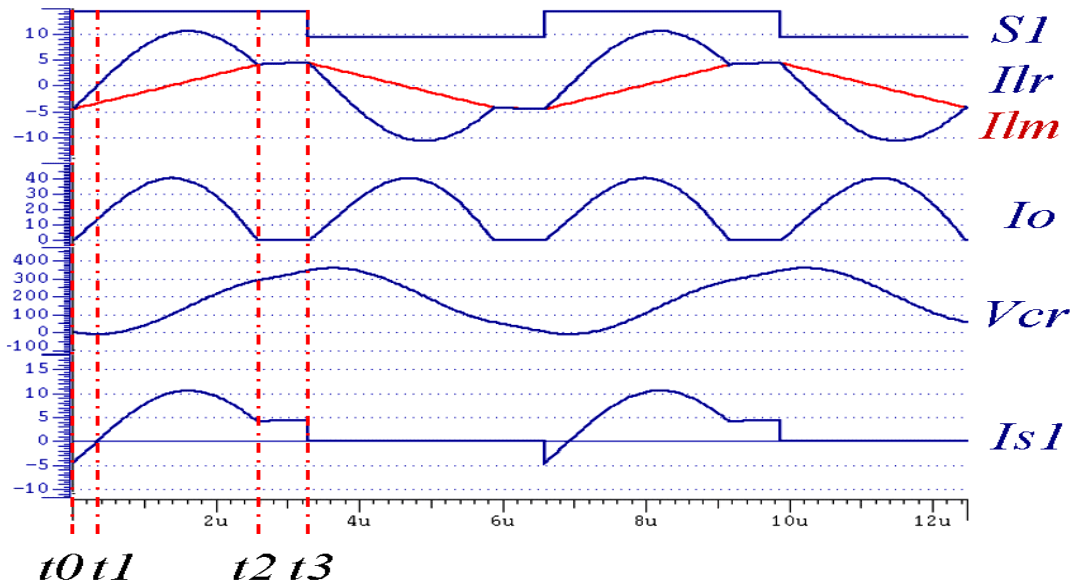


FIGURE 50 REFERENCE DIAGRAM OF SIMULATION WAVEFORMS IN REGION 2 [26]

Mode 1 ( $t_0$  to  $t_1$ ):

This mode begins when Q2 is turned off at  $t_0$ . At this moment, resonant inductor L11 current is negative; it will flow through body diode of Q1, which creates a ZVS condition for Q1. Gate signal of Q1 should be applied during this mode.

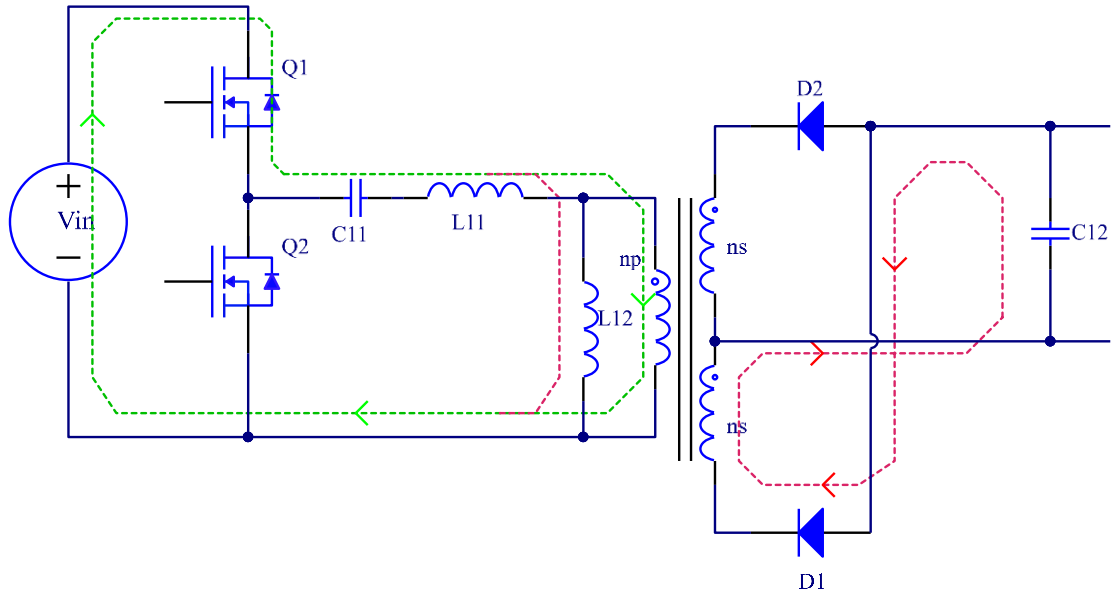


FIGURE 51 SIMPLIFIED SCHEMATIC LLC RESONANT CONVERTER CIRCUIT DIAGRAM DURING MODE 1 IN REGION 2



When resonant inductor  $L_{11}$  current flow through body diode of Q1,  $I_{L11}$  begins to rise, this will force secondary diode D1 conduct and  $I_o$  begin to increase. Also, from this moment, transformer sees output voltage on the secondary side.  $L_{12}$  is charged with constant voltage.

Mode 2 ( $t_1$  to  $t_2$ )

This mode begins when resonant inductor current  $I_{L11}$  becomes positive. Since Q1 is turned on during mode 1, current will flow through MOSFET Q1.

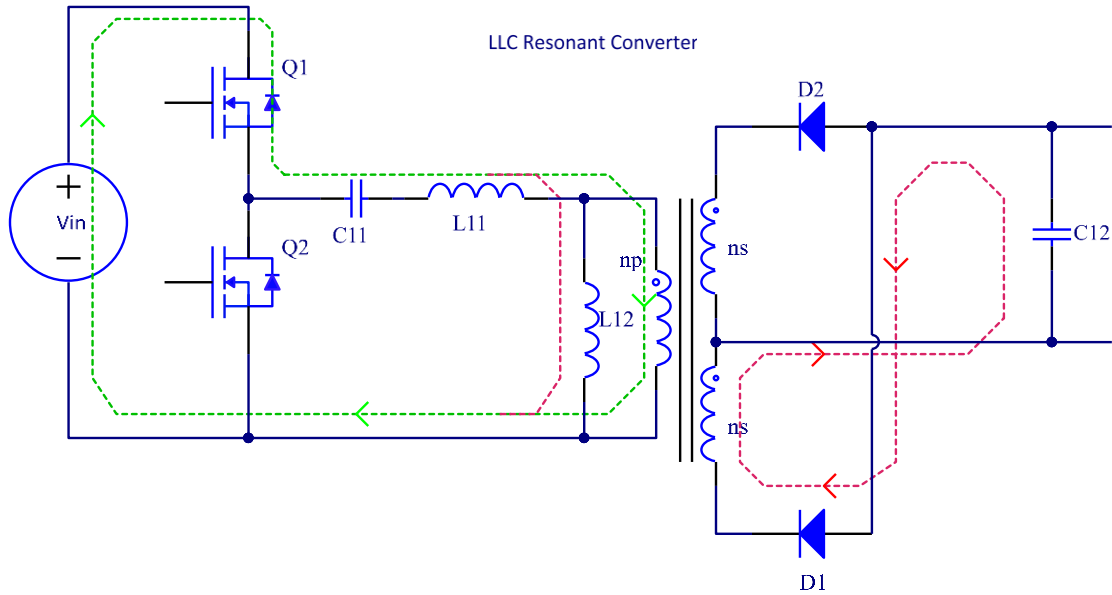


FIGURE 52 CIRCUIT DIAGRAM DURING MODE 2 IN REGION 2

During this mode, output rectifier diode D1 conduct. The transformer voltage is clamped at  $V_o$ .  $L_{12}$  is linearly charged with output voltage, so it doesn't participate in the resonant during this period. In this mode, the circuit works like a SRC with resonant inductor  $L_{11}$  and resonant capacitor  $C_{11}$ . This mode ends when  $L_{11}$  current is the same as  $L_{12}$  current. Output current reach zero.

Mode 3 ( $t_2$  to  $t_3$ )

At  $t_2$ , the two inductor's currents are equal. Output current reach zero. Both output rectifier diodes D1 and D2 is reverse biased. Transformer secondary voltage is lower than output voltage. Output is separated from transformer.

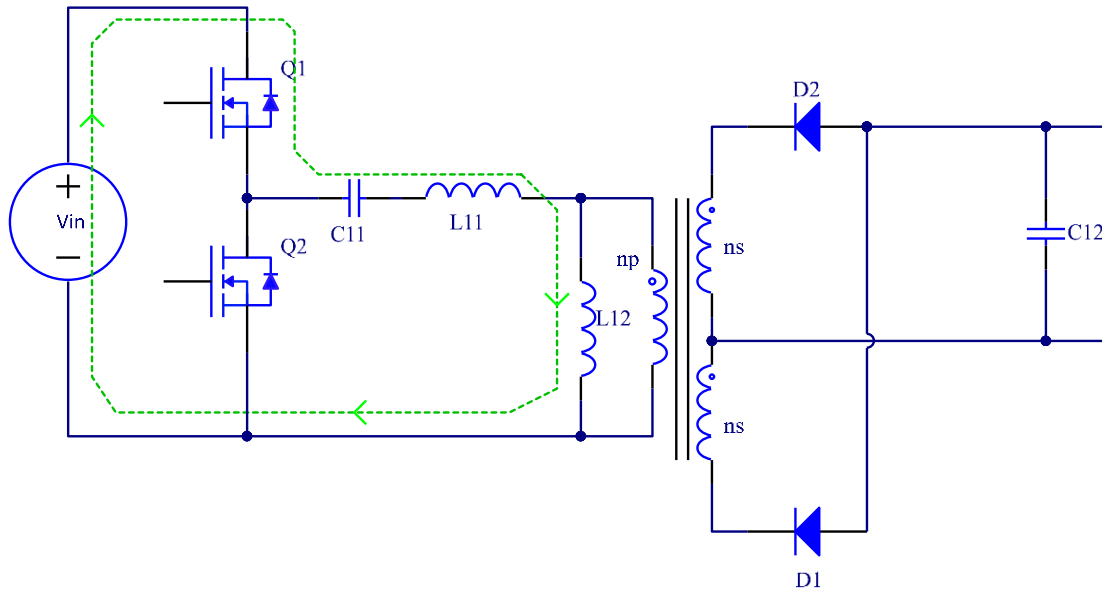


FIGURE 53 CIRCUIT DIAGRAM DURING MODE 3 IN REGION 2

During this period, since output is separated from primary,  $L_{12}$  is freed to participate resonant. It will form a resonant tank of  $L_{12}$  in series with  $L_{11}$  resonant with  $C_{11}$ .

This mode ends when Q1 is turned off. As can be seen from the waveform, Q1 turn off current at  $t_3$  is small compare with peak current. For next half cycle, the operation is same as analyzed above. From the simulation waveform we can see, the MOSFETs are turned on with ZVS. The ZVS is achieved with magnetizing current, which is not related to load current, so ZVS could be realized even with zero-load. Since this magnetizing current is also the turn off current of MOSFET. Choosing different magnetizing inductance could control it. The turn off current could be much smaller than load current, so turn off loss can be reduce. Also, the secondary side diode current reduce to zero and stay off, the

reverse recovery is eliminated also. With all these, the switching loss of this converter is very small. Design of LLC resonant converter 3.2.4. Design of power stage parameters from above analysis, the DC characteristic of LLC resonant converter could be derived. Based on the DC characteristic, parameters in power stage can be designed. The parameters need to be designed are:

- Transformer turns ratio:  $n$
- Series resonant inductor:  $L_{11}$
- Resonant capacitor:  $C_{11}$
- Resonant inductor ratio:  $L_{12}/L_{11}$

The specifications for the design are:

Input voltage range: 300V to 400V, normal operating region (360-400V)

Output voltage: 48V

Maximum load: 2.5 Ohm

Maximum switching frequency: 200 kHz

With above information, we can begin to choose the parameters. For front-end application, the target is to optimize the performance at high input voltage. From previous analysis results, the optimal operating point for this converter is when switching frequency equals to the resonant frequency of  $L_{11}$  and  $C_{11}$ . At this point, the voltage gain of LLC resonant converter is 1. Base on this, the transformer turns ratio can be choose. For Half Bridge LLC resonant converter with 400V input and 48V output, the transformer turns ratio can be choose base on following equations:

#### HALF BRIDGE TRANSFORMER TURNS RATIO

$$N = V_{IN} / (2 V_O) \quad (3-3)$$

## FULL BRIDGE LLC RESONANT CONVERTER TURN'S RATIO

$$N = V_{IN} / V_O \quad (3-4)$$

In our design, a half bridge LLC resonant converter is used; the turn's ratio was chosen to be 4. After the transformer turns ratio, the resonant tank can be designed. To determine the resonant tank, lot of tradeoffs are involved. Three design examples will be shown to demonstrate the tradeoffs.

### 3.2.4.1 PHASE 1: THE RATIO OF TWO RESONANT INDUCTORS IS 1

In this design, the ratio of two resonant inductors is 1, which means the two resonant inductors are with same value. The region of Q is from 1(Full load) to 0(no load). Here Q is defined as:  $Q = Z_o / R_l$ . Resonant inductor  $L_{11}$  is  $27.8\mu H$ , and  $C_{11}$  is  $22.8nF$ .

Simulation waveform is shown in Figures 3.26 and 3.27.

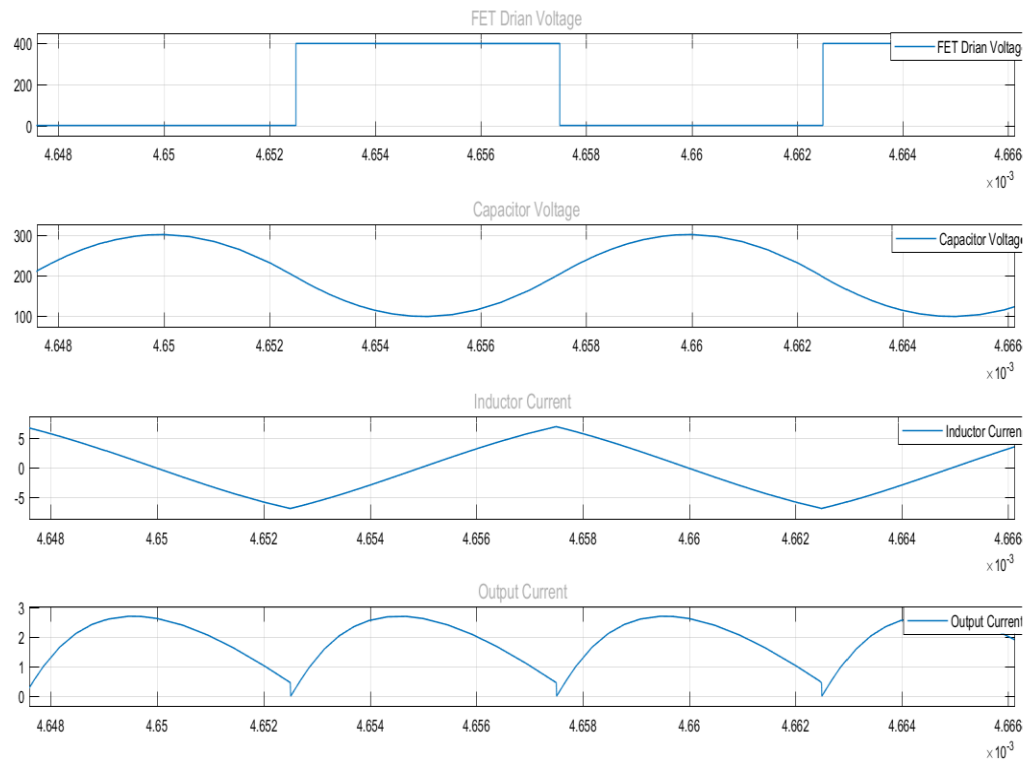


FIGURE 54 SIMULATION WAVEFORMS OF PHASE 1 WITH 400V

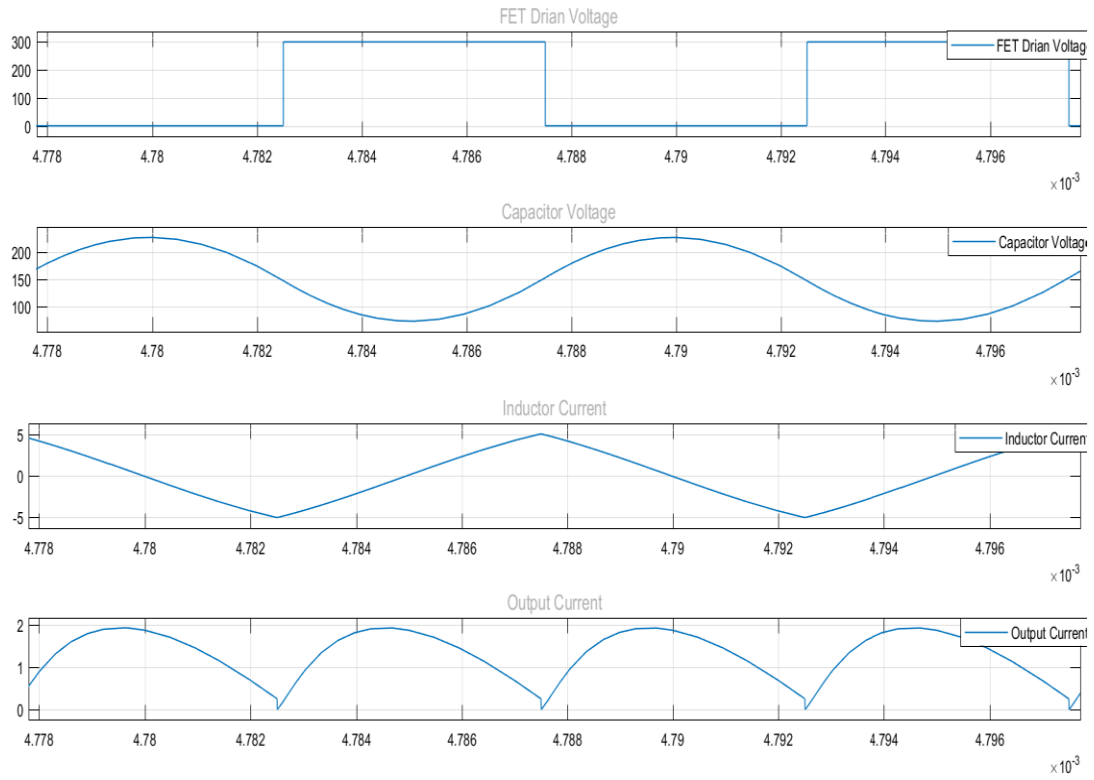


FIGURE 55 SIMULATION WAVEFORMS OF PHASE 1 WITH 300V

#### 3.2.4.2 PHASE 2: THE RATIO OF TWO RESONANT INDUCTORS IS 4

In this design, the ratio of two resonant inductors is 4, which means  $L_{12}$  is four times  $L_{11}$ .

The region of Q is from 0.5 (Full load) to 0 (no load). Resonant inductor  $L_{11}$  is  $17\mu\text{H}$  and  $L_{12}$  is  $70\mu\text{H}$ . Resonant capacitor is  $24\text{nF}$ .

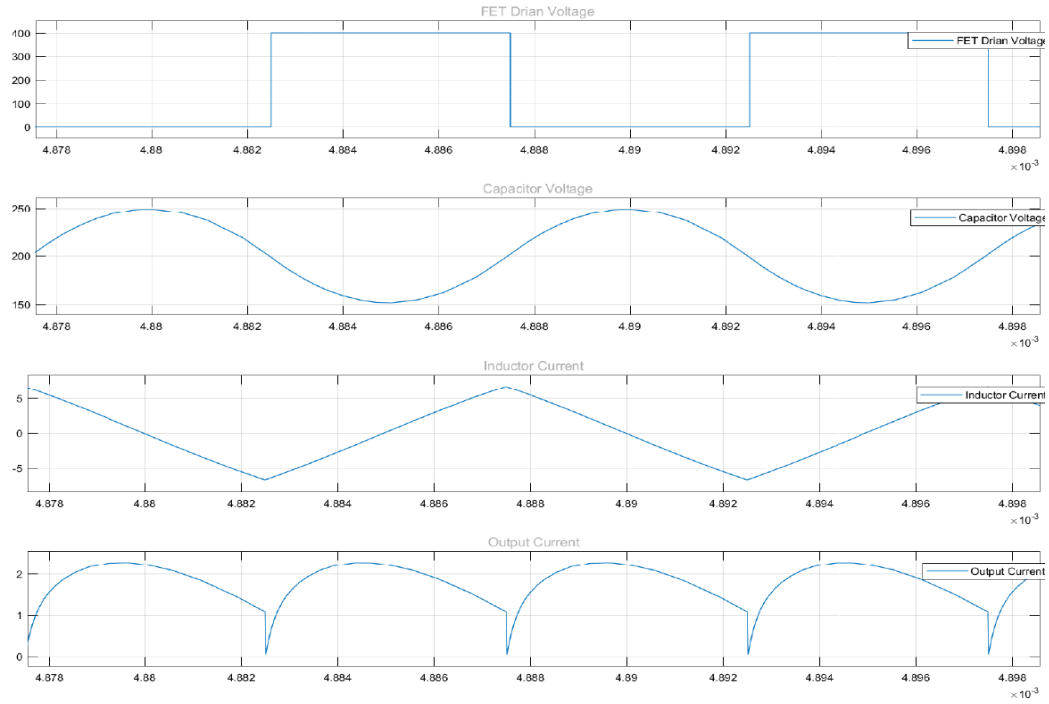


FIGURE 56 SIMULATION WAVEFORMS OF PHASE 2 WITH 400V

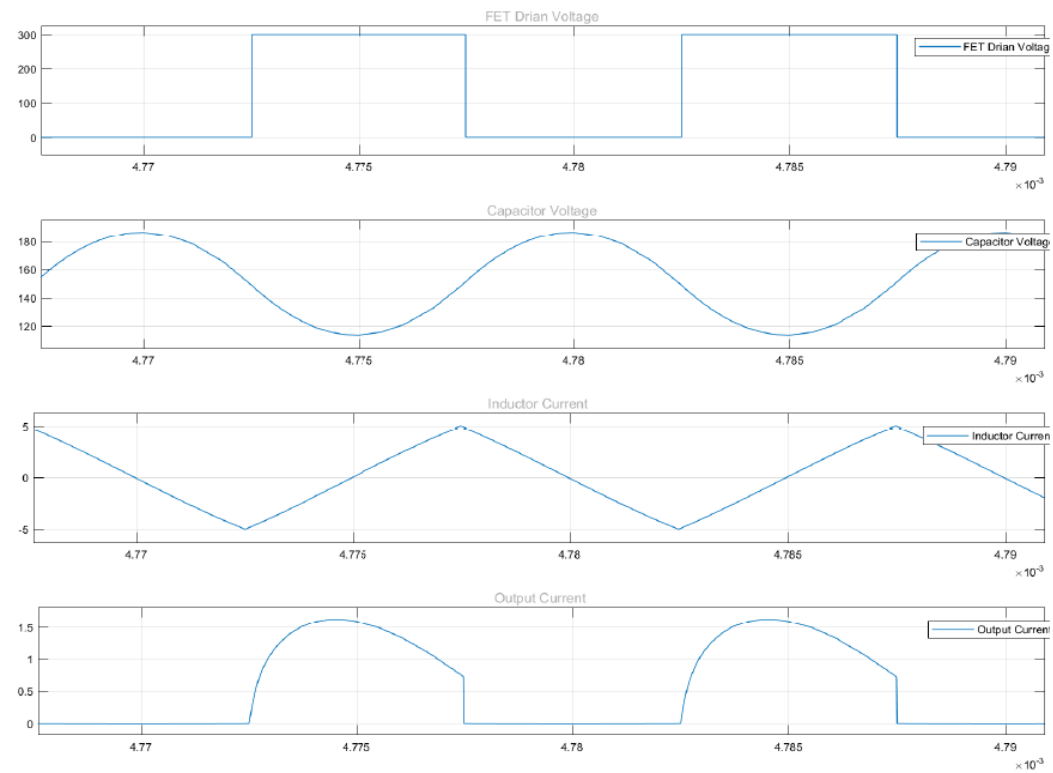


FIGURE 57 SIMULATION WAVEFORMS OF PHASE 2 WITH 300V

### 3.2.4.3 PHASE 3: THE RATIO OF TWO RESONANT INDUCTORS IS 16

In this design, the ratio of two resonant inductors is 16, which means  $L_{12}$  is sixteen times  $L_{11}$ . The characteristic and operating region are shown in Figure 56. The region of  $Q$  is from 0.25 (Full load) to 0 (no load). Resonant inductor  $L_{11}$  is  $7.95\mu\text{H}$ ,  $L_{12}$  is  $127\mu\text{H}$  and  $C_{11}$  is  $79.6\text{nF}$ .

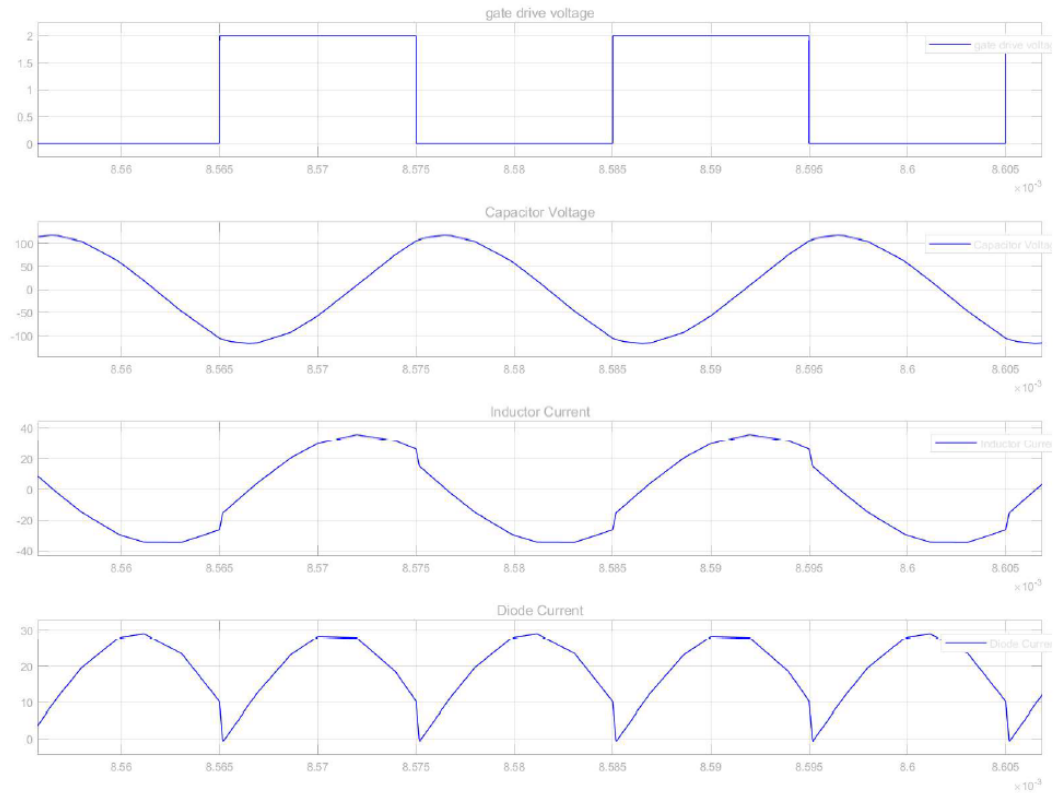


FIGURE 58 SIMULATION WAVEFORMS OF PHASE 3 WITH 400V

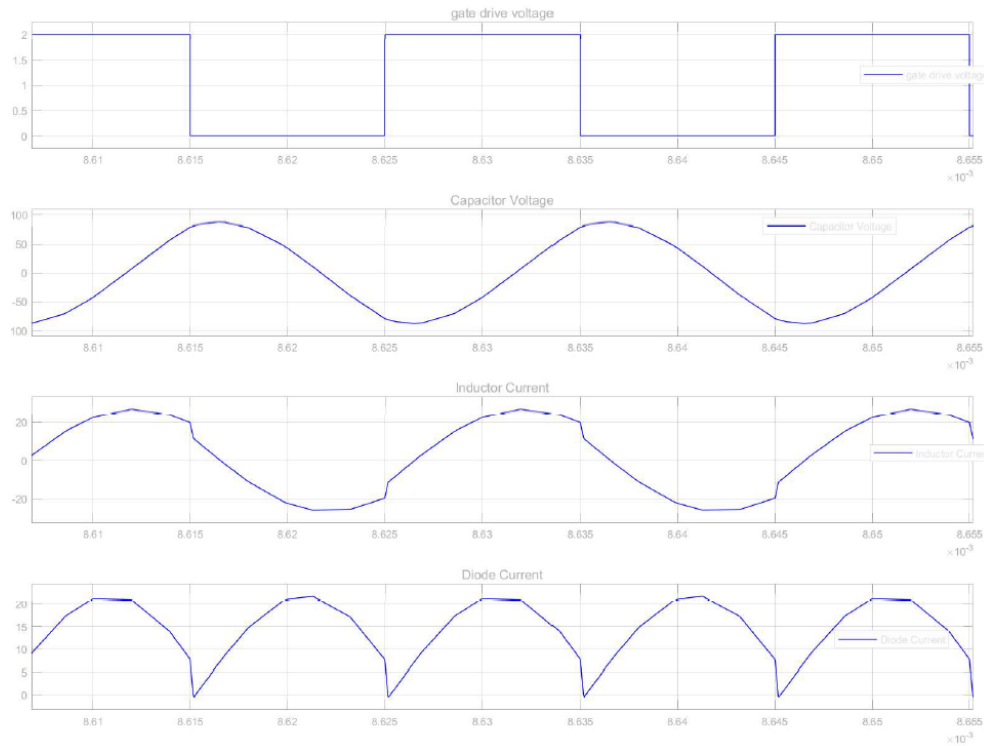


FIGURE 59 SIMULATION WAVEFORMS OF PHASE 3 WITH 300V

### 3.2.5 SUMMARY

In Figures 3.32 to Figure 3.34, primary switching and conduction loss are compared for three designs with different input voltage.

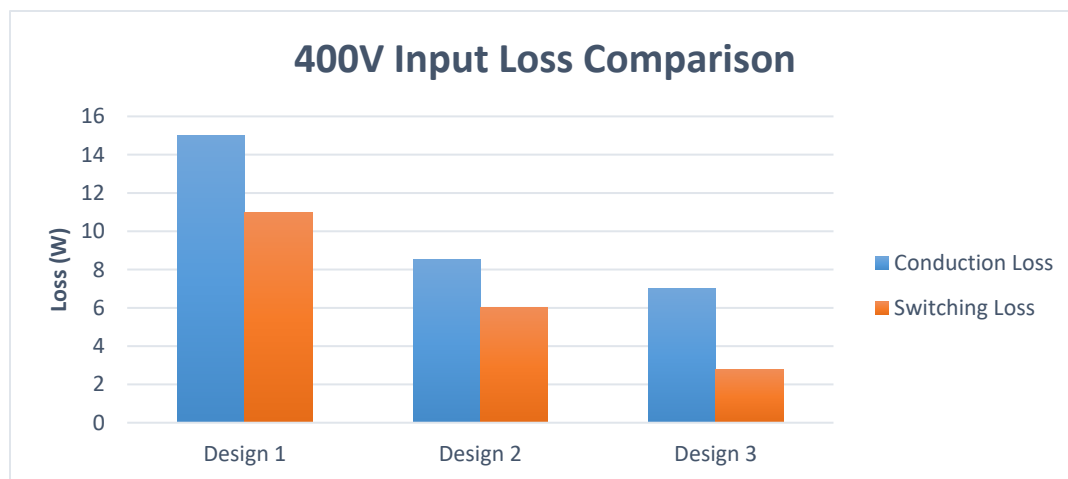


FIGURE 60 PRIMARY LOSS FOR THREE DESIGNS WITH  $V_{IN} = 400V$



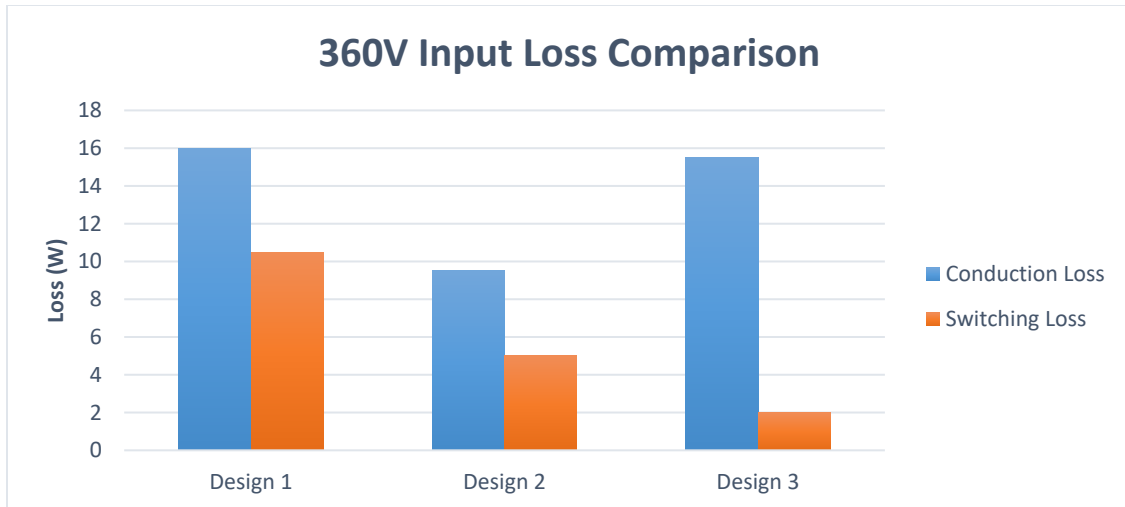


FIGURE 61 PRIMARY LOSS FOR THREE DESIGNS WITH  $V_{IN} = 360V$

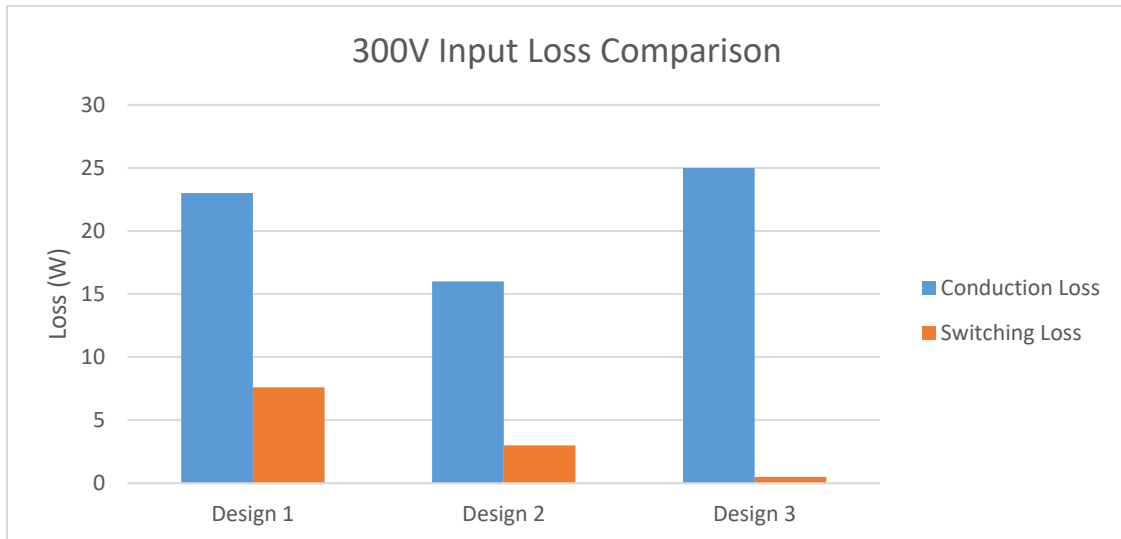


FIGURE 62 PRIMARY LOSS FOR THREE DESIGNS WITH  $V_{IN} = 300V$

From the summary Table 3-2, design 3 provides best performance at 400V input, but the switching frequency range will be much larger. For design 1, the performance at 400V is compromised; the benefit is very narrow switching frequency range. For this application, since the output voltage of PFC circuit is not tightly regulated, it has a range from 360 to 400V. The performance at 360V is also a concern.

TABLE 3-2 SUMMARY OF THREE LLC RESONANT CONVERTER DESIGNS

	Q Range	Fs range	Primary RMS Current	Switch Turn off current	Resonant Cap Voltage	Peak Output Current
Design 1	1 to 0	175k to 200k	8.1A to 9.2A	7.8A to 5.8A	800V	31A to 43A
Design 2	0.5 to 0	135k to 200k	6.0A to 8.3A	4.1A to 3.2A	440V	31A to 49A
Design 3	0.25 to 0	72k to 200k	5.7A to 10.2A	1.9A to 0.24A	430V	31A to 89A

From these comparisons, although design 3 could provide better performance at 400V input, its performance degrades very fast as input voltage drops. Design 1 could provide more balanced performance for whole range, but the performance at 400V input is greatly impaired. Design 2 is choosing for front-end application with 200 kHz design. With design 2, the performance is balanced within input range. Stress on different devices is reasonable.

## Chapter 4. WIRELESS POWER TRANSFER SERIES-SERIES/PARALLEL RESONANT CONVERTER

### 4.1 INTRODUCTION

In the previous chapter we determined that SS and SP are the topologies which lend themselves well to battery charger applications. In this chapter we will investigate WPT scenario we will investigate the (SS) and (SP) Inductive Power Transfer topologies.

### 4.2 WIRELESS POWER TRANSFER

Because of many parameters used in specification of a WPT, Wireless Power Transfer, system, it has to be designed and adapted to individual conditions and there is no one universal solution. WPT, transformers usually operate under much a lower magnetic coupling factor due to the lower coupling factor  $k$  used for the two halves cores with a large air gap WPT. [25]

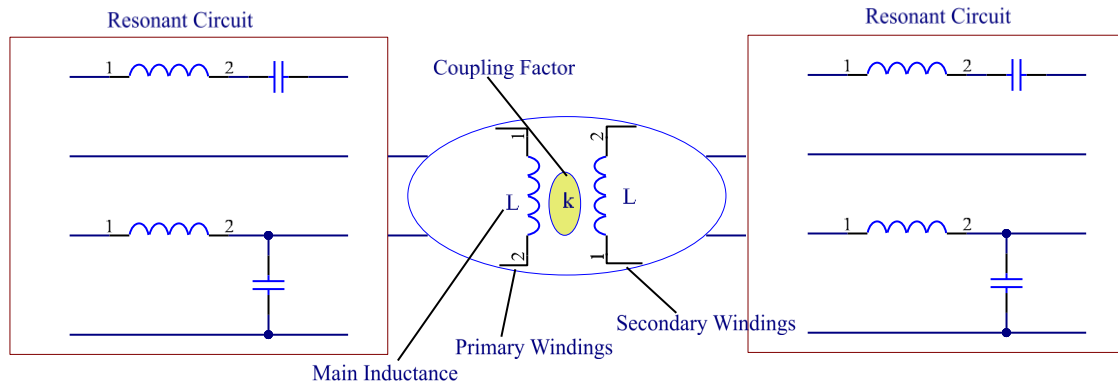


FIGURE 63 SIMPLIFIED SCHEMATIC DIAGRAM OF RESONANT MODE CONVERTER COMPONENTS

As a result, the main inductance is very small whereas leakage inductances associated with the coupling between primary and secondary windings are large as compared with conventional transformers. Consequently, increase in magnetizing current causing higher conducting losses. These winding losses increase because of large leakage inductances.

When the primary capacitance is varied, the reactive parts of the impedance on the primary side no longer cancel each other out. The impedance on the primary side increases, causing the current through the primary coil to decrease. In accordance with equation the induced voltage in the secondary coil decreases with the current through the primary coil. Since the current through the primary coil is no longer in phase with the source voltage, the power factor decreases. [28] Another disadvantage of transformers with relatively large gap is electromagnetic compatibility (EMC) problem (strong radiation).

Comparing (SS) with (SP) parameters, it can be seen that selected topology influences strongly the correct choice of the primary capacitance. An important advantage of (SS) topology is that primary capacitance is independent of either magnetic coupling factor or the load.

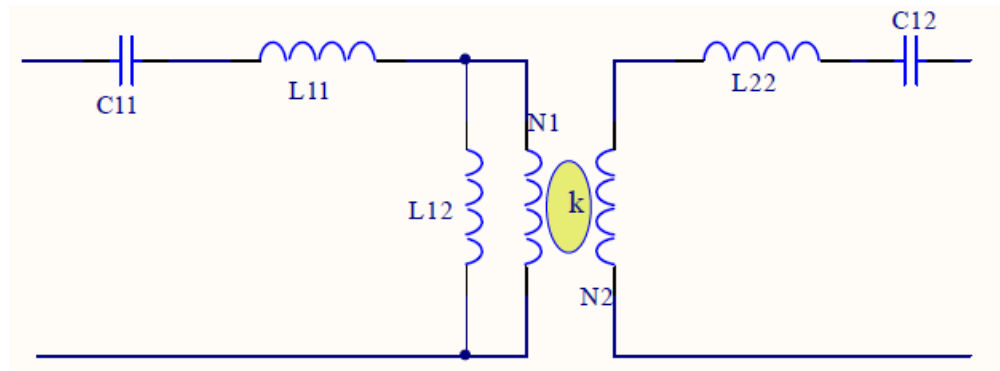


FIGURE 64 SIMPLIFIED SCHEMATIC DIAGRAM OF RESONANT MODE SERIES-SERIES WPT

TABLE 4-1 SUMMARY OF SERIES-SERIES CONVERTER

Abbreviation	Comments	Advantages	Disadvantages
Series-Series SS	Systems with intermediate DC voltage bus	Independent of either magnetic coupling factor or the load	Sensitivity to load changes

Contrary to this, the (SP) topology depends on coupling factor and requires higher value of capacitance for stronger magnetic coupling. [25] Due to the nature of battery charging (SP) may be the best choice since it is not as susceptible to load changes.

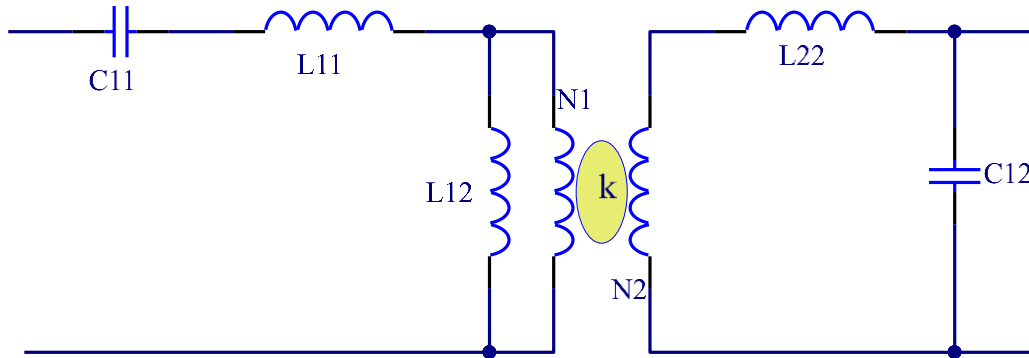


FIGURE 65 SIMPLIFIED SCHEMATIC DIAGRAM OF RESONANT MODE SERIES-PARALLEL WPT

TABLE 4-2 SUMMARY OF SERIES-PARALLEL CONVERTER

Abbreviation	Comments	Advantages	Disadvantages
Series-Parallel SP	Current source output) Battery Charging	Not as susceptible to load changes	Sensitivity to Coupling changes higher value of capacitance for stronger magnetic coupling

#### 4.2.1 WPT PARALLEL-SERIES RESONANT CONVERTER

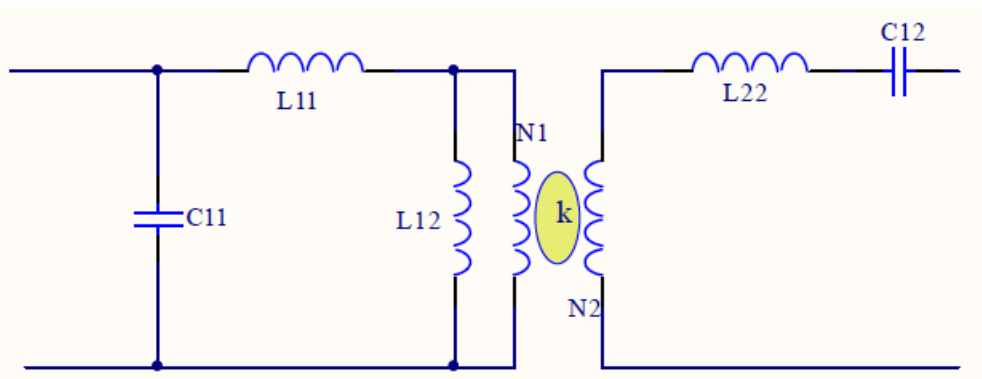


FIGURE 66 SIMPLIFIED SCHEMATIC OF PARALLEL-SERIES RESONANT CONVERTER

When the primary side is parallel compensated, the primary compensation capacitance does not influence the current through the primary coil. The current,  $I_{L12}$ , through the primary coil- $L_{12}$ , determined by the input voltage,  $U_1$ , the impedance of the primary coil and the total impedance of the secondary side as seen by the primary coil. The expression for the current through the primary coil is given by equation:

EXPRESSION FOR THE CURRENT THROUGH THE PRIMARY COIL [29].

$$I_{L12} = \frac{U_1}{j \cdot \omega \cdot L_1 + \frac{\omega^2 \cdot M^2}{Z_2}} \quad (4-1)$$

MUTUAL INDUCTANCE OF AN INDIVIDUAL COIL IS REPRESENTED BY [29]

$$M = \frac{\mu_0 \cdot \mu_r \cdot N_1 \cdot N_2 \cdot A}{l} \quad (4-2)$$

Where:

- $\mu_0$  is the permeability of free space ( $4 \cdot \pi \cdot 10^{-7}$ )
- $\mu_r$  is the relative permeability of the soft iron core
- $N$  is in the number of coil turns
- $A$  is in the cross-sectional area in  $m^2$
- $l$  is the coils length in meters

The mutual inductance of two air coils of which their distance is  $D$  can be approximately expressed as

#### MUTUAL INDUCTANCE OF TWO AIR COILS SEPARATED BY A DISTANCE D [29]

$$M = \frac{\pi \mu_0 r^4 N^2}{2D^3} \quad (4-3)$$

in which  $\mu_0$  is permeability of vacuum,  $r$  is the radius of the coils,  $N$  is the number of turns,  $D$  is the distance of two coils which are coaxial. In other words, if the size and parameter of the coils are fixed, a larger  $D$  means a smaller mutual inductance  $M$ .

The Mutual Inductance of two coils with high permeability cores can be approximated as;

#### MUTUAL INDUCTANCE OF TWO COILS WITH HIGH PERMEABILITY CORES [29]

$$M = k \cdot \sqrt{L_{11} \cdot L_{22}} \quad (4-4)$$

Where  $L_{11}$  and  $L_{22}$  are the primary and secondary inductance of the coils respectively,  $k$  is the coupling coefficient or the percentage of magnetic of the lines of flux from the first coil are cutting the second coil. Generally, the amount of inductive coupling that exists between the two coils is expressed as a fractional number between 0 and 1 instead of a percentage (%) value, where 0 indicates zero or no inductive coupling, and 1 indicating full or maximum inductive coupling. In other words, if  $k = 1$  the two coils are perfectly coupled, if  $k > 0.5$  the two coils are said to be tightly coupled and if  $k < 0.5$  the two coils are said to be loosely coupled.

As can be seen by equation (3.5) the current through the primary coil is independent of the primary compensation capacitance,  $C_{11}$ . Since the current through the primary coil determines the induced voltage in the secondary coil, the secondary side is unaffected by the primary compensation capacitance,  $C_{11}$ . The change in primary compensation

capacitance does however move the primary side out of resonance. The primary current increases and since it is no longer in phase with the voltage, the power factor decreases. When the primary side was series compensated, the resonance of the primary side kept the secondary side output independent of the impedance of the secondary side. But due to the nature of the parallel compensation, the primary compensation capacitance does not affect the current through the primary coil.

TABLE 4-3 SUMMARY OF PARALLEL TO SERIES CONVERTER

Abbreviation	Comments	Advantages	Disadvantages
Parallel-Series PS	Systems with Intermediate Bus Voltages	Primary compensation capacitance does not affect the current through the primary coil	Sensitive to Coupling Changes

#### 4.2.2 WPT PARALLEL TO PARALLEL RESONANT CONVERTER

As with the parallel-series compensation topology, the current through the primary coil is independent of the primary compensation capacitance,  $C_{11}$ . Thus it does not affect the output of the secondary side. It does however cause a phase shift, resulting in a reduced power factor. Since the current through the primary coil is independent of the primary compensation capacitance, the primary compensation capacitance cannot keep the secondary output independent of the secondary impedance. As can be seen in figure 4.5, when the secondary side is parallel compensated it is the secondary compensation capacitance,  $C_{12}$ , that keeps the output current independent of the load resistance. When the secondary side no longer is in resonance the output current no longer remains constant.



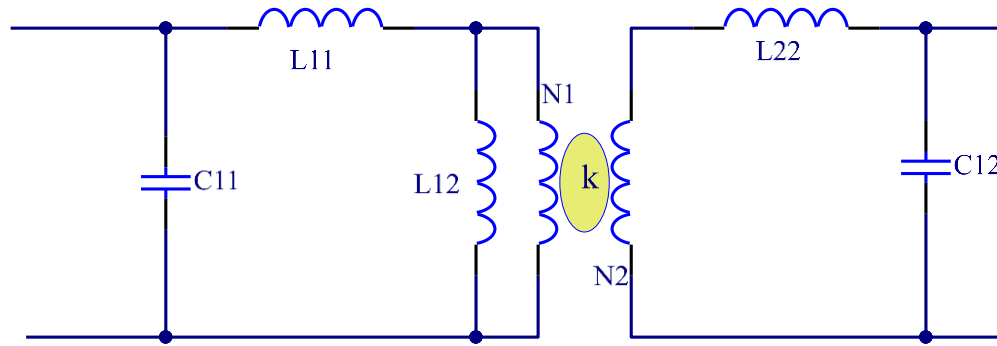


FIGURE 67 SIMPLIFIED SCHEMATIC OF PARALLEL-PARALLEL RESONANT CONVERTER

TABLE 4-4 SUMMARY OF PARALLEL TO PARALLEL CONVERSION

Abbreviation	Comments	Advantages	Disadvantages
Parallel-Parallel PP	(Current Source Output) Battery Charging	Current through the primary coil is independent of the primary compensation capacitance	Sensitive to Coupling Changes

#### 4.2.3 DESIGN TRADE-OFFS

In design of power stage, there are some tradeoffs that will affect the final results. First trade-off is switching frequency range and switching loss. With smaller magnetizing inductance, narrower switching frequency range can be achieved, but switching loss and conduction loss will increase because of high magnetizing current.

Another trade off to make is switching frequency range and resonant tank impedance. For the same specification,  $L_{11}$  and  $C_{11}$  can have different values, which will work. Although there is a limit on how small  $C_{11}$  can be in order to keep series resonant tank working in the constant gain region. With larger  $C_{11}$ , the voltage stress on  $C_{11}$  will be smaller. The problem is that the impedance of the resonant tank will be small too, which will affect the short circuit performance. With smaller tank impedance, the higher the short circuit current

will be and higher switching frequency is needed to limit the output current. The problem with low switching frequency is the conduction loss will increase as switching frequency drops. As shown in first part, the conduction loss can be doubled when switching frequency change from 200 kHz to 150 kHz.

From these trade-offs, the optimized design should choose as small resonant capacitor as possible to get enough voltage gain at heavy load. Then  $L_{12}$  should be as large as possible to get the voltage gain with desired switching frequency range.

#### 4.2.3.1 RESULTS AND COMPARISONS

Base on the design, a LLC resonant converter is built with the values determined. The test circuits are shown in Figures 3.34, 3.35, 3.36 and 3.37 with the part number of the devices. Test waveforms are shown in Figure 51 and 52. The test efficiency is shown in Table 2. Compare with asymmetrical half bridge converter, LLC resonant converter could improve the efficiency at normal operation point by more than 3%. Table 2 shows the test efficiency at different input voltage. LLC resonant converter could cover wide input range with much higher efficiency compared with PWM converter.

Because of the two halves cores used and/or air gap WPT, Wireless Power Transfer, transformers usually operate under much lower magnetic coupling factor. [25]

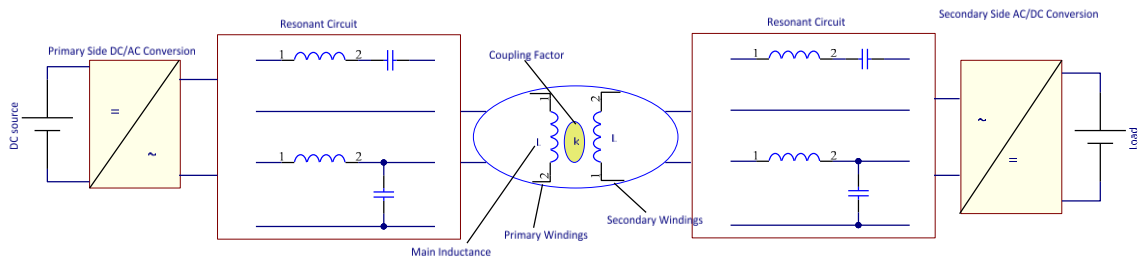


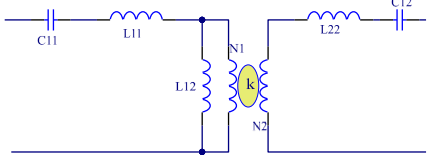
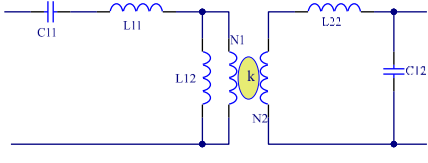
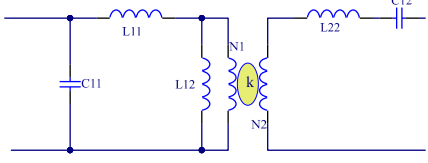
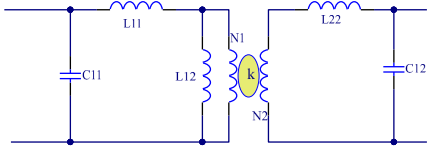
FIGURE 68 SIMPLIFIED DIAGRAM OF WIRELESS POWER TRANSFER SYSTEM [25]

As a result, the main inductance  $L_{12}$  very small whereas leakage inductances ( $L_{11}$  (see Table 4) is,  $L_{22}$ ) are large as compared with conventional transformers. Consequently, increase in magnetizing current causes higher conducting losses. Also, winding losses increase because of large leakage inductances. Another disadvantage of transformers with relatively large gap is electromagnetic compatibility (EMC) problem (strong radiation). To form resonant circuits and compensate for the large WPT transformer leakage inductances, two methods can be applied [25]: S-series or P-parallel, giving four basic topologies: (SS), (SP), (PS), and (PP) (first letter denotes primary and second a secondary compensation—see Table 3.7).

The (PS) and (PP) topologies require an additional series inductor to regulate the inverter current flowing into the parallel resonant tank. This additional inductor increases EMC distortion, converter size, and the total cost of WPT system.

Assuming the same number of primary winding,  $N_1=N_2$ , the basic parameters of (SS) and (SP) topologies have been summarized in table below, where  $G_v = u_s/u_I$  – voltage output-input transfer function of WPT system;  $w=w_s/w_0$  – normalized frequency;  $k$  – magnetic coupling factor; and  $R_0$  – load resistance on the secondary side.

TABLE 4-5 SUMMARY OF TOPOLOGIES

Simplified Circuit	Abbreviation	Comments	Sensitivity for Coupling and Load Changes
	Series-Series (SS)	Systems with Intermediate Bus Voltages	Sensitive to Load Changes
	Series-Parallel (SP)	(Current Source Output) Battery Charging	Sensitive to Coupling Changes
	Parallel-Series (PS)	Systems with Intermediate Bus Voltages	Sensitive to Coupling Changes
	Parallel-Parallel (PP)	(Current Source Output) Battery Charging	Sensitive to Coupling Changes

Comparing (SS) with (SP) parameters, it can be seen that selected topology influences strongly the correct choice of the primary capacitance. An important advantage of (SS) topology is that primary capacitance is independent of either magnetic coupling factor or the load. Contrary to this, the (SP) topology depends on coupling factor and requires higher value of capacitance for stronger magnetic coupling. [25]

Secondary Impedance Load Voltage/Current, and Properties at Secondary Resonant Frequency

TABLE 4-6 SECONDARY IMPEDANCE AND LOAD VOLTAGE/CURRENT

Compensation	Series	Parallel
Secondary Impedance $Z_s$	$j\omega L_s + \frac{1}{j\omega C_s} + R$	$j\omega L_s + \frac{1}{j\omega C_s + \frac{1}{R}}$
Load Voltage $V_L$	$I_s \cdot R$	$V_s$
Load Current $I_L$	$I_s$	$\frac{V_s}{R}$

TABLE 4-7 PROPERTIES AT THE SECONDARY RESONANT FREQUENCY  $\omega_0$ 

Compensation	Series	Parallel
Reflected Resistance	$\frac{\omega_0^2 M^2}{R}$	$\frac{M^2 \cdot R}{L_s^2}$
Reflected Reactance	0	$-\frac{\omega_0^2 M^2}{L_s}$
Secondary Quality Factor $Q_s$	$\frac{\omega_0 \cdot L_s}{R}$	$\frac{R}{\omega_0 \cdot L_s}$

However, resonant converters exhibit several disadvantages. Although, the components of an RC can be chosen such that good performance with high efficiency is obtained at a single operating point, typically it is difficult to optimize the resonant components in such a way that good performance is obtained over a wide range of load currents and input voltages variations. Significant currents may circulate through the tank components, even when the load is removed, leading to poor efficiency at light loads. Therefore, the converter used in WPT system has to be carefully designed. [30] [31, 32] Typical steady-state

waveforms of the voltages  $u_1$  ,  $u_2$  ; currents  $i_1$  ,  $i_2$ ; and primary side power  $P_1$  in an insulated gate bipolar transistor-based WPT resonant full-bridge converter with series-series compensation for operation at resonance frequency are presented in Figure 36.5. The rotatable transformer air gap is 25.5 mm, the load resistance 10  $\Omega$ , and transferred power is 2.5 kW [32]. It can be seen that resonant converter operates with zero primary current switching.

#### 4.2.4 SERIES-SERIES AND SERIES-PARALLEL RESONANT POWER CONVERTER CONSIDERATION FOR HIGH POWER WPT DESIGN

Resonant power converters discussed in the previous sections leads us to two basic topologies for consideration Series-Series and Series Parallel. Both contain resonant L–C networks with characteristics that should favor battery charging design. These converters contain low total harmonic distortion because switching frequency is equal to first harmonic frequency. Basic power converter topologies used in WPT systems are presented in Figure 3.1 and 3.5.

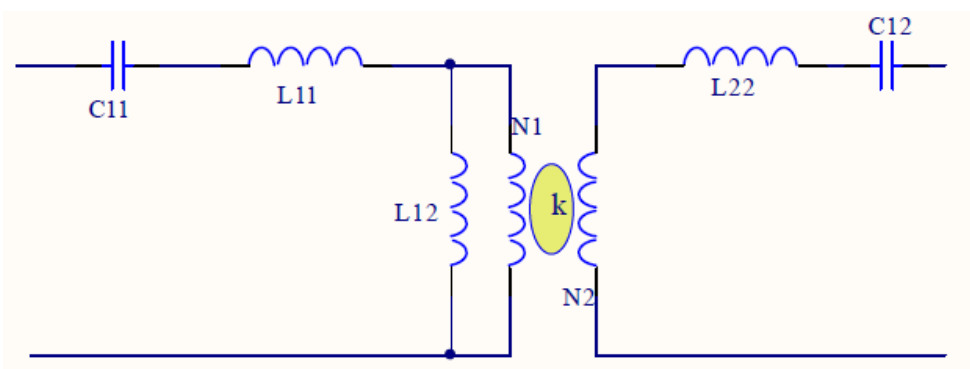


FIGURE 69 SIMPLIFIED SCHEMATIC OF SERIES-SERIES RESONANT CONVERTER

Voltage Transfer Function  $G_{Vss}$  [33]

$$G_{Vss} = \sqrt{\left[1 + \frac{1-k}{k} \cdot \left(1 - \frac{1}{\omega^2}\right)\right]^2 + \left[Q_{ss} \cdot \left(\omega - \frac{1}{\omega}\right) \left[1 + \frac{1-k}{2k} \cdot \left(1 - \frac{1}{\omega^2}\right)\right]\right]^2} \quad (4-5)$$

RESONANT ANGULAR FREQUENCY  $\omega_0$

$$\omega_0 = \frac{1}{\sqrt{L_r \cdot C_r}} \quad (4-6)$$

RESONANT CAPACITORS  $C_{11}$ ,  $C_{22}$  RATIO

$$C_{11} = C_{22} \quad (4-7)$$

CIRCUIT QUALITY FACTOR  $Q_{ss}$  [33]

$$Q_{ss} = \frac{\omega(L_{11} + L_{22})}{R_{es}} \quad (4-8)$$

EQUIVALENT LOAD RESISTOR " $R_{es}$ " [33]

$$R_{es} = \frac{8}{\pi^2} R_0 \quad (4-9)$$

VOLTAGE TRANSFER FUNCTION  $G_{Vsp}$  [33]

$$G_{Vsp} = \frac{1}{\sqrt{1 + (1-k^2) \cdot \left(1 - \frac{\omega}{\omega_0}\right)^2 + Q_{ss}^2 \cdot \left[\left(\frac{\omega}{\omega_0}\right) \cdot \left(\frac{\omega_0}{\omega}\right)\right]^2}} \quad (4-10)$$

#### RESONANT ANGULAR FREQUENCY $\omega_0$

$$\omega_0 = \frac{1}{\sqrt{L_r \cdot C_r}} \quad (4-11)$$

#### RESONANT CAPACITORS $C_{11}, C_{22}$ [33]

$$C_{11} = \frac{1}{1 - k^2} C_{22} \quad (4-12)$$

#### CIRCUIT QUALITY FACTOR $Q_{sp}$ [33]

$$Q_{sp} = \frac{R_{ep}}{\omega \cdot (L_{11} + L_{22})} = \frac{R_{ep}}{\omega \cdot L_r} \quad (4-13)$$

#### EQUIVALENT LOAD RESISTOR $R_{EP}$ [33]

$$R_{ep} = \frac{\pi^2}{8} R_0 \quad (4-14)$$

The main advantage of resonant technique is reduction of switching losses via mechanisms known as zero current switching (ZCS) and zero voltage switching (ZVS). The switch-on and/or switch-off converter semiconductor components can occur only at zero crossing of the resonant quasi-sinusoidal waveforms. This eliminates some of the switching loss mechanisms. Hence, switching losses are reduced, and resonant converters can operate at switching frequencies that are considerably higher than in comparable pulse width modulation (PWM) hard switching converters. ZVS can also eliminate or reduce some of the electromagnetic emission sources, also known as electromagnetic interference. Another advantage is that both ZVS and ZCS converters can utilize transformer leakage inductance and diode junction capacitors as well as the output parasitic capacitor of the power switch. The induced and reflected voltages in this model are specified in terms of



the mutual inductance “M”, the operational frequency “w”, and the primary and secondary currents. The mutual inductance is related to the magnetic coupling coefficient by

MAGNETIC COUPLING COEFFICIENT "k"[33]

$$k := \frac{M}{\sqrt{L_p \cdot L_s}} \quad (4-15)$$

The reflected impedance from the secondary to the primary can be found by dividing the reflected voltage by the primary current resulting in

THE REFLECTED IMPEDANCE FROM THE SECONDARY TO THE PRIMARY  $Z_R$ [33]

$$Z_r := \frac{\omega^2 M^2}{Z_s} \quad (4-16)$$

“ $Z_r$ ” is the impedance of the secondary network and depends on the selected compensation topology. The power transferred from the primary to the secondary is the reflected resistance multiplied by the square of primary current as given by

REFLECTED POWER TRANSFER FROM PRIMARY TO SECONDARY[33]

$$P := (R_e \cdot Z_r) \cdot I_p^2 \quad (4-17)$$

The operator “ $R_e$ ” represents the real component of corresponding variable.

## Chapter 5. DESIGN, MODELING AND SIMULATION FOR 7.5KW WIRELESS CHARGER

### 5.1 INTRODUCTION: PRACTICAL IMPLEMENTATION OF WIRELESS DESIGN

In the previous chapter a separate inductor was placed series with the transformer and the inductor was used as the inductive portion of the tuned LC circuit. In this chapter the LLC or Series-Series wireless power transfer's primary and secondary inductance will be used to form the inductive portion of the tuned LC circuit. By using the transformer the leakage inductance will be an active portion of the tuned circuit. Using small increments in capacitor values placed in parallel to obtain a well-tuned circuit will make the design easier to implement in the real world application. Adding a location for a secondary inductor will also allow of better tuning and reduce secondary ripple current.

### 5.2 INITIAL DESIGN PARAMETERS

Looking at the results from the previous chapters we will design a charger based on an LLC primary and a matching LC secondary or design approach. We will compare this to the LC primary with matching LC secondary. This design will be based on a full bridge topology similar to the Simplified Schematic shown below.

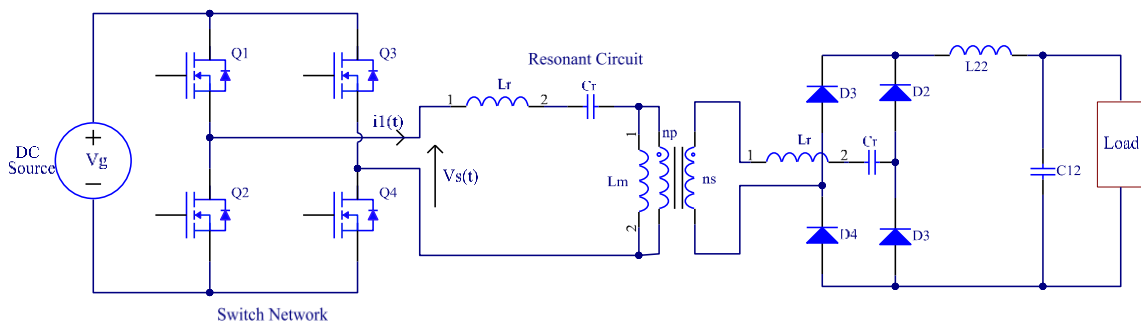


FIGURE 70 SIMPLIFIED FULL BRIDGE LLC - (SP) DESIGN SCHEMATIC

With the following design parameters we will select the each component.

$$f_s := 50\text{kHz} \quad P_o := 7500\text{W}$$

$$V_g := 400\text{V} \quad V_o := 380\text{V}$$

$$V_{oc} := 600\text{V}$$

To determine the individual components of the circuit it will first be broken down into sections. See Figure 4.2

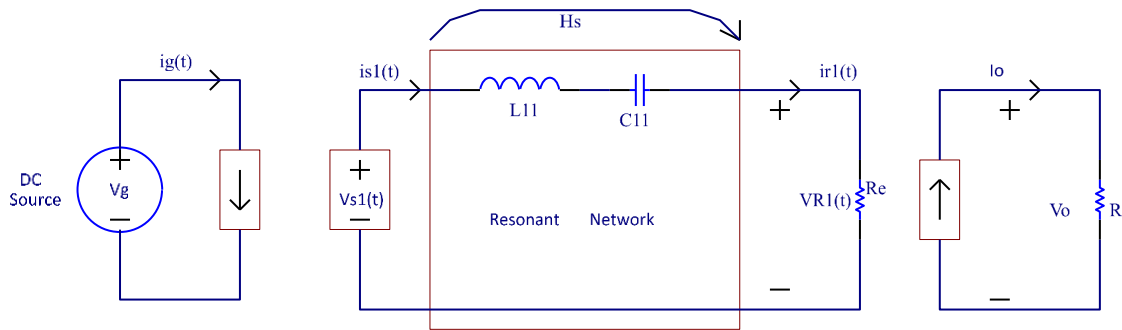


FIGURE 71 SIMPLIFIED BLOCK DIAGRAM OF A FULL BRIDGE

From here we determine  $I_{out}$  and  $R_{out}$  using ohm's law

$R_{OUT}$  USING OHM'S LAW

$$R_o := \frac{V_o^2}{P_o} = 19.253\Omega \quad (5-1)$$

$I_{OUT}$  USING OHM'S LAW

$$I_o := \frac{P_o}{V_o} = 19.737\text{A} \quad (5-2)$$

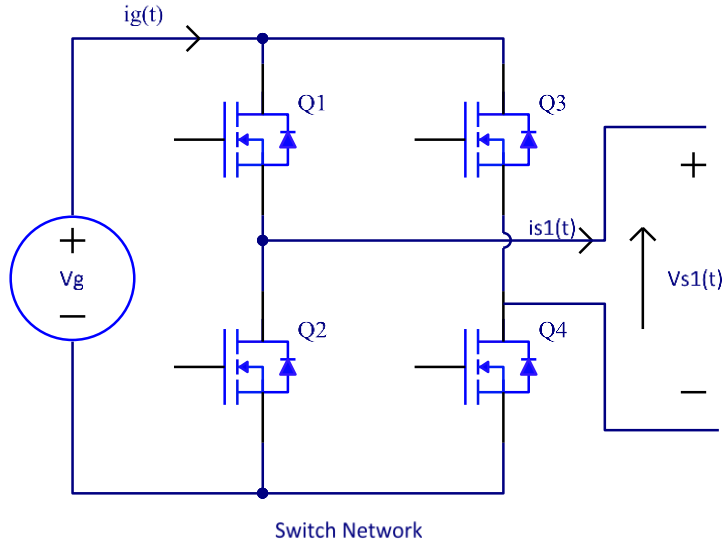


FIGURE 72 SWITCH BANK

We can calculate the fundamental component of  $V_{s1(t)}$  switch has a peak value of 2 times the DC input voltage  $V_{in}$

FUNDAMENTAL COMPONENT OF  $V_{s1}$

$$V_{s1} := \frac{N_s}{N_p} V_{in} \quad (5-3)$$

$$V_{s1} = 360 \text{ V}$$

The DC component, or average value, of the input current can be found by averaging  $I_{g(t)}$  over one half switching period

INPUT CURRENT  $I_G$  [23]

$$I_g := \frac{2I_{s1}}{\pi} \quad (5-4)$$

Next we examine the output section to determine  $V_{R1}$

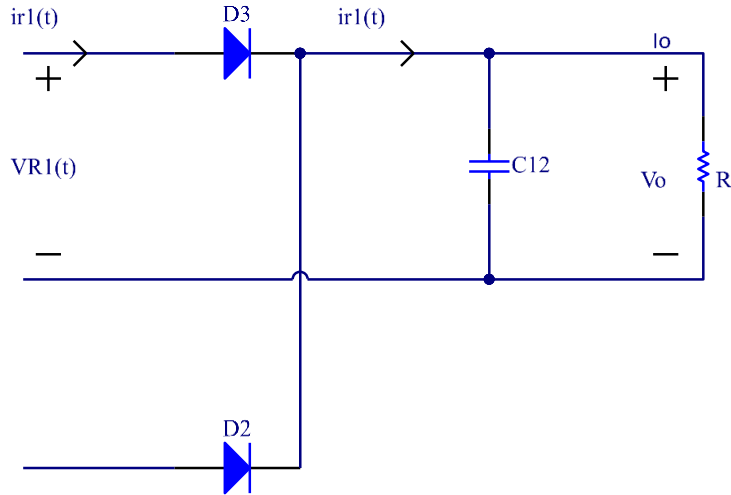


FIGURE 73 RECTIFIER/FILTER SECTION

From here we determine the peak value of  $V_{R1}$  which it  $4/\pi$  times the DC output voltage  $V_o$  and is in phase with the current  $I_{R(t)}$

PEAK VALUE OF  $V_{R1}$ [23]

$$V_{R1} := \frac{4}{\pi} V_o \quad (5-5)$$

$$V_{R1} = 483.831V$$

As an intermediate step we calculate  $R_e$  from  $R_o$

RATION BETWEEN  $R_e$  FROM  $R_o$  [23]

$$R_e := \frac{8}{\pi^2} R_o \quad (5-6)$$

$$R_e = 15.606\Omega$$

We can now calculate  $I_{R1}$  [23]

$$I_{R1} := \frac{V_{R1}}{R_e} \quad (5-7)$$

$$I_{R1} = 31.003A$$

We can now examine the relationship between  $I_o$  and  $I_{R1}$

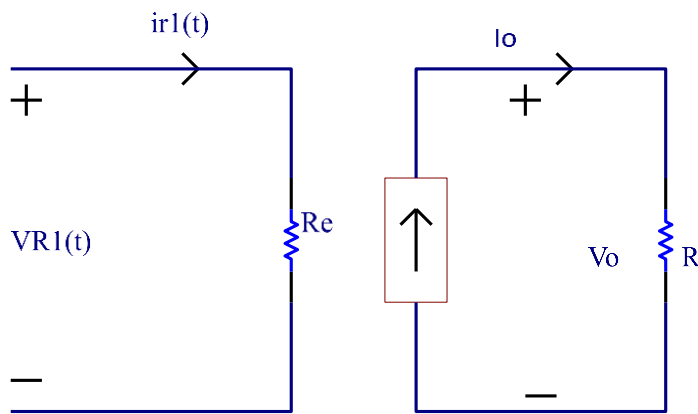


FIGURE 74 OUTPUT CHARACTERISTICS [23]

$$I_o := \frac{2}{\pi} I_{R1} \quad (5-8)$$

$$I_o = 19.737A$$

Next we examine the resonant tank network and its transfer function  $H_s$

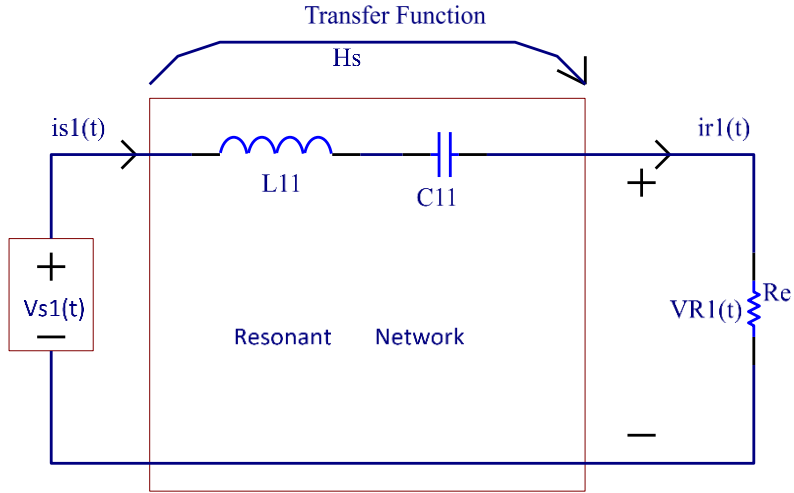


FIGURE 75 RESONANT TANK NETWORK

The magnitude of  $H_s$  is determined by the relationship of the voltage ration of  $V_{R1}$  and  $V_{s1}$

TRANSFER FUNCTION OF  $H_s$  AS A FUNCTION OF VOLTAGE [23]

$$H_s := \frac{V_{R1}}{V_{s1}} \quad (5-9)$$

$$H_s = 1$$

TRANSFER FUNCTION  $H_s$  AS A FUNCTION OF IMPEDANCE [23]

$$H_s := \frac{R_e}{Z_r} \quad (5-10)$$

$H_s$  WITH  $Z_R$  EXPANDED [23]

$$H_s := \frac{R_e}{\left( R_s + s \cdot L + \frac{1}{s \cdot C} \right)} \quad (5-11)$$

### LAPLACE TRANSFORM OF Hs [23]

$$H_s := \frac{\frac{s}{Q_e \cdot \omega_0}}{1 + \frac{s}{Q_e \cdot \omega_0} + \left(\frac{s}{\omega_0}\right)^2} \quad (5-12)$$

We also determine the open circuit transfer function  $H_\infty$

### OPEN CIRCUIT TRANSFER FUNCTION $H_\infty$ [23]

$$H_\alpha := \frac{V_{oc}}{V_{s1}} \quad (5-13)$$

$$H_\alpha = 1.963$$

We now calculate  $I_{nom}$  we need this value to determine

### NOMINAL CURRENT $I_{nom}$ [23]

$$I_{nom} := \frac{P_o}{V_{rms}} \cdot \sqrt{2} \quad (5-14)$$

$$I_{nom} = 39.43 \text{ A}$$

To determine the component values of the resonant circuit we calculate the short circuit current  $I_{sc}$ .

### SHORT CIRCUIT CURRENT [23]

$$I_{sc} := \frac{I_{nom}}{\sqrt{1 - \left(\frac{V_{nom}}{V_{oc}}\right)^2}} \quad (5-15)$$

$$I_{sc} = 127.6 \text{ A}$$



We now calculate the matched load and output impedance [23]

$$V_{\text{mat}} := \frac{V_{\text{oc}}}{\sqrt{2}} \quad (5-16)$$

$$V_{\text{mat}} = 282.843 \text{ V}$$

$$I_{\text{mat}} := \frac{I_{\text{nom}}}{\sqrt{2}} \quad (5-17)$$

$$I_{\text{mat}} = 27.881 \text{ A}$$

$$Z_o := \frac{V_{\text{oc}}}{I_{\text{sc}}} \quad (5-18)$$

$$Z_o = 3.135 \Omega$$

Now we can determine the element of the LC tank network.

Mutual inductance assuming perfect linkage between two coils the mutual inductance that exists between them can be expressed as [34, 35];

$$M := \frac{\mu \cdot \mu_0 \cdot N_1 \cdot N_2 \cdot Ae}{le}$$

$$M = 136.403 \text{ mH}$$

Since this is a contactless power transformer there will not be perfect linkage between the cores so taking the so we must take the distance between the core into consideration. In order to determine the tank LC network I will determine the coupling coefficient “k” based on the distance between the coils.

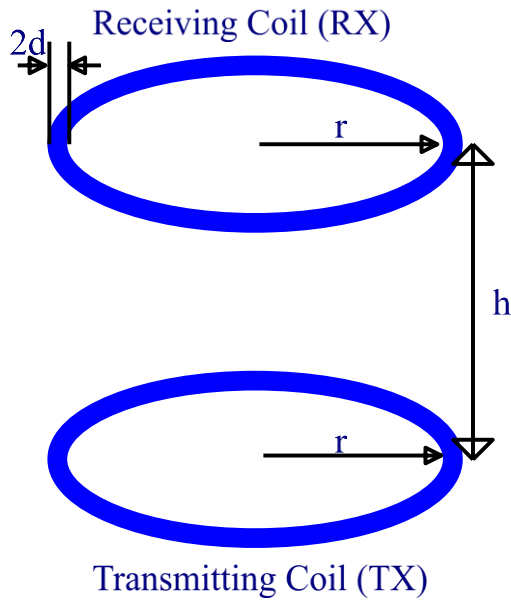


FIGURE 76 TRANSMIT AND RECEIVE COILS SEPARATED BY A DISTANCE H

$k$  is the coupling coefficient between two adjacent coils separated by a distance  $h$  [36].

$$k := \frac{4 \cdot r_1 \cdot r_2}{(r_1 + r_2)^2 + h^2} \quad (5-19)$$

$$k = 0.303$$

$h$  is the distance between the coils and  $r$  is the radius of the coil [36].

$$h = 20 \text{ cm}$$

$$r = 6.6 \text{ cm}$$

### 5.3 PHASE 1: MATCHING PRIMARY AND SECONDARY LC

The first and most critical value to derive is the primary and mutual inductance. Above the mutual inductance, “ $M$ ”, was determined based on ideal coupling but in a contactless

power transformer the ratio of the distance between the coils and diameter determine the best case mutual inductance “ $L_m$ ”. Mutual inductance,  $L_m$ , based on the distance between the coils and permeability of the core material,  $\mu$  and the permeability of air  $\mu_0$

$$L_m := \mu_0 \cdot \mu \cdot \frac{\sqrt{r_1 \cdot r_2}}{cm} \cdot \left[ \left( \frac{2}{k} - k \right) \cdot K(k) - \frac{2}{k} E(k) \right] \quad (5-20)$$

$$L_m = 112.422 \mu H$$

Coupling coefficient “ $k$ ” can also be expressed as a function of mutual inductance and primary and secondary inductances

$$k = \frac{L_m}{\sqrt{L_1 \cdot L_2}} \quad (5-21)$$

Since the primary and secondary inductance will be equal the inductance  $L$  is

$$L_T = \frac{L_m}{k} \quad (5-22)$$

$$L_T = 370.506 \mu H$$

With the mutual inductance and primary inductance determined the resonant capacitor value can be determined based on the simplification of equivalent resonant network.

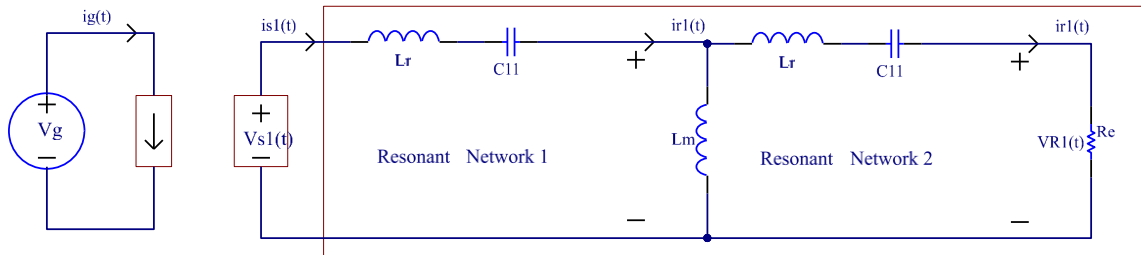


FIGURE 77 SIMPLIFIED SCHEMATIC OF DUAL RESONANT NETWORK

The equivalent rework combines  $L_r$  and  $C_r$  of the primary and secondary by placing the 2 networks in parallel.

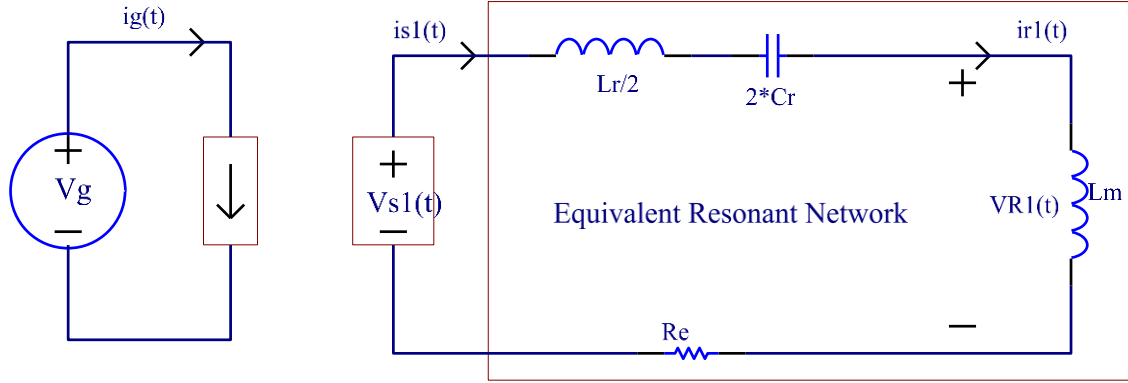


FIGURE 78 SIMPLIFIED SCHEMATIC OF COMBINED DUAL RESONANT NETWORK

With the equivalent network realized the resonant capacitor is determined based on a resonant frequency,  $f_r$  of 50 kHz.

$$f_r := \frac{1}{2\pi \sqrt{\left(L_m + \frac{L_r}{2}\right) \cdot C_r}} \quad (5-23)$$

Factoring for  $C_r$

$$C_r := \frac{1}{4 \cdot \pi^2 \cdot \left(\frac{L_r}{2} + L_m\right) \cdot f_r^2} \quad (5-24)$$

$$C_r = 0.034 \mu\text{F}$$

Determining the voltage across the capacitor,  $V_{xc}$ , as a function of  $X_c$  and load or primary current.

$$X_C := \frac{1}{2\pi f_r \cdot C_r}$$

$$X_C = 93.517\Omega$$

Both primary and secondary will have the same LC circuit and assuming a perfect transfer of power from capacitor to inductor we will use the conservation of energy equations multiplied by the power output to determine the voltage rating of capacitor and current rating of inductor.

$$P_o = \frac{1}{2} C_r \cdot V_c^2 \cdot f_r \quad (5-25)$$

$$V_c := \sqrt{\frac{2P_o}{C_r \cdot f_r}} \quad (5-26)$$

$$V_c = 2969.694V$$

$$P_o = \frac{1}{2} L_r \cdot I_r^2 \cdot f_r \quad (5-27)$$

$$I_L := \sqrt{\frac{2P_o}{L_r \cdot f_r}} \quad (5-28)$$

$$I_L = 31.729A$$

Derived Equation for Graphing Inductor current

Multiplication factors

X is a multiplication factor used to normalize the voltage across capacitor as a function of the energy required to achieve 7500W

$$X := \frac{V_c}{V_{in}} = 7.817 \quad (5-29)$$

Y is a multiplication factor used to normalize the current through the inductor as a function of the energy equations to achieve 7500W

$$Y := \frac{I_L}{I_{ave}} = 1.443 \quad (5-30)$$

Derive Inductor Current split into two section for clarity.

Beginning 0 to half the switching Frequency

$$I_{L1}(t) := \frac{V_c}{X_L(t) + (X_c(t))} \cdot \left( \Phi(t) - \Phi\left(t - \frac{T_s}{2}\right) \right) \quad (5-31)$$

Second half of inductor current

$$I_{L2}(t) := \frac{-V_c}{X_L\left(t - \frac{T_s}{2}\right) + X_c\left(t - \frac{T_s}{2}\right)} \cdot \left( \Phi\left(t - \frac{T_s}{2}\right) - \Phi\left(t - t_{on\_max} - \frac{T_s}{2}\right) \right) \quad (5-32)$$

$$I_{L\_total}(t) := (I_{L1}(t) + I_{L2}(t)) \cdot Y \quad (5-33)$$

Derived Equation for Graphing Capacitor Voltage

$$V_{c1}(t) := I_L(t) \cdot \frac{X_c(t)}{Y} \quad (5-34)$$

$$V_{c2}(t) := -I_L\left(t - \frac{T_s}{2}\right) \cdot \frac{X_c\left(t - \frac{T_s}{2}\right)}{Y} \cdot \left(\Phi\left(t - \frac{T_s}{2}\right) - \Phi\left(t - t_{on\_max} - \frac{T_s}{2}\right)\right) \quad (5-35)$$

$$V_{c\_total}(t) := (V_{c1}(t) + V_{c2}(t))Y - \frac{V_{c1}(T_s)}{2}Y \quad (5-36)$$

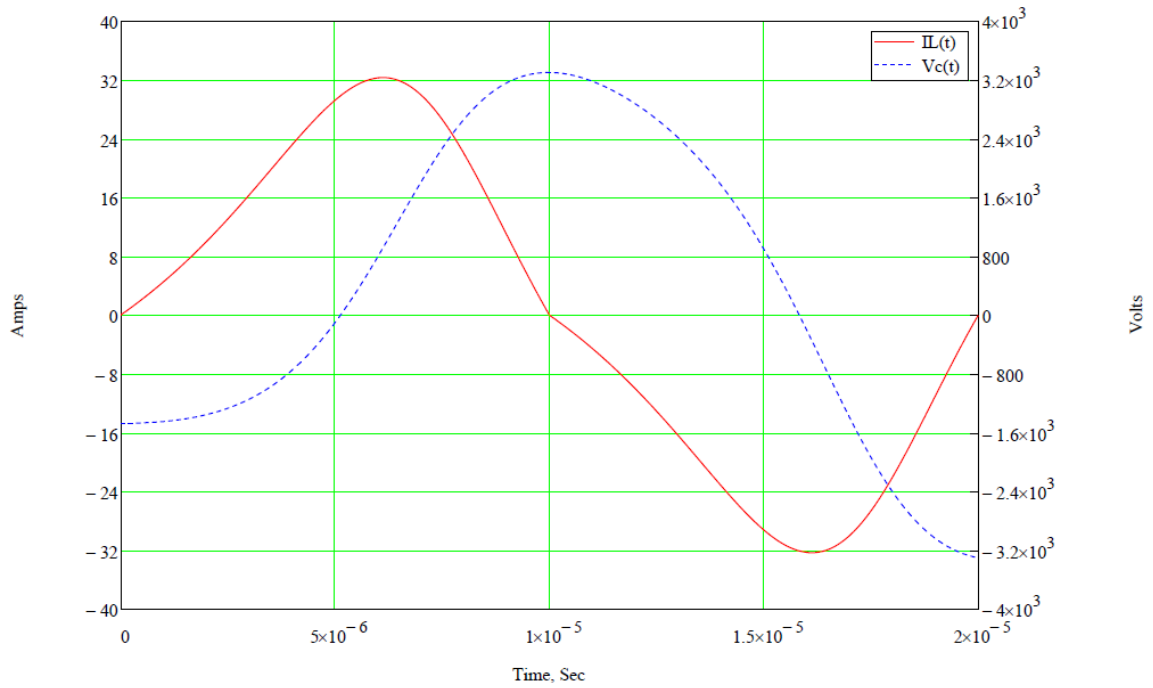


FIGURE 79 GRAPH OF  $V_c$  AND  $I_L$  WITH  $370\mu H$  CHOKE AND  $.034\mu F$  CAP

Figure 5.10 above illustrates the relationship and phase of the inductor current and capacitor voltage with ideal 7500W power transfer. The Figure also illustrates that the inductor current does not reach its peak at 50 kHz. This indicates the circuit will not

deliver full power at the switching frequency. In the simulation Figure 5.11 below illustrates the 380V was not achieved. The primary inductor current and capacitor voltage of figure 5.11 are sinusoidal but did not achieve the desired capacitor voltage or inductor current. Figure 5.12 illustrates the turn off and turn on switching currents are not ideal. These variations may be due to some parasitic capacitances of the switches or input filter capacitors. This may be corrected by reducing the ratio of the capacitor vs inductor value otherwise known as the Quality factor, or “Q”, of the circuit which may be too high and is not tune properly. Decreasing the Quality factor by increasing the capacitance will allow a more frequency tolerant variations.

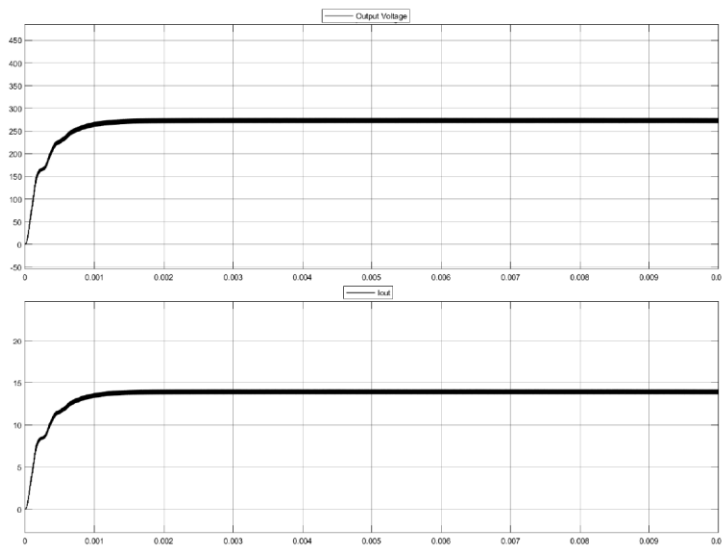


FIGURE 80 OUTPUT AND CURRENT WAVEFORMS WITH 380 $\mu$ F CHOKE AND 0.034 $\mu$ F CAPACITOR



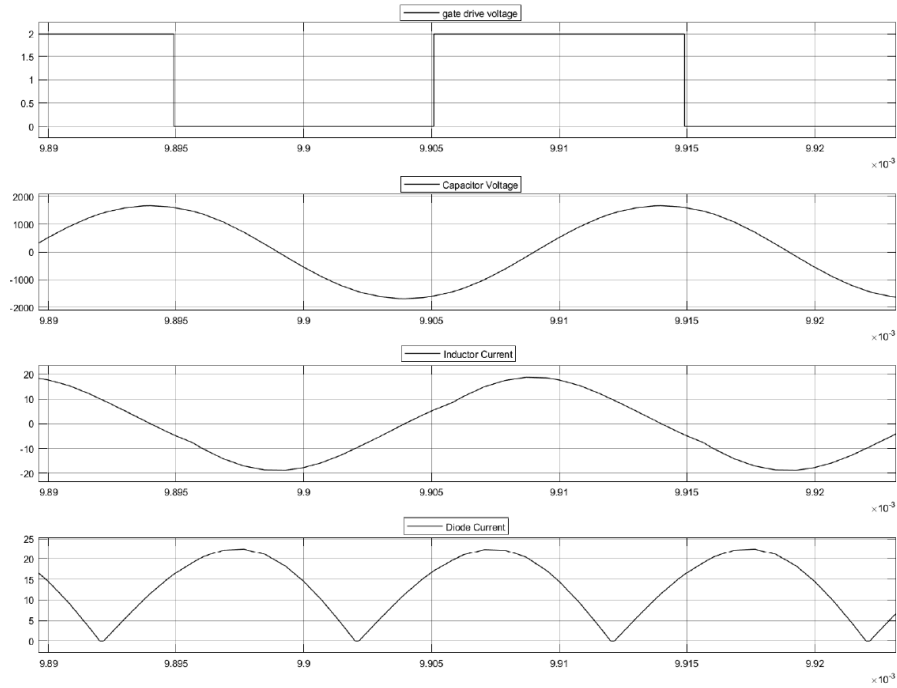


FIGURE 81 PRIMARY WAVEFORMS WITH  $370\mu\text{H}$  CHOKE AND  $0.034\mu\text{F}$  CAPACITOR

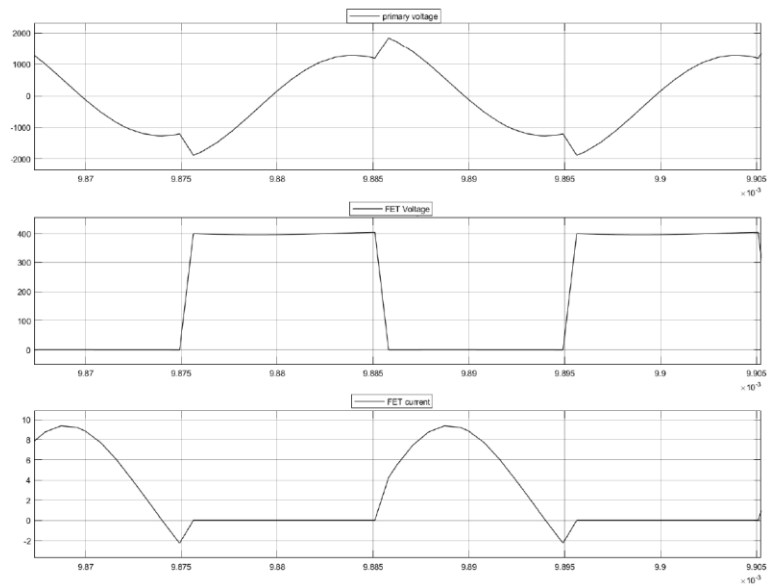


FIGURE 82 PRIMARY INDUCTOR VOLTAGE, FET VOLTAGE AND CURRENT WAVEFORMS WITH  $370\mu\text{H}$  CHOKE AND  $0.034\mu\text{F}$  CAPACITOR

The Q factor is a function of the Equivalent AC impedance or  $R_{ac}$  and the ratio between the inductor and capacitor values and turns ratio. The Equivalent output impedance is calculated by;

$$R_{ac} := \frac{8}{\pi^2} \cdot \frac{N_p^2}{N_s^2} \cdot R_o \quad (5-37)$$

$$R_{ac} = 15.606\Omega$$

The general equation of Q factor of a typical RLC circuit based solely on one LC combination.

$$Q = \frac{\sqrt{\frac{L_r}{C_r}}}{R_{ac}} \quad (5-38)$$

$$Q = 6.412$$

With a dual tuned RLC circuit the Q-factor equation is modified to account for both tuned circuits.

$$Q := \frac{\sqrt{\frac{2L_m + \frac{L_r}{2}}{2C_r}}}{R_{ac}} \quad (5-39)$$

$$Q = 4.77$$

Based on the separation between coils our estimated k-factor was 0.303. With this Q factor we can determine the coupling coefficient and verify against our estimated k-factor coupling coefficient. The k-factor can be derived as function of the combined reactive components of  $L_r$ ,  $C_r$  and Q based on the resonant frequency  $f_r$ .

$$k(F, L_T, C_T, Q) := \frac{Q}{|Z_P(F, L_T, C_T)|} \quad (5-40)$$

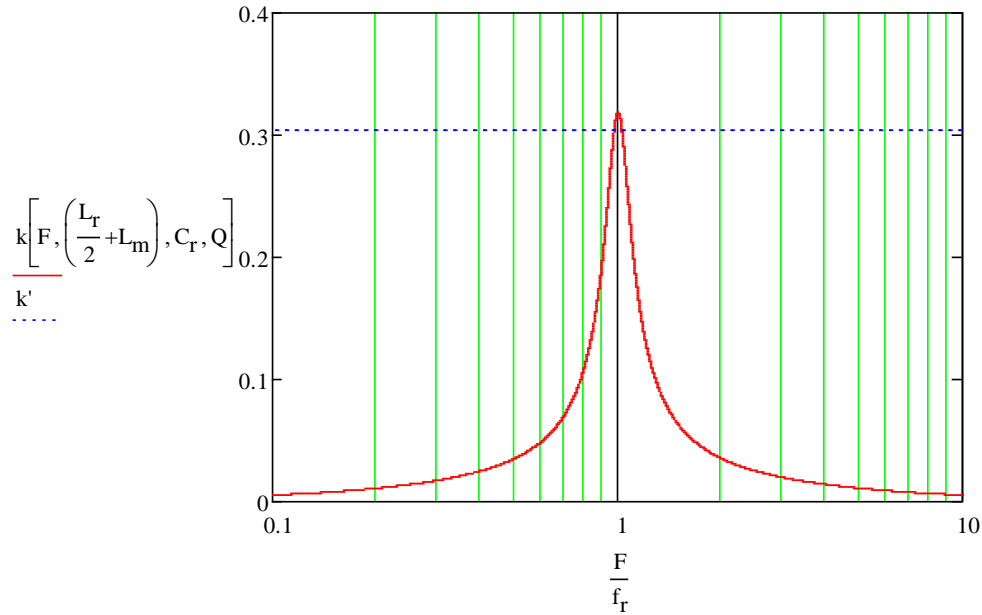


FIGURE 83 COUPLING COEFFICIENT “K”- FACTOR AS A FUNCTION OF REACTIVE COMPONENT VALUES AND 0.034 $\mu$ F

The peak “k”- factor value is 0.319 at 50 kHz. This higher k-factor would suggest better than estimated coupling and higher power output. But our simulation indicates this is not the case.

#### 5.4 PHASE 2: INCREASING THE RESONANT CAPACITOR VALUE TO 0.036 $\mu$ F

For optimal tuning of the resonant circuit either the capacitor or inductor value may need to be changed to achieve the desired result. By increasing the capacitor value it will lower the Q factor but also lower the resonant frequency. This will also allow for adjusting the capacitor value for the final tuned LRC circuit. Increasing the capacitor to 0.036 $\mu$ F lowers

the “k” factor to 0.309 and the Q-factor to 4.836. The calculated resonant frequency drops to 48.6 kHz. In the simulation below the output voltage increases to 360V. As can be seen in figure 4.15 both capacitor voltage and inductor current are both sinusoidal.

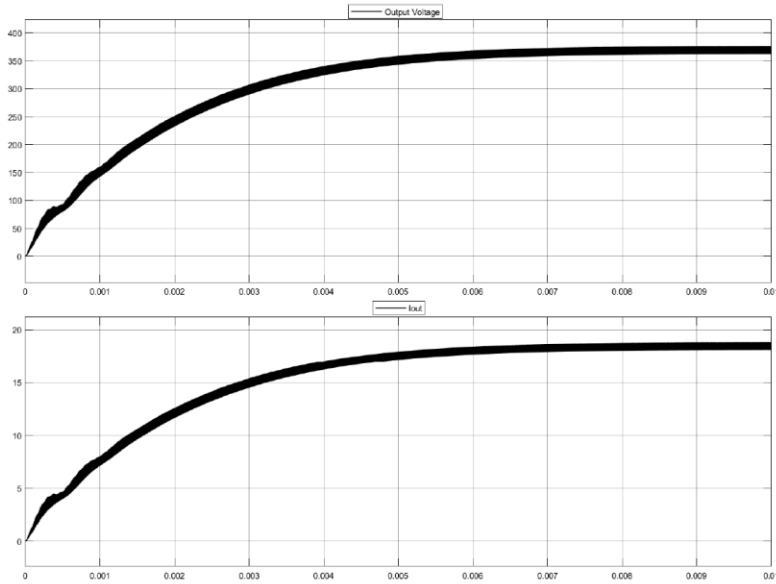


FIGURE 84 OUTPUT AND CURRENT WAVEFORMS WITH 380 $\mu$ F CHOKE AND 0.036 $\mu$ F CAPACITOR

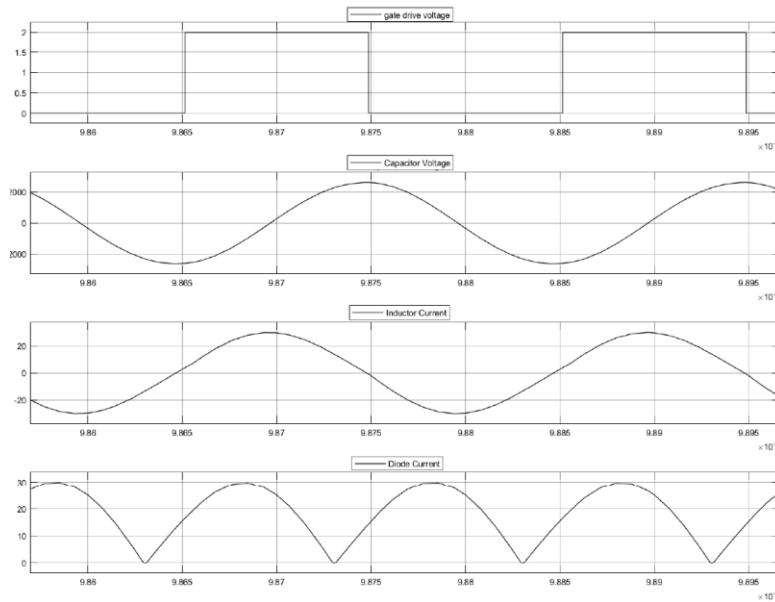


FIGURE 85 PRIMARY WAVEFORMS WITH 370 $\mu$ H CHOKE AND 0.036 $\mu$ F CAPACITOR

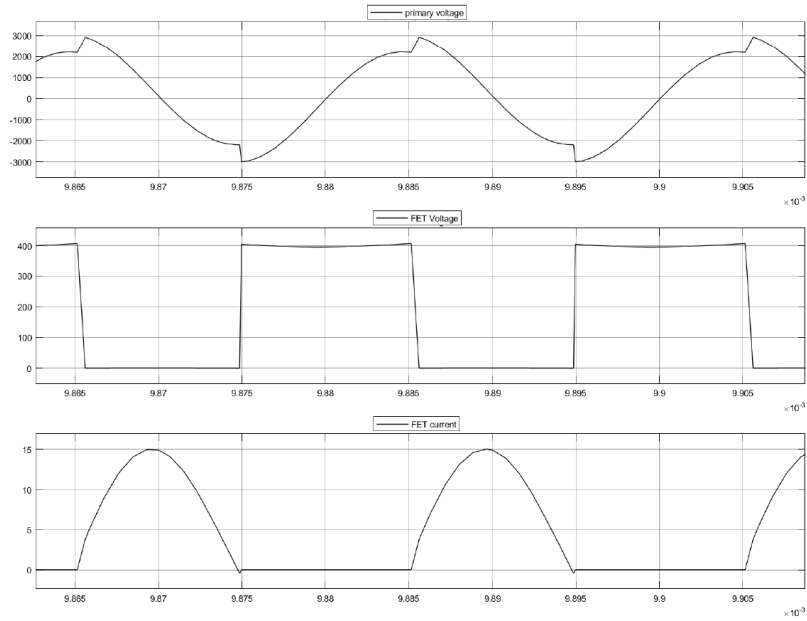


FIGURE 86 PRIMARY INDUCTOR VOLTAGE, FET DRAIN VOLTAGE AND FET CURRENT  
370 $\mu$ H CHOKE AND 0.036 $\mu$ F CAPACITOR

Based on the higher value of  $C_r$  the Q-Factor is reduced thereby reducing the coupling coefficient and lowers the resonant frequency to 43.5 kHz

$$Q = 4.836$$

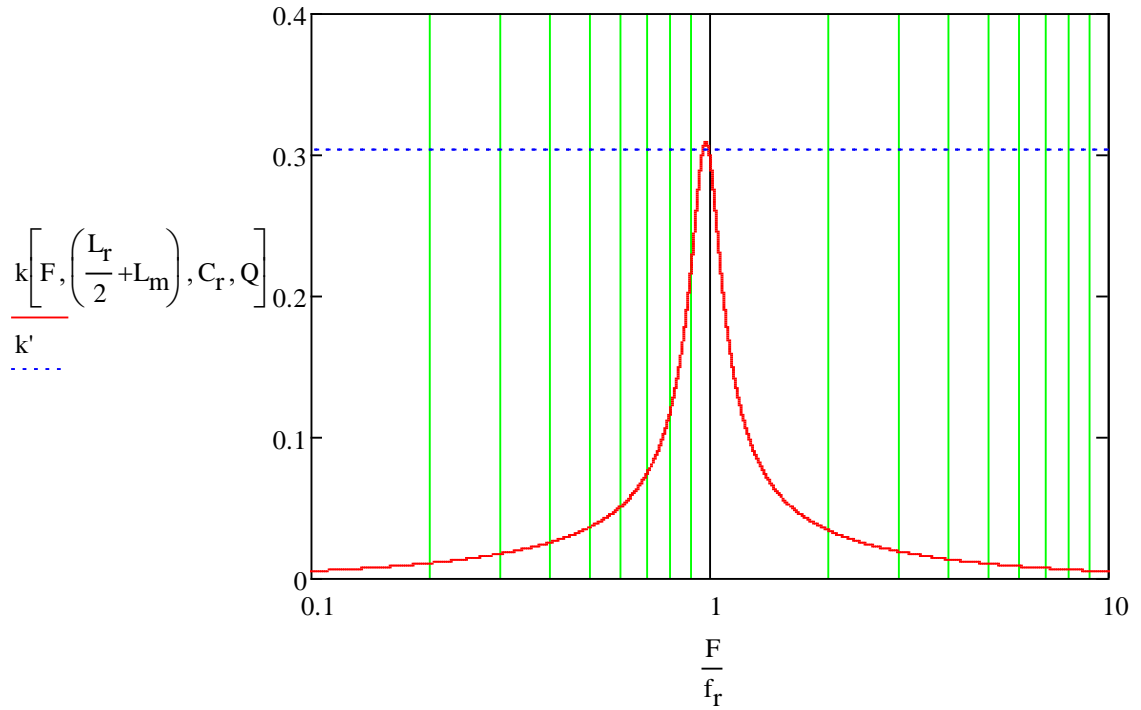


FIGURE 87 COUPLING COEFFICIENT “K”- FACTOR AS A FUNCTION OF  $C_R = 0.036\mu\text{F}$

### 5.5 PHASE 3: INCREASING THE RESONANT CAPACITOR VALUE TO $0.037\mu\text{F}$

Increasing the capacitor to  $0.037\mu\text{F}$  lowers the K factor to 0.305 the Q-factor is 4.836 and lowers the calculated resonant frequency to 47.96 kHz. The output voltage increases to 400V. As can be seen in figure 4.18 both capacitor voltage and inductor current are both sinusoidal.

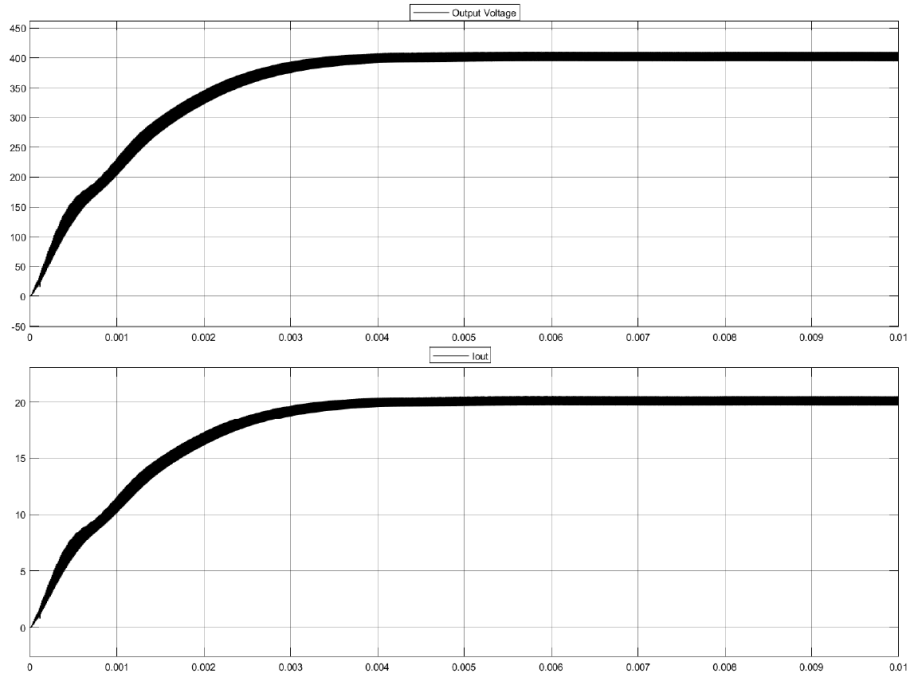


FIGURE 88 OUTPUT AND CURRENT WAVEFORMS WITH 380 $\mu$ F CHOKE AND 0.037 $\mu$ F CAPACITOR

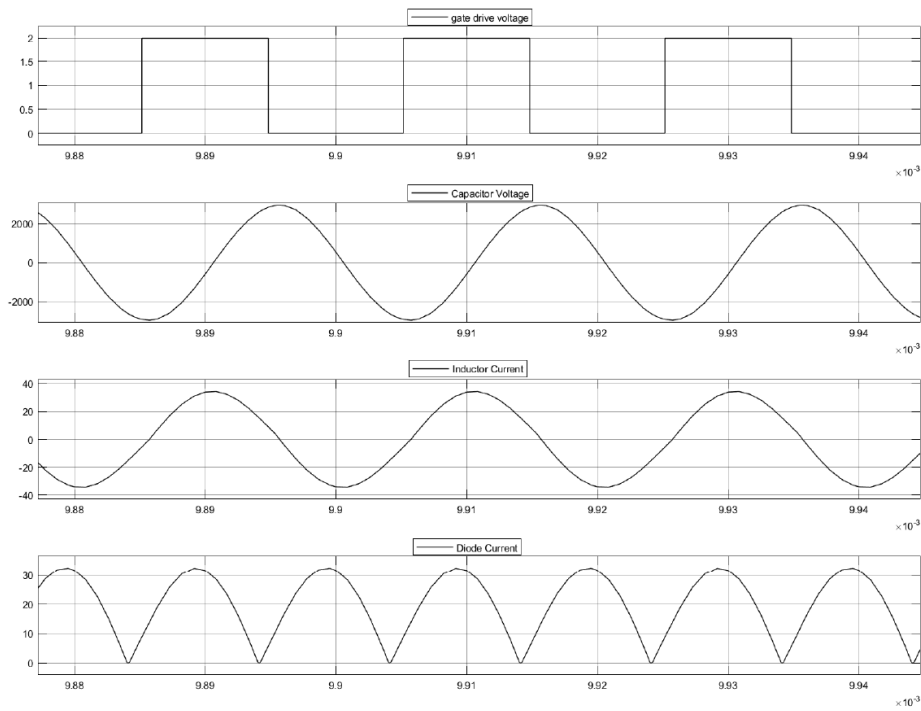


FIGURE 89 PRIMARY WAVEFORMS WITH 370 $\mu$ H CHOKE AND 0.037 $\mu$ F CAPACITOR

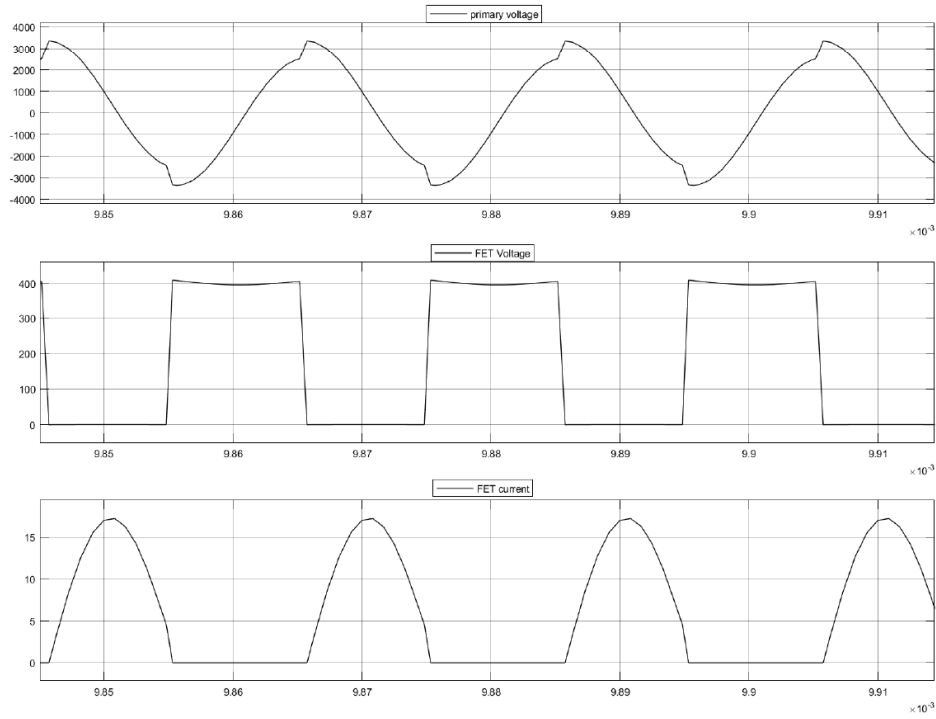


FIGURE 90 PRIMARY INDUCTOR VOLTAGE, FET DRAIN VOLTAGE AND FET CURRENT  
370 $\mu$ H CHOKE AND 0.037 $\mu$ F CAPACITOR

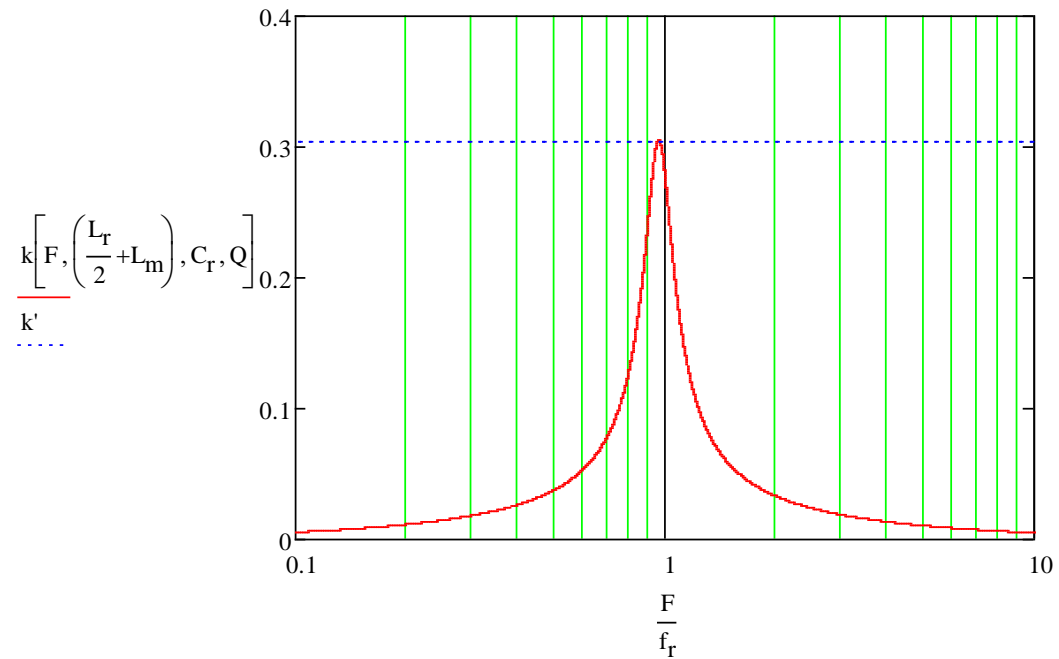


FIGURE 91 COUPLING COEFFICIENT “K”- FACTOR AS A FUNCTION OF  $C_R = 0.037\mu$ F



## 5.6 PHASE 4: INCREASING THE RESONANT CAPACITOR VALUE TO 0.038 $\mu$ F

Increasing the capacitor to 0.038 $\mu$ F lowers the K factor to 0.301 the Q-factor is 4.707 and lowers the calculated resonant frequency to 48.6 kHz. The output voltage increases to 400V and overshoots to 500V initially. As can be seen in figure 5.23 and 5.24 both capacitor voltage and inductor current are both sinusoidal.

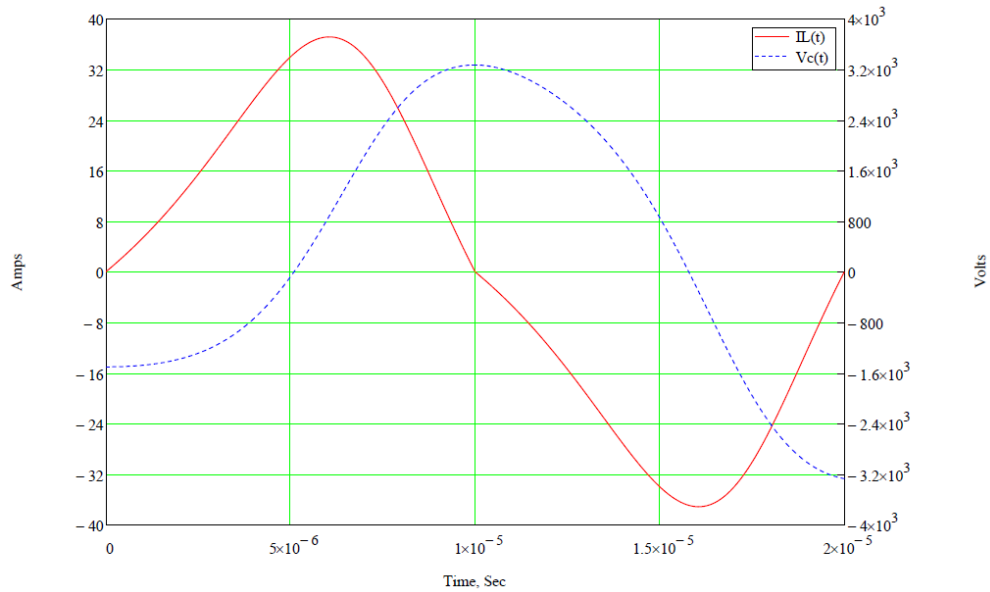


FIGURE 92 GRAPH OF  $V_C$  AND  $I_L$  WAVEFORMS WITH 380 $\mu$ H CHOKE AND 0.038 $\mu$ F CAPACITOR

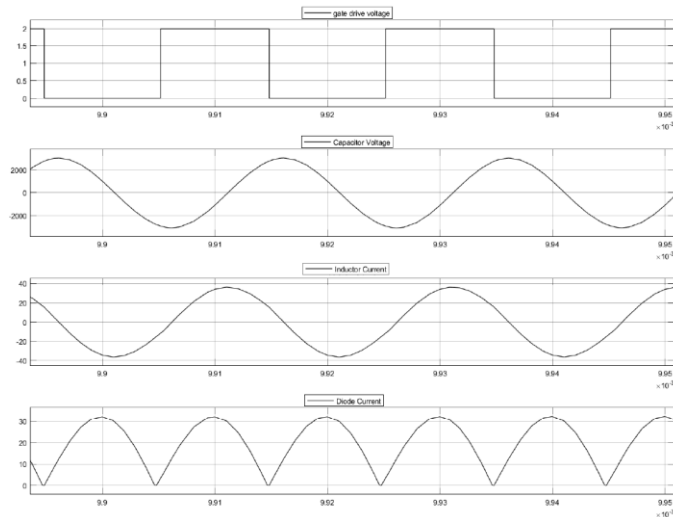


FIGURE 93 PRIMARY WAVEFORMS WITH 370 $\mu$ H CHOKE AND 0.038 $\mu$ F CAPACITOR

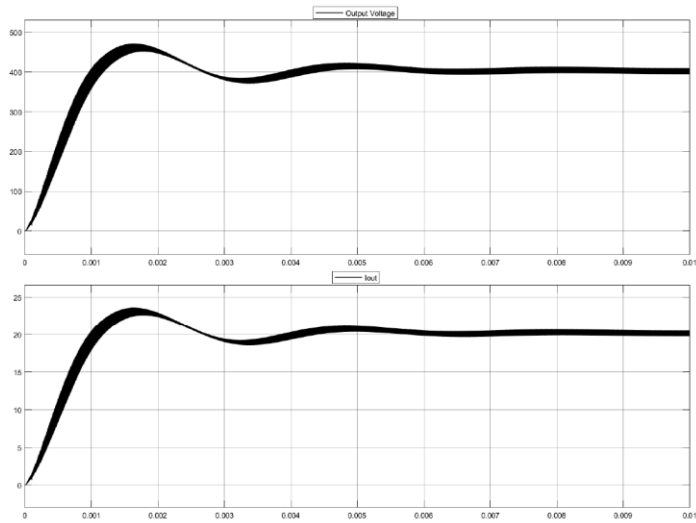


FIGURE 94 OUTPUT AND CURRENT WAVEFORMS WITH 380 $\mu$ H CHOKE AND 0.038 $\mu$ F CAPACITOR

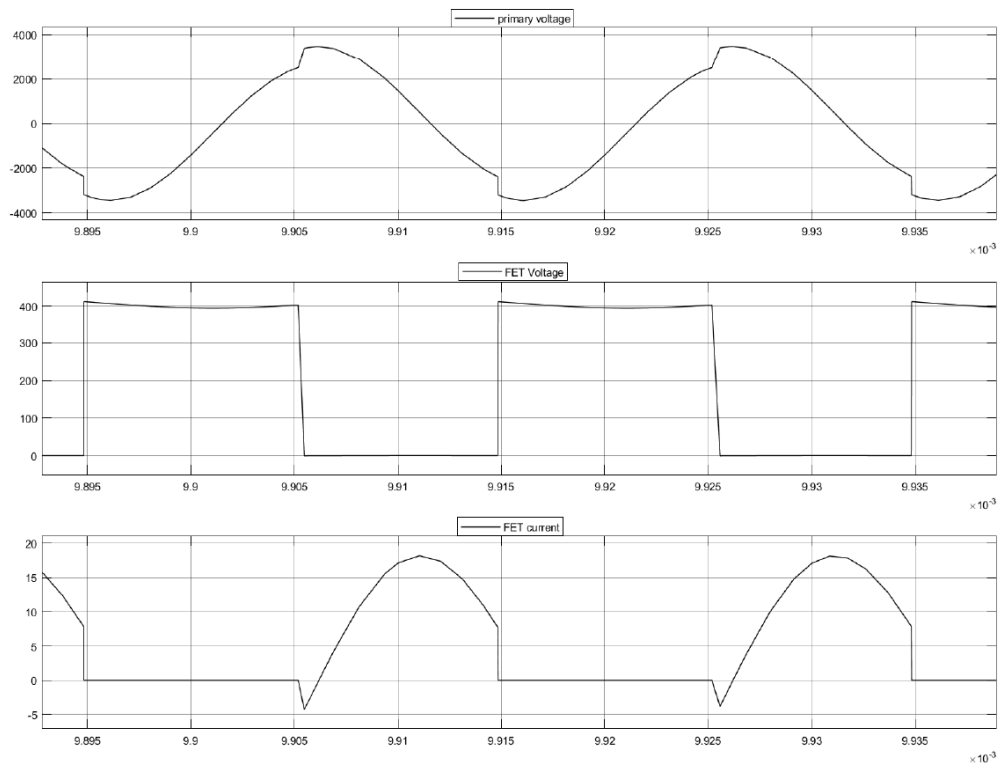


FIGURE 95 PRIMARY INDUCTOR VOLTAGE, FET DRAIN VOLTAGE AND FET CURRENT  
370 $\mu$ H CHOKE AND 0.038 $\mu$ F CAPACITOR

## 5.7 PHASE 5: ADDING SERIES INDUCTOR OUTPUT

Adding an inductor in series with the output is used to lower the resonant frequency but will actually increase the “Q” - Factor. Below are results with the resonant inductance of the transformer unchanged and with the resonant capacitor  $C_r$   $0.036\mu\text{F}$  and adding a  $16\mu\text{H}$  choke series with the secondary output filter.

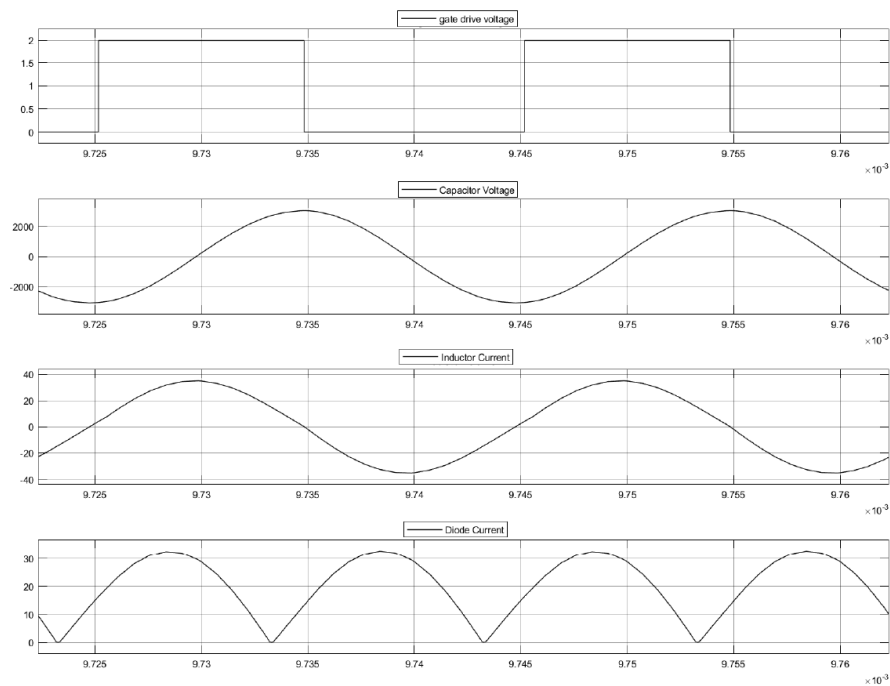


FIGURE 96 PRIMARY WAVEFORMS WITH  $370\mu\text{H}$  CHOKE AND  $0.038\mu\text{F}$  CAPACITOR AND  $16\mu\text{H}$  CHOKE ON OUTPUT

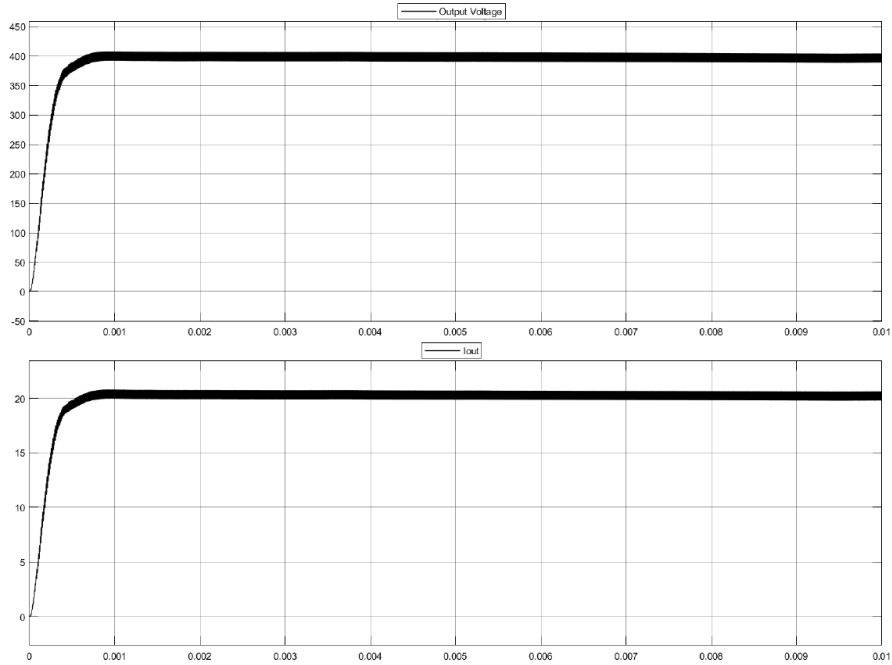


FIGURE 97 OUTPUT AND CURRENT WAVEFORMS WITH 380 $\mu$ F CHOKE AND 0.035 $\mu$ F CAPACITOR AND 16 $\mu$ H CHOKE IN SERIES WITH OUTPUT

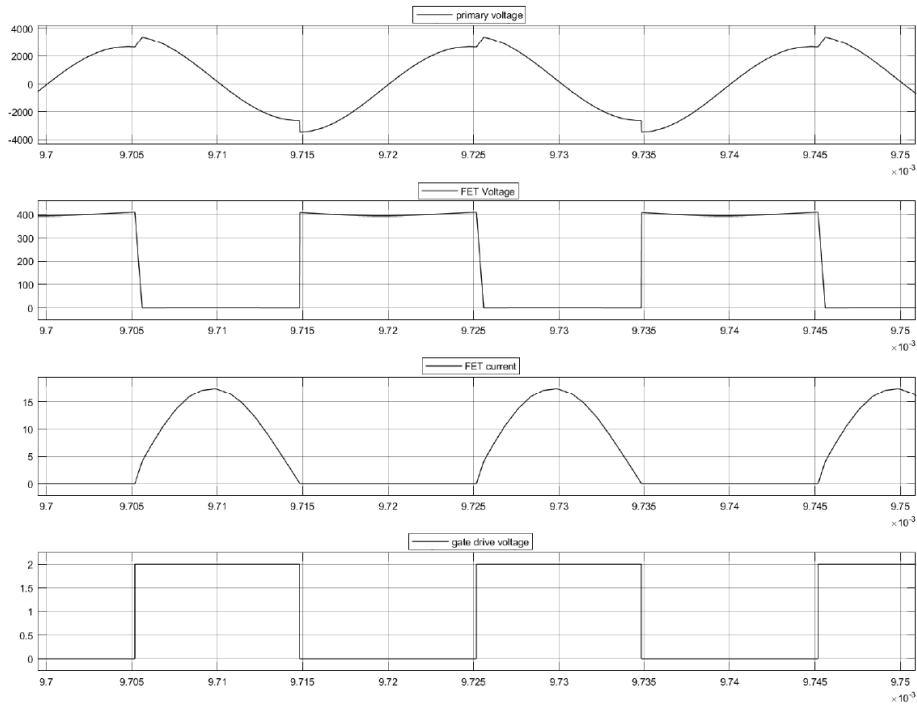


FIGURE 98 PRIMARY INDUCTOR VOLTAGE, FET DRAIN VOLTAGE AND FET CURRENT 370 $\mu$ H CHOKE AND 0.036 $\mu$ F CAPACITOR AND 16 $\mu$ H CHOKE

TABLE 5-1 SUMMARY OF CALCULATED VS SIMULATED VALUES

LC Combo	Switch Turn on current	Switch Turn off current	Est Cap Voltage	Peak Cap Voltage	Primary Inductor Current	Max Output Power	Eff
370 $\mu$ H and 0.034 $\mu$ F	2.25A	0A	2135V	1600V	13.2A	3877 W	94.83 %
370 $\mu$ H and 0.036 $\mu$ F	.5A	0A	3038V	2800V	21.21A	8309 W	95.15 %
370 $\mu$ H and 0.037 $\mu$ F	4.0A	0A	3014V	3000V	24A	8405 W	95.95 %
370 $\mu$ H and 0.038 $\mu$ F	7.2A	3A	2945V	3000V	25.4A	8241 W	96.73 %

With this value we can now find a capacitor based on capacitance and voltage rating. 4.1

## 5.8 PHASE 6: INCREASING PRIMARY LEAKAGE INDUCTANCE

Let's move to the other end of the spectrum and look at a more tightly coupled primary to secondary with 850 $\mu$ H on both the primary and secondary. See figure 5.28.

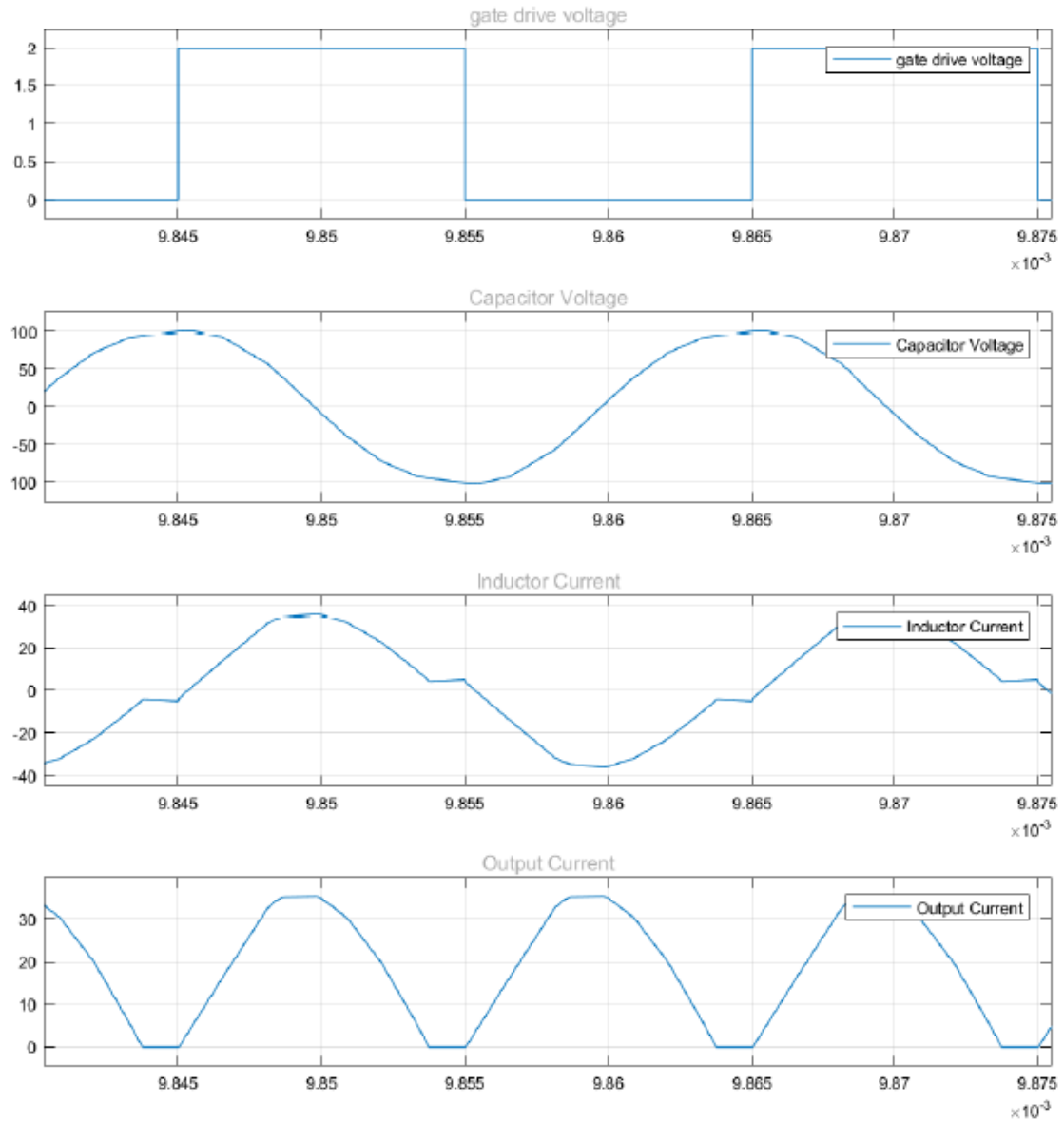


FIGURE 99 PHASE 6 PRIMARY WAVEFORMS

In this version of the design we have gotten back our dead time shown in the inductor current waveform.

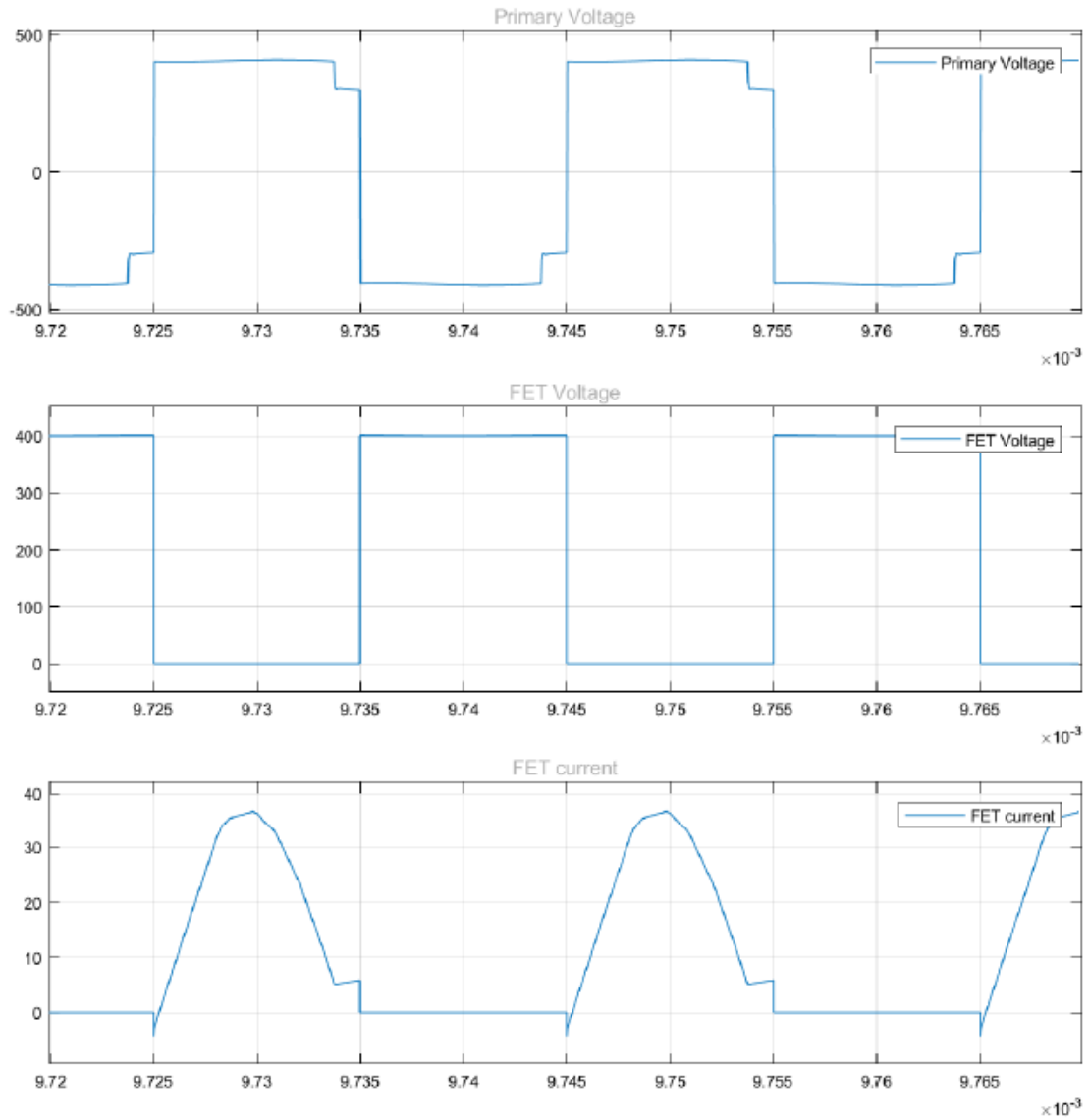


FIGURE 100 PRIMARY WAVEFORMS

We have our zero current during the transition and the efficiency is back up to 94.55%.

## 5.9 SIMPLIFIED SCHEMATICS OF CIRCUIT USED FOR SIMULATION

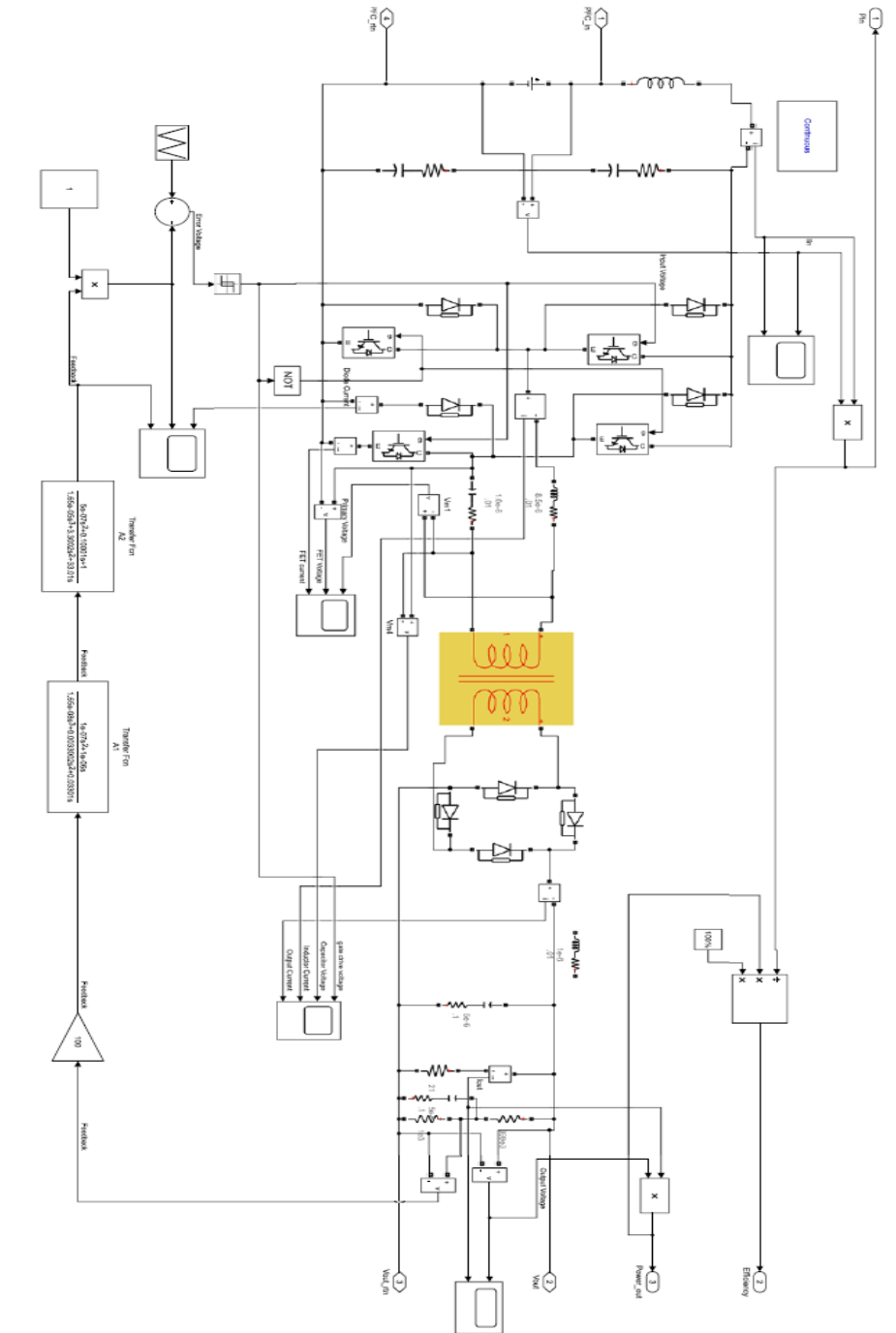


FIGURE 101 SCHEMATIC USED TO FOR SIMULATION TO PRODUCE WAVEFORMS



With components selected for a real world application using synchronous rectification.  
And doubling the FETs in the primary bridge.

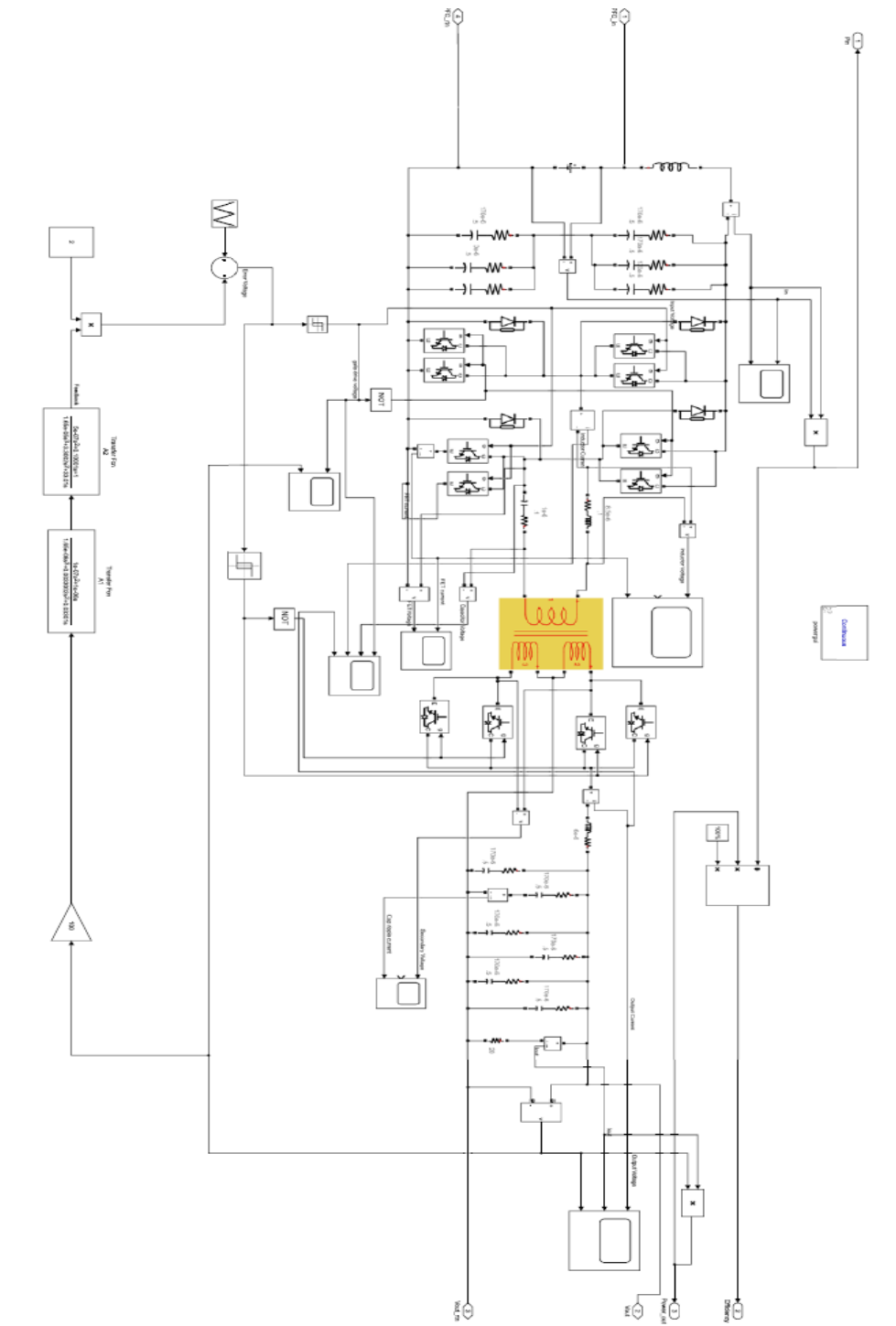


FIGURE 102 DESIGN 2 SCHEMATIC WITH NON-IDEAL COMPONENTS

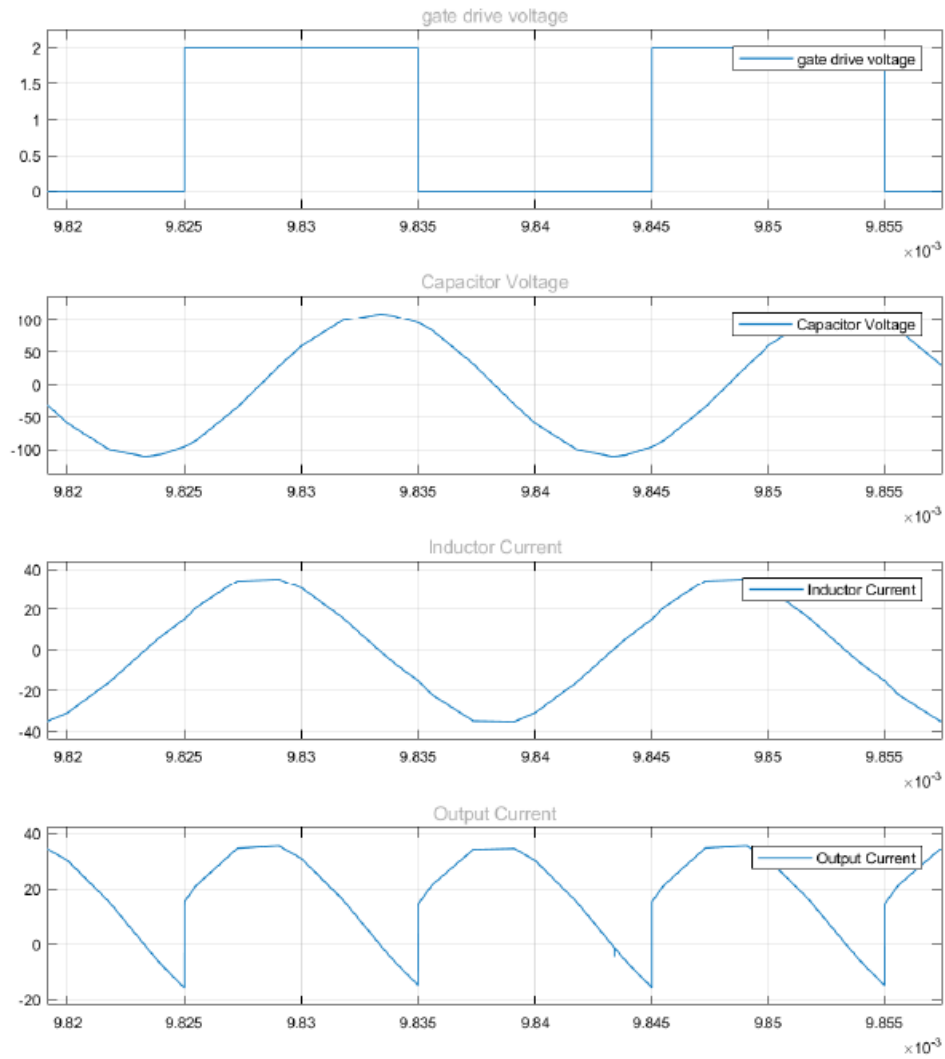


FIGURE 103 PRIMARY WAVEFORMS WITH REAL WORLD COMPONENT VALUES

The FETs turn on when the current is still at 18A which contributes to the switching losses then circulates through the anti-parallel diodes. Although we have a considerable amount of additional capacitor on the secondary the overall efficiency is still ok at 92.4% with an output voltage of 380V and 7460W. The peak current is 38A.

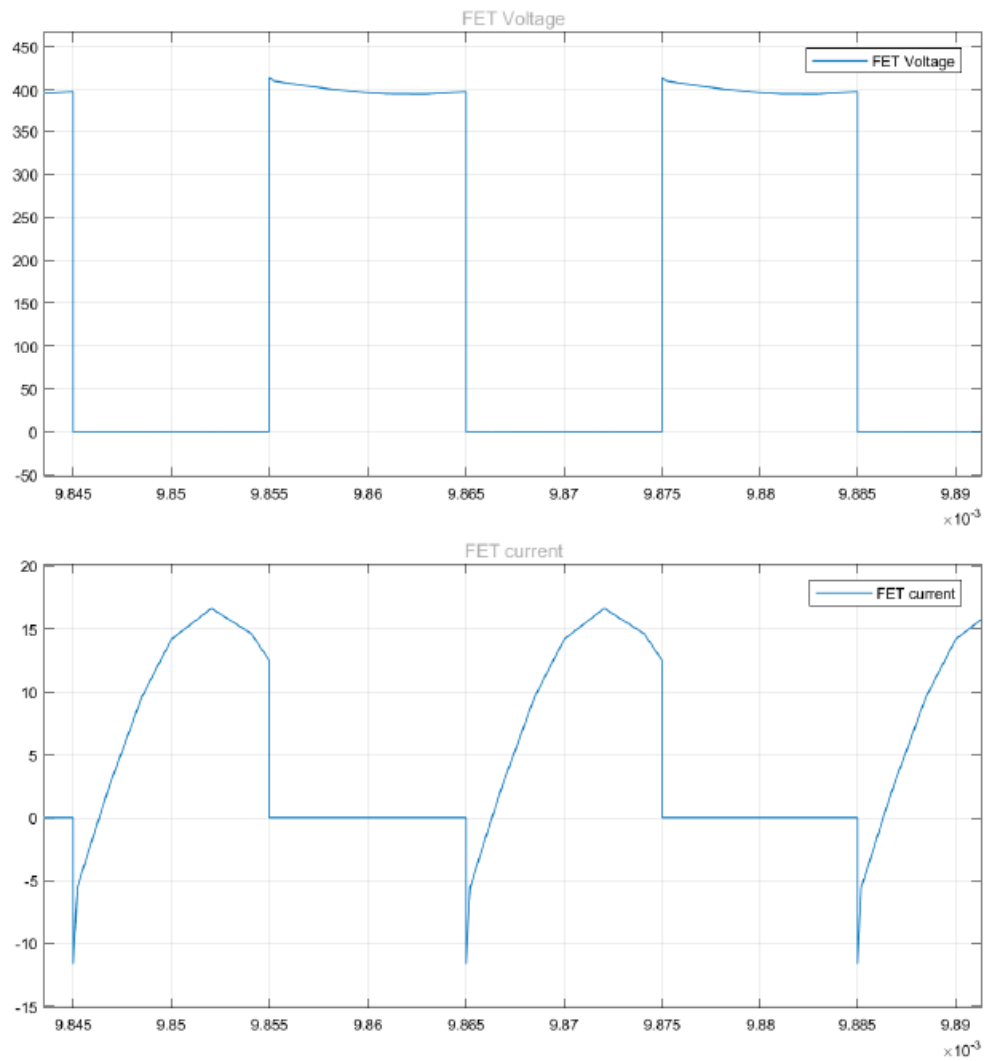


FIGURE 104 PRIMARY FET WAVEFORMS WITH REAL WORLD COMPONENT VALUES

Component selection for Schematic

## 5.10 SCHEMATIC DIAGRAHMS

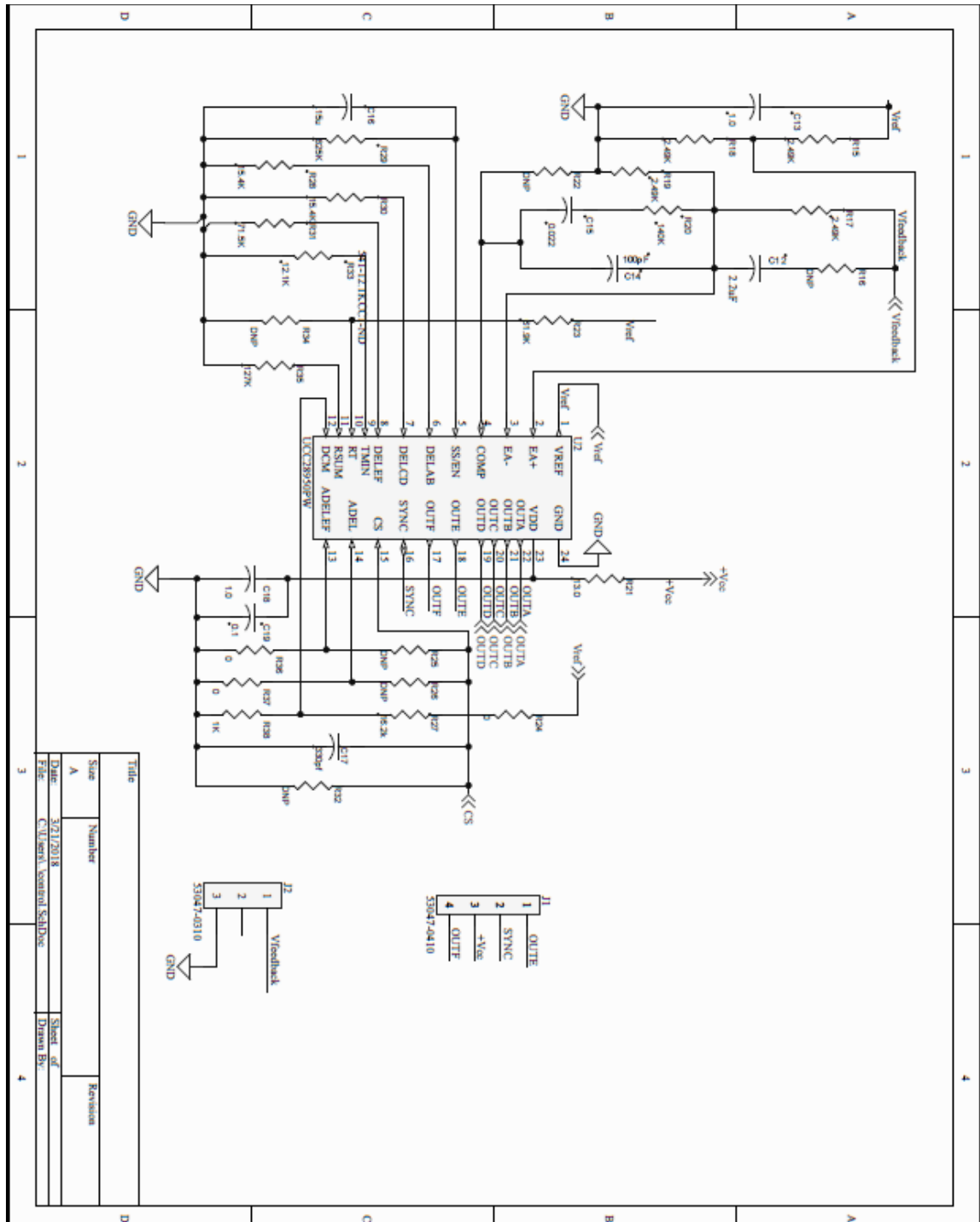


FIGURE 105 SCHEMATIC OF FULL BRIDGE CONTROL SECTION

FIGURE 106 SCHEMATIC OF PRIMARY FULL BRIDGE INVERTER SECTION

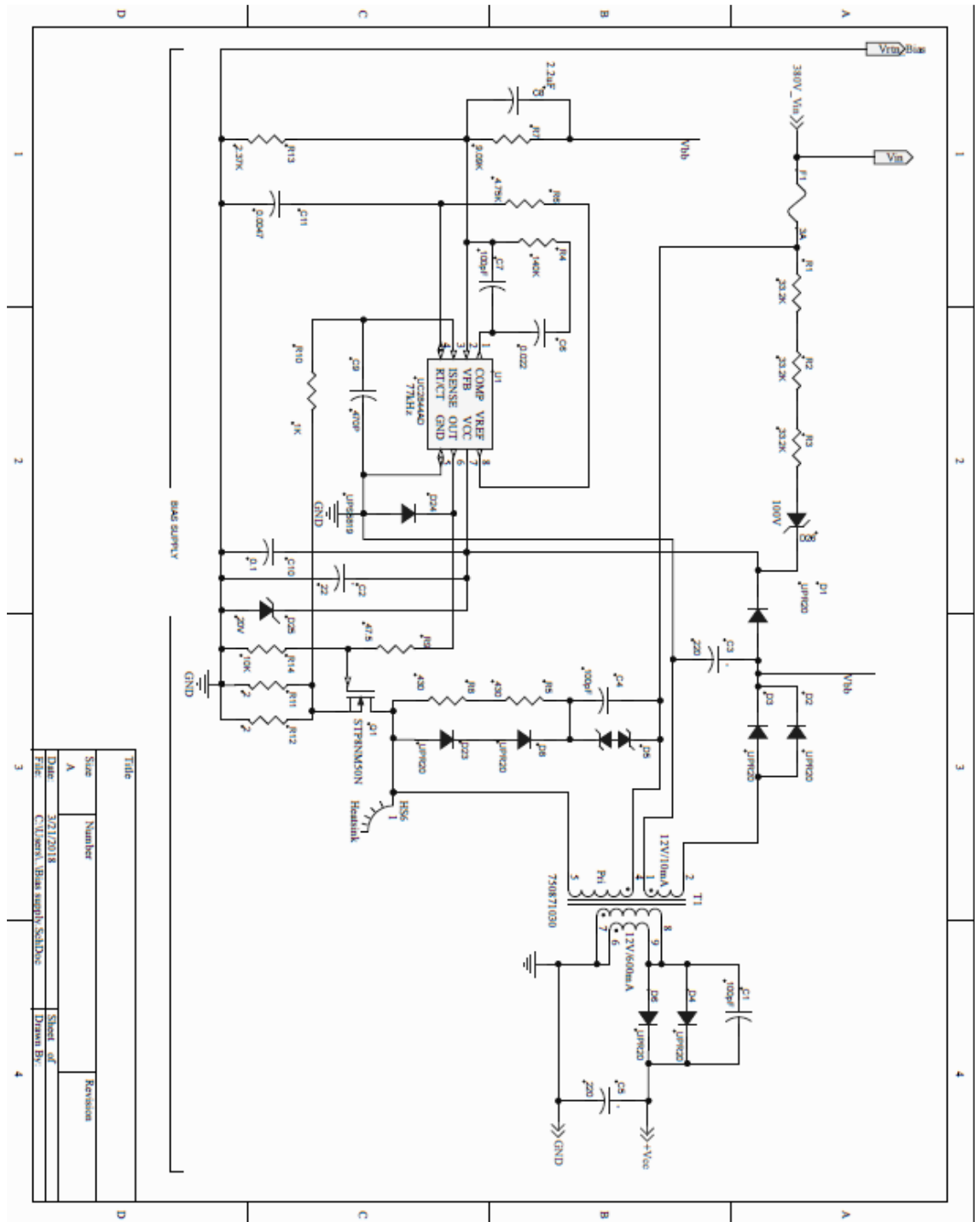


FIGURE 107 SCHEMATIC OF BIAS AND HOUSE KEEPING SUPPLY



## 5.11 TRANSFORMER DESIGN

### 5.11.1 TRANSFORMER CORE SELECTION

Transformers are typically designed to transfer power from primary to secondary winding using core of very high permeability. These cores are used in applications where the coupling coefficient is very high. This type of core is used in high frequency applications such as forward, half and full bridge converters as they offer the lowest losses at higher frequencies. These applications call for all the energy in the core being transferred from the primary to the secondary and very little energy stored or lost in the cores. Cores with low permeability are typically used in applications where energy is stored in the cores, such as flyback transformers or inductors. As such the size of the transformer is limited by the amount of energy that can be stored in the core for the given power level. Since we are using a resonant LC circuit the energy stored in the magnetic field generated by the current flowing through the inductor generates an electric field that transfers the energy to the capacitor. So since in this case energy storage is desired a low permeability core was chosen based on is transferred to the capacitor immediately transferred from the inductor to the capacitor in the form of voltage. Theoretically this form of energy transfer is lossless. So for this transformer the energy equation of an inductor was used and sizing provided by Magnetic Inc. inductor core selection procedure[37].

Since we are effectively using a pulse current with no DC component out “I” will be;

$$I := I_{\text{out}} + dI \quad (5-41)$$

$$I = 37.5 \text{ A}$$



Inductance  $L \cdot 1000$  to determine  $LI^2$  product for core sizing

$$L_T = 370.506 \mu\text{H}$$

$$L' := L \cdot 1000$$

Now we determine the energy stored in the core

$$L' \cdot I^2 = 520.313 \cdot \text{joule} \quad (5-42)$$

With the following assumption

$$\frac{L' \cdot I^2}{\text{Volume}} = 5 \cdot 10^{-4} \cdot \frac{\text{joule}}{\text{cm}^3} \quad (5-43)$$

We can determine the volume by

$$\text{Volume} := \frac{L' \cdot I^2}{5 \cdot 10^{-4} \cdot \frac{\text{joule}}{\text{cm}^3}} \quad (5-44)$$

$$\text{Volume} = 1040.625 \cdot \text{cm}^3$$

Now that we have the energy we can use the chart

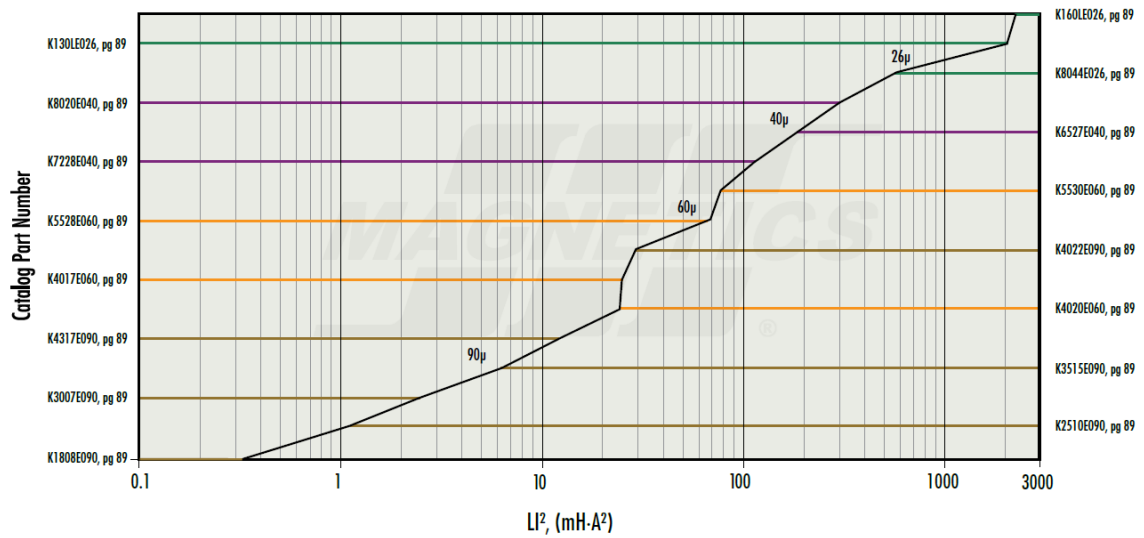


FIGURE 109 COOL MU “E-CORE” SELECTOR CHART

While we will be using “I-cores” or bar cores we can use this chart to determine the Initial permeability. We can also use them to obtain the relative size of the core. From here we see that a 26 permeability core is selected.

Blocks					
PART NO		A	B	C	Volume $V_e(\text{mm}^3)$
00_9541B***	mm in	95.00±0.61 3.740±0.024	41.00±0.51 1.614±0.020	27.51±0.41 1.083±0.016	107,200

FIGURE 110 MECHANICAL PARAMETERS OF BAR CORE

$$\text{Volume} := Q_t \cdot 107.2 \cdot \text{cm}^3$$

$$Q_t := 15$$

$$l_e := 20.8 \cdot \text{cm}$$

$$A_e := Q_t \cdot 3.89 \cdot \text{cm}^2$$

$$V_e := \text{Volume}$$

$$V_e = 1929.6 \cdot \text{cm}^3$$

$$A_L := Q_t \cdot 91 \cdot \text{henry}$$

$$N_{\text{w}} := \sqrt{\frac{L' \cdot (10^6)}{A_L}}$$

$$N = 16.464$$

$$H_{\text{w}} := \frac{.4 \cdot \pi \cdot N \cdot I}{l_e}$$

$$H = 46.873 \cdot \text{oersted}$$

$$\mu_{\text{eff}}(H) := \sqrt{\frac{-1.505 \cdot 10^{-4} \cdot \mu_i^3 \cdot H + 6.100 \cdot 10^{-9} \cdot \mu_i^4 \cdot H^2 + \mu_i^2}{-1.277 \cdot 10^{-4} \cdot \mu_i \cdot H + 2.740 \cdot 10^{-8} \cdot \mu_i^2 \cdot H^2 + 1}}$$

$$\mu_{\text{eff}}(H) = 24.199$$

$$N_a := N + N \cdot \frac{\mu_i - \mu_{\text{eff}}(H)}{\mu_i}$$

$$N_a = 16.991$$

$$N_{\text{a}}_{\text{w}} := N_a - \text{mod}(N_a, 1) + 1$$

$$N_a = 17$$

$$H_a := h_{ni} \cdot N_a \cdot I$$

$$H_a = 48.399$$

$$\mu_a(H_a) := \sqrt{\frac{-1.505 \cdot 10^{-4} \cdot \mu_i^3 \cdot H_a + 6.1 \cdot 10^{-9} \cdot \mu_i^4 \cdot H_a^2 + \mu_i^2}{-1.277 \cdot 10^{-4} \cdot \mu_i \cdot H_a + 2.740 \cdot 10^{-8} \cdot \mu_i^2 \cdot H_a^2 + 1}}$$

$$\mu_a(H_a) = 24.156$$

$$L_a := \frac{A_L \cdot (N_a^2) \cdot 10^{-6}}{1000}$$

$$L_a = 0.394 \cdot \text{mH}$$

$$L_e := \frac{\mu_a(H_a)}{\mu_i} \cdot L_a$$

$$L_e = 381.171 \cdot \mu\text{H}$$

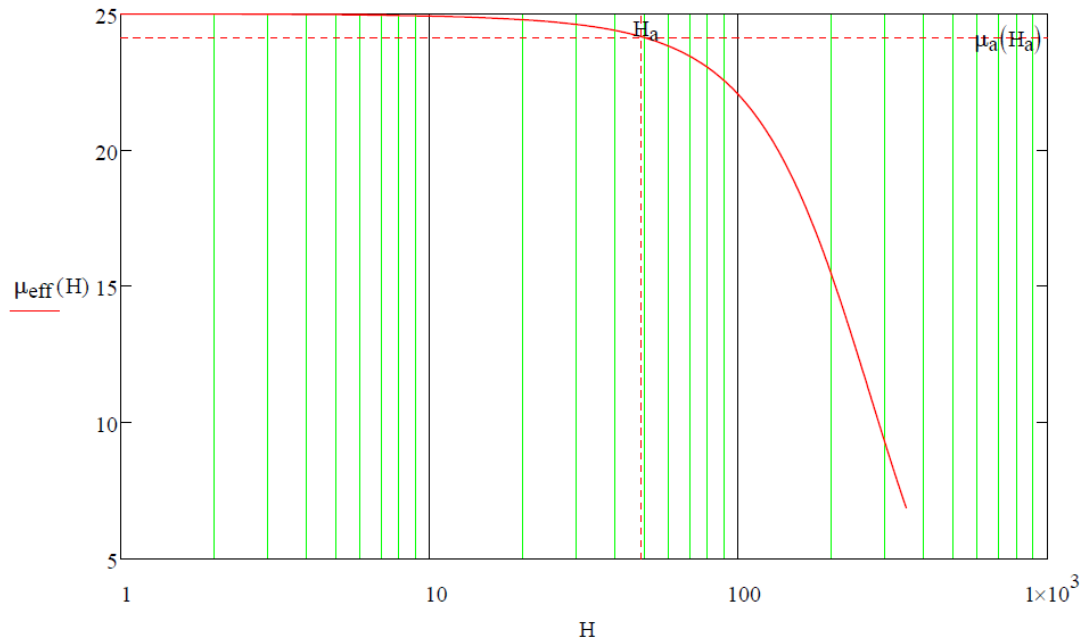


FIGURE 111 FIELD INTENSITY

### 5.11.2 DETERMINE WIRE GAUGE

Maximum Allowable Temperature Rise[37]

$$\Delta T_{cu} := 30 \quad I_{rms} = 37.5 \cdot A$$

Current density as a function of temperature

$$J := 297 \cdot \sqrt{\frac{\Delta T_{cu}}{15}} \cdot \frac{\text{amp}}{\text{cm}^2} \quad (5-45)$$

$f_r$

$$J = 420.021 \cdot \frac{\text{amp}}{\text{cm}^2}$$

Calculate total wire area as a function of current

$$\text{totArea} := \frac{I_{rms}}{J} \quad (5-46)$$

$$\text{totArea} = 8.928 \cdot \text{mm}^2$$

Calculate wire Diameter

$$dp := \sqrt{\text{totArea} \cdot \frac{4}{\pi}} \quad (5-47)$$

$$dp = 0.133 \cdot \text{in}$$

Calculate wire gauge based on wire diameter

$$AW := -\left(20 \cdot \log\left(\pi \cdot \frac{dp}{25.4 \cdot \text{mm}}\right)\right) \quad (5-48)$$

$$AW = 7.597$$

Rounding off Wire Diameter

$$AWG := (AW - \text{mod}(AW, 1)) + 1$$

(5-49)

$$AWG = 8$$

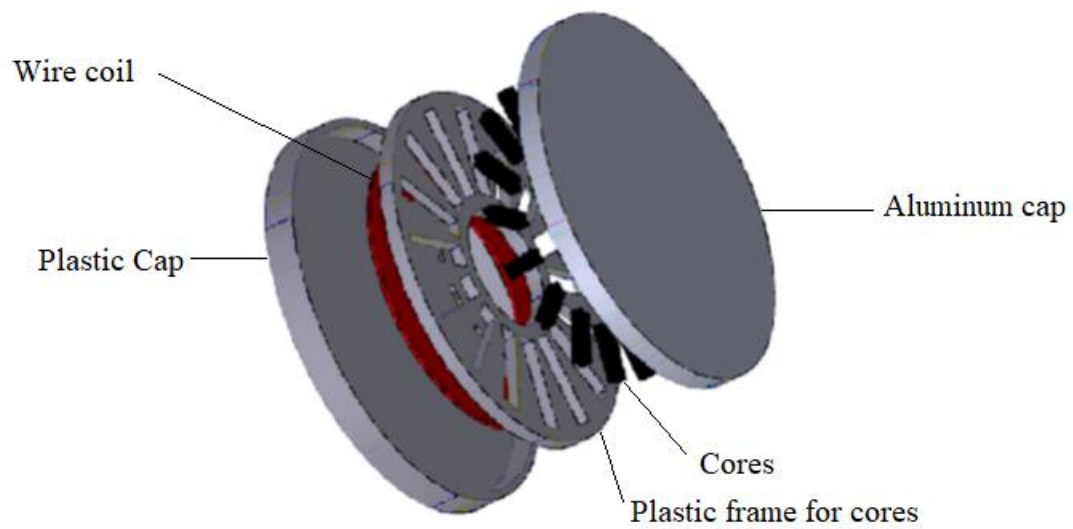


FIGURE 112 COMPONENTS OF WIRELESS TRANSFORMER

## Chapter 6. RESULTS AND CONCLUSION

### 6.1 RESULTS

Figures below illustrate the tradeoffs made in selecting switching frequency and varying capacitor values. Figure 5.44 below illustrates a peak current of 25A with only 200V in and 44w on the output switching initially at 83 KHz with 47% efficiency. All testing was performed with 49.9 ohm, 250W resistive load. Ch1 Gate Q9, Ch2 Drain Voltage Q9 and Ch4 Primary Current.



FIGURE 113 VIN 200V, VO 44.7V SWITCHING 83KHZ

Note: Ch1 Gate Q9, Ch2 Drain Voltage Q9 and Ch4 Primary Current.

Since we are not close to having a full sinusoidal current waveform reducing the switching frequency to 47 KHz did not make much of a difference in the tuning of the circuit with efficiency at 52%. The out did however become slightly unstable, as can be seen in the current waveform of Fig 5.45 below.

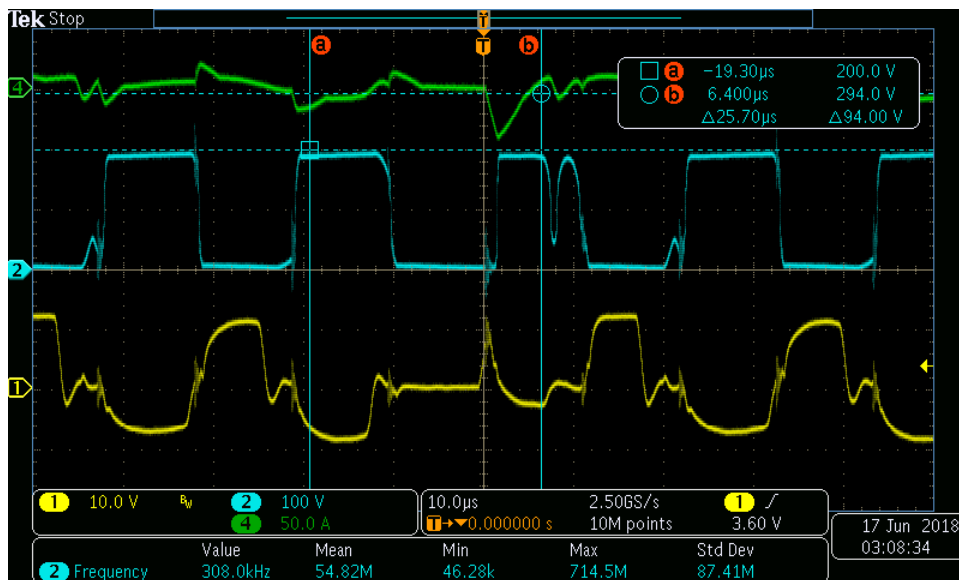


FIGURE 114 VIN 200V, VO 19V SWITCHING 47KHZ

Varying the input voltage as well as placement of the transformer primary and secondary wires made a significant difference in the performance of the converter. Figure 5.46 below illustrates that lowering the input voltage makes the converter more stable and improves the efficiency to 57%.

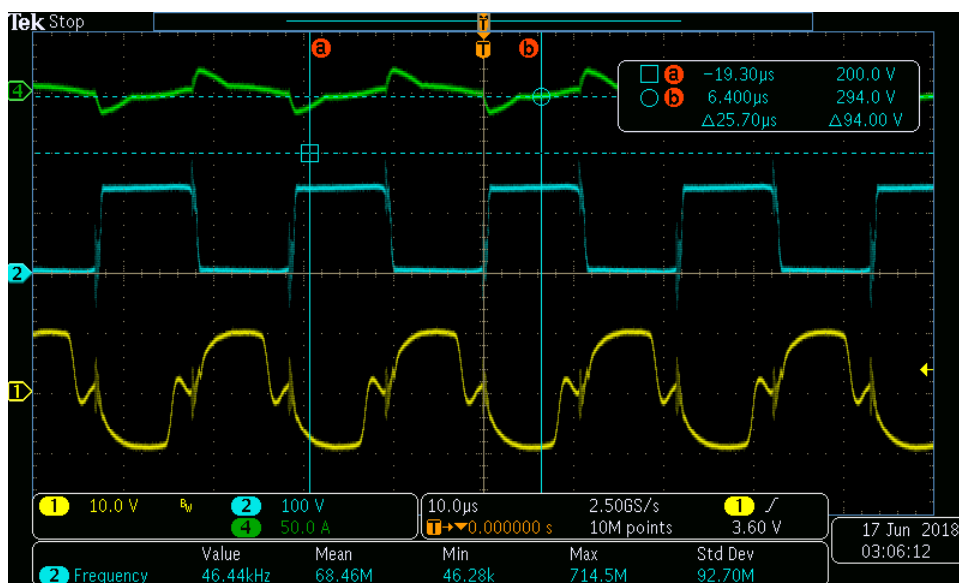


FIGURE 115 VIN 150V, VO 16V SWITCHING 47KHZ



Routing the primary and secondary transformer leads away from the drive section further improves the converter performance. Figure 5.47 below shows output increased to 50V and efficiency near 83% with peak currents nearing 50A.

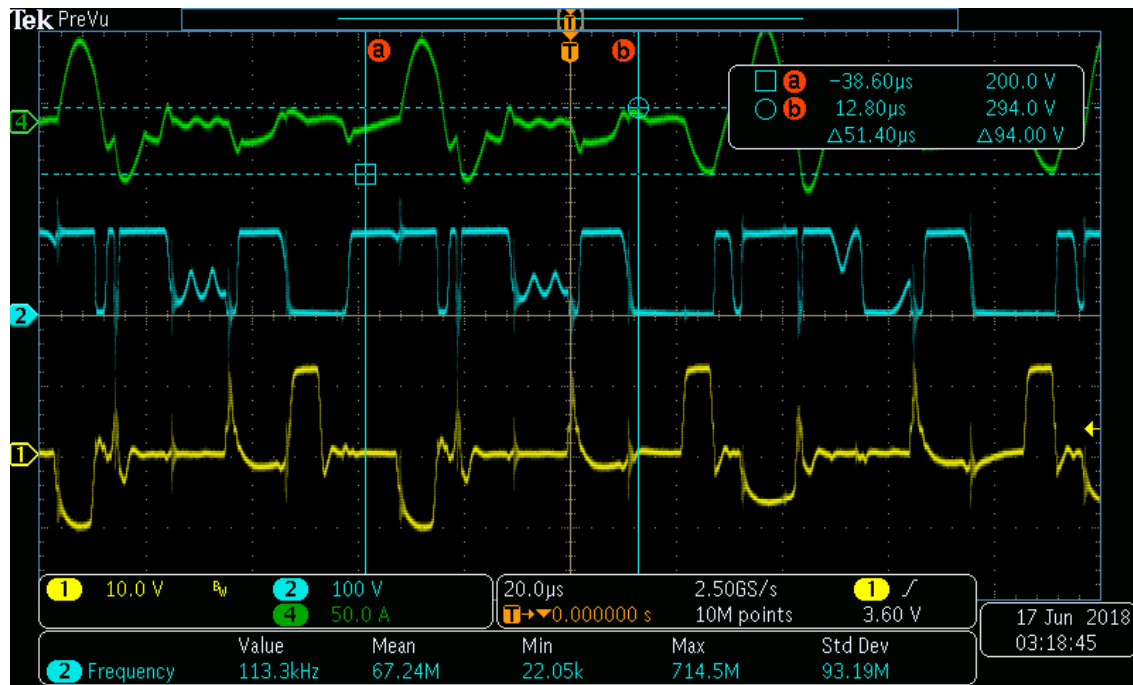


FIGURE 116 VIN 150v, VO 50v SWITCHING 47KHZ

Due to the noise associated with the transformer it was suspected that the output would not be able to be stabilized with any significant distance between primary and secondary. A 1.5 inch separation was added to check for power transfer. It was observed that the converter peak currents caused the output to shut down before a stable output could be developed.

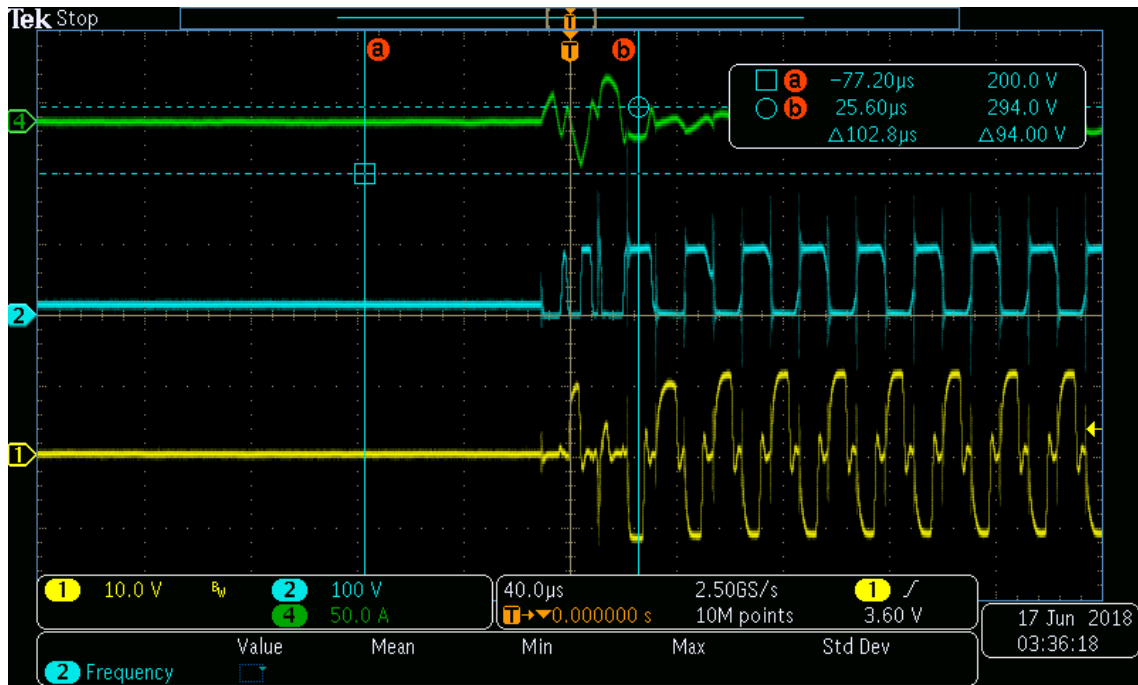


FIGURE 117 VIN 100V, WITH 1.5 INCH SEPARATION FROM PRIMARY TO SECONDARY

## 6.2 CONCLUSION

During the initial design phase all components from the schematic were selected and optimized to minimize inductor current and capacitor voltage. Over the design phase some of them became unavailable or had excessive lead times that prohibited getting them in time for the prototype stage. Due to availability and lead times of practical components, such as the 3kV capacitors the high current 1μF output capacitors and the aluminum shielding for the transformer, the LC - transformer and capacitor design selection had to be modified. The actual primary and secondary inductance chosen was set to 83μH and 0.108μF. While this should still provide the same resonant coupling we have seen in previous chapters it will lead to higher peak current and lower capacitor voltages making component selection a bit easier. The higher primary peak current will likely cause more

noise issues which will need to be addressed with shielding. Initially the 2 transformers are set directly on top of each other and are separated once a stable output is obtained. It was later determined that the output section was not properly configured for the synchronous rectification and as a result 600V rectifier diodes were used for this experiment. On my future work once the LC combination of the various filters are optimized I will order the long lead time items to ensure these critical components are available for prototype testing. While I was not able to obtain my 21cm separation with any substantial loading, my converter did show signs that I am on the right track.

## REFERENCES

1. Dai, J. and D.C. Ludois, *A Survey of Wireless Power Transfer and a Critical Comparison of Inductive and Capacitive Coupling for Small Gap Applications*. IEEE Transactions on Power Electronics, 2015. **30**(11): p. 6017-6029.
2. Shinohara, N., <Wireless Power Transfer via Radiowaves.pdf>, P.-N. Favenneec, Editor. 2014, JohnWiley & Sons, Inc. p. 247.
3. Wikipedia, t.f.e., *James Clerk Maxwell*.
4. Wikipedia, t.f.e. *Guglielmo Marconi*. Available from: [https://en.wikipedia.org/wiki/Guglielmo\\_Marconi](https://en.wikipedia.org/wiki/Guglielmo_Marconi).
5. Wikipedia, t.f.e. *Maurice Leblanc (engineer)*. Available from: [https://en.wikipedia.org/wiki/Maurice\\_Leblanc\\_\(engineer\)](https://en.wikipedia.org/wiki/Maurice_Leblanc_(engineer)).
6. Experts, T. *Happy Birthday, Heinrich Hertz!* Wed, 2017-02-22; Available from: <https://de.tek.com/blog/happy-birthday-heinrich-hertz>.
7. Wikipedia, t.f.e., *Tesla coil*. October 2016.
8. Institute, S.S.P. *Father of Microwave Power Transmission(MPT)*. Available from: [https://solarsat.org/billbrown\\_memorial.htm](https://solarsat.org/billbrown_memorial.htm).
9. Leonard David, S.c.s.S.I.C. *Peter Glaser*. June 9, 2014; Available from: <https://www.space.com/26175-peter-glaser-solar-power-satellite-obituary.html>.
10. Space.com. *Under New Plan, Satellites to Beam Power Down From Space*. November 2010; Available from: <https://www.space.com/9491-plan-satellites-beam-solar-power-space.html>.
11. Ofalla, J. *CES 2011: Fulton Innovation Taking Wireless Power to the Next Level*. 2011; Available from: <http://nerdreactor.com/2011/01/13/ces-2011-fulton-innovation-taking-wireless-power-to-the-next-level/>.
12. Wikipedia, t.f.e., *André-Marie Ampère*. June 2017, Wikipedia, the free encyclopedia.
13. Wikipedia, t.f.e., *Michael Faraday*. Wikipedia, the free encyclopedia.
14. Wikipedia, t.f.e., *Wireless power transfer*.
15. Rice, J., <Examining Wireless Power Transfer.pdf>. 2014 Texas Instruments Power Supply Design Seminar, 2014. **SEM2100**, (TI Literature Number: SLUP321 Topic 3 ): p. 24.
16. Minghua Xia, S.A., *On the Efficiency of Far-Field Wireless Power Transfer*. IEEE TRANSACTIONS ON SIGNAL PROCESSING, 2015, June, 1. **63**(11): p. 13.
17. Pozar, D.M., *Microwave Engineering*. 2012, JohnWiley & Sons, Inc.
18. Lu, F., et al., *A Double-Sided <italic>LCLC</italic>-Compensated Capacitive Power Transfer System for Electric Vehicle Charging*. IEEE Transactions on Power Electronics, 2015. **30**(11): p. 6011-6014.
19. Theodoridis, M.P., *Effective Capacitive Power Transfer*. IEEE Transactions on Power Electronics, 2012. **27**(12): p. 4906-4913.
20. Ludois, D.C., M.J. Erickson, and J.K. Reed, *Aerodynamic Fluid Bearings for Translational and Rotating Capacitors in Noncontact Capacitive Power Transfer Systems*. IEEE Transactions on Industry Applications, 2014. **50**(2): p. 1025-1033.
21. Baoyun Ge\*, S.M., IEEE, Daniel, C. Ludois, Member, IEEE, Rodolfo Perez, *The use of dielectric coatings in capacitive power transfer systems.pdf*. IEEE, 2014: p. 2193-2199.
22. J.G. Bolger, F.A.K.r.a.L.S.N., Khai, *Inductive power coupling for an electric highway system .pdf*. IEEE, 1979. **29**: p. 8.
23. Robert W. Erickson, D.M., *Fundamentals of Power Electronics*. 2004, KLUWER ACADEMIC PUBLISHERS.
24. MCLYMAN, C.W.T., *Transformer and Inductor Design Handbook.pdf*. 2004. p. 533.

25. *Power Electronics chapter 35 Contactless Energy Transfer.pdf*.
26. *<Power Electronics chapter 20 Resonant Conveters.pdf>*.
27. Yang, B., *LLC Resonant Converter*. p. 48.
28. Cederlöf, M., *Inductive Charging of Electrical Vehicles System Study*. 2012, KTH. p. 101.
29. Hong, H., D. Yang, and S. Won, *The Analysis for Selecting Compensating Capacitances of Two-Coil Resonant Wireless Power Transfer System*. 2017: p. 220-225.
30. Lindemann, A.E.a.A., *Analysis and Design of a Contactless Energy Transmission System with Flexible Inductor Positioning for Automated Guided Vehicles.pdf*. IEEE Transactions on Industrial Electronics, 2006: p. 6.
31. Esser, A., *Contactless charging and communication for electric vehicles.pdf*. IEEE Transactions on Industrial Electronics, 1995: p. 8.
32. Kazmierkowski, A.J.M.a.M.P., *FPGA based control of series resonant converter for contactless power supply.pdf*. 2006. **IEEE**: p. 6.
33. *<Power Electronics chapter 35 Contactless Energy Transfer.pdf>*.
34. Rui Jin, Z.Y., Fei Lin, *<Mutual inductance identification and maximum efficiency control of wireless power transfer system for the modern tram.pdf>*. 2017.
35. Surajit Das Barman, A.W.R., Narendra Kumar, Md. Ershadul Karim, Abu Bakar Munir, *Wireless powering by magnetic resonant coupling: Recent trends in wireless power transfer system and its applications*. ScienceDirect, Renewable and Sustainable Energy Reviews, 2014: p. 1525–1552.
36. Felic, R.M.D.a.G., *Analysis of the Coupling Coefficient in Inductive Energy Transfer Systems*. Active and Passive Electronic Components, 2014. **2014, Article ID 951624, 6 pages**: p. 7.
37. Inc, M., *Magnetics POWDER CORES*. 2015,